

DISS. ETH NO. 16034

Quasi Elastic Charm Production in Neutrino-Nucleon Scattering

A dissertation submitted to the

SWISS FEDERAL INSTITUTE OF TECHNOLOGY ZURICH

for the degree of

Doctor of Natural Sciences

presented by

Markus Bischofberger

Dipl. Phys., ETH Zurich

born 23.06.1975

citizen of

Teufen AR, Niederweningen ZH

Switzerland

accepted on recommendation of

Prof. Andre Rubbia, examiner

Prof. Felicitas Pauss, co-examiner

April 2005

Abstract

A study of quasi elastic charm production in charged current neutrino-nucleon scattering is presented. A sample of about 1.3 million interactions recorded with the NOMAD detector in the CERN SPS wide band neutrino beam has been searched for quasi elastically produced charmed baryons (Λ_c^+ , Σ_c and Σ_c^*). The search has been performed in two exclusive decay channels of the Λ_c^+ , both including a Λ . Also, the semi-inclusive decay channels Λ_c^+ , Σ_c , $\Sigma_c^* \rightarrow \Lambda + X$ have been studied. Kinematic selection criteria have been chosen in order to obtain samples enriched with quasi elastic charm events. Signal efficiencies and background expectations have been estimated by Monte Carlo simulations. The observed number of events in each searched channel has been found to agree with the background expectation from charged and neutral current reactions and an upper limit for the cross section has been derived. For the quasi elastic charm production cross section averaged over the neutrino energy spectrum ($\langle E_\nu \rangle = 24.3 \text{ GeV}$) the upper limit has been found to be $\langle \sigma_{\text{QEC}} \rangle < 3.58 \times 10^{-40} \text{ cm}^2$ or relative to the total charged current cross section $\langle \sigma_{\text{QEC}} \rangle / \langle \sigma_{\text{cc}} \rangle < 0.22\%$ at 95% confidence level. Assuming an energy independent cross section for neutrino energies above 15 GeV, an upper limit of $\sigma_{\text{QEC}} < 4.0 \times 10^{-40} \text{ cm}^2$ (95% C. L.) has been found for the absolute cross section.

Kurzfassung

Diese Arbeit befasst sich mit der quasi-elastischen Charmproduktion in den geladenen schwachen Wechselwirkungsprozessen bei der Streuung von Neutrinos an Nukleonen. Ungefähr 1.3 Millionen Ereignisse wurden mit dem NOMAD Detektor im CERN SPS Breitbandneutrinostrahl aufgezeichnet und nach quasi-elastisch erzeugten Charmbaryonen (Λ_c^+ , Σ_c und Σ_c^*) durchsucht. Die Suche wurde in zwei exklusiven Zerfällen des Λ_c^+ durchgeführt, welche je ein Λ enthalten. Zusätzlich wurde nach den halb-inklusiven Zerfällen $\Lambda_c^+, \Sigma_c, \Sigma_c^* \rightarrow \Lambda + X$ gesucht. Quasi-elastische Ereignisse wurden durch die Anwendung von kinematischen Auswahlkriterien angereichert. Die Effizienzen der Auswahlbedingungen, wie auch die Beiträge der Untergrundprozesse, wurden mit Hilfe von Monte Carlo Simulationen abgeschätzt. Die beobachtete Anzahl der Ereignisse, welche die Auswahlkriterien erfüllen, stimmt mit den erwarteten Beiträgen der Untergrundprozesse von geladenen und neutralen schwachen Wechselwirkungen überein und somit kann nur eine obere Grenze für den Wirkungsquerschnitt berechnet werden. Für den Wirkungsquerschnitt der quasi-elastischen Charmproduktion, gemittelt über das Energiespektrum des Neutrinostrahls ($\langle E_\nu \rangle = 24.3 \text{ GeV}$), wurde eine obere Grenze von $\langle \sigma_{\text{QEC}} \rangle < 3.58 \times 10^{-40} \text{ cm}^2$ für das 95 % Vertrauensintervall gefunden. Relativ zum totalen geladenen schwachen Wirkungsquerschnitt entspricht dies einer oberen Grenze von $\langle \sigma_{\text{QEC}} \rangle / \langle \sigma_{\text{cc}} \rangle < 0.22 \%$. Unter der Annahme eines konstanten Wirkungsquerschnitts für quasi-elastische Prozesse bei Neutrinoenergien über 15 GeV wurde eine obere Grenze von $\sigma_{\text{QEC}} < 4.0 \times 10^{-40} \text{ cm}^2$ für das 95 % Vertrauensintervall gefunden.

Acknowledgments

The successful completion of this thesis would not have been possible without the assistance and support of many people.

First of all, I would like to thank Prof. A. Rubbia who offered me the opportunity to undertake the work towards this degree. His guidance and advice throughout the years have truly been essential to finally reach this goal.

I am also very grateful to Prof. Wulf Fetscher for his advice and many useful discussions during the last two years. For the appraisal of my work and the willingness to act as co-examiner I would like to thank Prof. Felicitas Pauss.

Further, I would like to thank all the members of the NOMAD collaboration who have done a tremendous job in realizing this experiment. Especially, I would like to mention Roberto Petti who was my link to the slowly disbanding collaboration and who provided me with all the relevant information about the data storage and the Monte Carlo simulations.

My thanks go also to Rosa Bächli, Dr. Andreas Badertscher, Leo Knecht and Gustav Natterer who warmly welcomed me in the Zurich group. I am especially indebted to Rosa for taking care of all the administrative things during these last 4 years, thereby making my life so much easier. Also, I am much obligated to Andreas Badertscher and Wulf Fetscher for proofreading my manuscript and eliminating lots of mistakes.

I would like to thank Salvatore Mangano my “office neighbor”, who was a good friend during all these many years at ETH. Besides providing invaluable help with many problems I encountered in my work, he has been an excellent teammate for soccer, tennis and foosball and I will never forget our travels to South Africa, Peru and Chile.

Further, I have to thank all the friendly people I met at our institute and I would especially like to mention Simon Baumgartner, Petra Häfliger, Marco Laffranchi and David Meer. Simon has helped me many times with my Linux problems and he has been a frequent and competent company when having a beer. Petra has always been an interesting partner for conversation on all topics. Her founded knowledge about good \LaTeX style, however, made me soon stop showing her any of my work. Marco has entertained me every time he found his way from the lab to my office and I am very thankful for his translations in Italy which helped me to survive. I am indebted to David for smoothing my way by exploring all the nifty \LaTeX features just before I needed them.

My thanks go also to Andreas Wenger the founder of our weekly movie evening and Pascal Halder a close friend ever since Kindergarten. Special thanks also to Dr. Thomas Flückiger, Dr. Gérald A. Wigger and Christian Kottler for the many enjoyable hours in

the Bistro or hanging out in Zurich and not to forget the exciting travels to South Africa and South America.

Finally, I would like to warmly thank my parents, Myrta and Walter Bischofberger, who always supported and encouraged me throughout my education. This thesis could not have been done without them.

To everyone I mentioned and those I forgot: Thank you very much!

Contents

Abstract	iii
Kurzfassung	v
Acknowledgments	vii
1 Introduction	1
2 Theoretical Background	3
2.1 Brief Overview of the Standard Model	3
2.2 Weak Interactions	5
2.2.1 Charged Current Interactions	6
2.2.2 Charged Current Reactions in the Low Energy Limit	8
2.2.3 Neutral Current Interactions	10
2.3 Neutrino-Nucleon Scattering	10
2.3.1 Kinematic Definitions	10
2.3.2 Deep Inelastic Scattering	13
2.3.3 Quasi Elastic Charm Production	15
3 The Experiment	19
3.1 The Neutrino Beam	19
3.2 The Detector	22
3.2.1 The Magnet	22
3.2.2 The Veto Counters	24
3.2.3 The Forward Calorimeter (FCAL)	24
3.2.4 The Drift Chambers (DCH)	25
3.2.5 The Transition Radiation Detector (TRD)	26
3.2.6 The Preshower Detector (PRS)	27
3.2.7 The Electromagnetic Calorimeter (ECAL)	27
3.2.8 The Hadronic Calorimeter (HCAL)	28
3.2.9 The Muon Chambers	29
3.2.10 The Trigger System	30

4	Monte Carlo Simulation	31
4.1	Charged Current Monte Carlo Sample	31
4.1.1	The Neutrino Beam Simulation	31
4.1.2	The Event Generation	32
4.1.3	The Detector Simulation and Event Reconstruction	32
4.1.4	Comparison with Data	32
4.2	Signal Monte Carlo Sample: Quasi Elastic Charm Production	35
4.2.1	The QEC Model of Shrock and Lee	38
4.2.2	The QEC Model of Kovalenko	40
4.2.3	Calculation of the total QEC Cross Section	40
4.2.4	Monte Carlo Generation of QEC Events	42
5	Data Analysis	45
5.1	Introduction	45
5.2	Data Selection	46
5.2.1	Purity of the ν_μ cc Sample	47
5.3	Efficiencies and Normalization of the QEC Signal Monte Carlo Samples	48
5.4	Selection and Identification of V^0 Vertices	49
5.5	Search in the Decay Channel: $\Lambda_c^+ \rightarrow \Lambda \pi^+ \pi^+ \pi^-$	51
5.6	Search in the Decay Channel: $\Lambda_c^+ \rightarrow \Lambda e^+ \nu_e$	55
5.7	Semi-Inclusive Search: $B_c \rightarrow \Lambda + X$	66
5.8	Calculation of Cross Section Limits	68
5.9	Error Estimation	70
5.9.1	Background Uncertainties	71
5.9.2	Uncertainties of the Signal Efficiency	72
5.10	Results	73
6	Conclusion	79
A	Variables for Event Classification	81
	Curriculum Vitae	89

List of Figures

2.1	Vertex graph for the virtual process $f \rightarrow f' + V$	6
2.2	Some examples of first order Feynman diagrams	6
2.3	First order Feynman diagram for the charged current reaction	9
2.4	Charged current neutrino-nucleon scattering	11
2.5	DIS neutrino-nucleon scattering	14
2.6	Total charged current cross section	15
2.7	Feynman diagram for quasi elastic charm production	16
3.1	Schematic layout of the WANF beam line	20
3.2	Composition and energy spectrum of the CERN SPS neutrino beam	21
3.3	Top and side view of the NOMAD detector	23
3.4	Top view of the FCAL	24
3.5	Top view of the TRD setup	27
3.6	An exploded view of the preshower detector	28
3.7	The front view of the HCAL	29
3.8	Layout of the muon chambers	30
4.1	Reconstructed neutrino and muon energies	34
4.2	Number of primary tracks and charge sum	34
4.3	Position of the reconstructed primary vertex	36
4.4	Reconstructed kinematic quantities	37
4.5	Total QEC cross sections for the model of Shrock and Lee and for the model of Kovalenko	42
4.6	Differential QEC cross sections for the model of Shrock and Lee and for the model of Kovalenko	43
5.1	Transverse momentum with respect to the line of flight	50
5.2	Two-body decay of a neutral particle	50
5.3	Podolanski-Armenteros plot	52
5.4	Display of a QEC event with $\Lambda_c^+ \rightarrow \Lambda \pi^+ \pi^+ \pi^-$	52
5.5	ECAL energy deposit by neutral particles	53
5.6	Invariant mass of the hadronic system	56
5.7	Reconstructed invariant mass of the Λ_c^+	57

5.8	Number of charged primary tracks	58
5.9	Display of a QEC event with $\Lambda_c^+ \rightarrow \Lambda e^+ \nu_e$	59
5.10	Electron identification	60
5.11	Invariant mass of the hadronic system	62
5.12	Normalized difference between ECAL energy and DCH momentum	63
5.13	Energy deposited in the PRS	64
5.14	Invariant mass of the hadronic system	67
5.15	Compilation of QEC measurements	77
5.16	Energy dependence of the upper limits	78

List of Tables

2.1	The fermions of the Standard Model	4
2.2	Interactions of the Standard Model	4
2.3	Predicted quasi elastic charm cross sections	18
3.1	Composition of the neutrino beam	22
3.2	Composition of the drift chamber fiducial volume	25
4.1	Threshold energy of QEC production	41
5.1	Efficiencies of the ν_μ cc sample selection	47
5.2	Expected numbers of signal events in the ν_μ cc sample	49
5.3	$\Lambda_c^+ \rightarrow \Lambda \pi^+ \pi^+ \pi^-$: Monte Carlo efficiencies	54
5.4	$\Lambda_c^+ \rightarrow \Lambda \pi^+ \pi^+ \pi^-$: Contribution of inclusive QEC	55
5.5	$\Lambda_c^+ \rightarrow \Lambda \pi^+ \pi^+ \pi^-$: Data efficiencies	58
5.6	$\Lambda_c^+ \rightarrow \Lambda e^+ \nu_e$: Monte Carlo efficiencies	61
5.7	$\Lambda_c^+ \rightarrow \Lambda e^+ \nu_e$: Contribution of inclusive QEC	65
5.8	$\Lambda_c^+ \rightarrow \Lambda e^+ \nu_e$: Data efficiencies	65
5.9	$B_c \rightarrow \Lambda + X$: Monte Carlo efficiencies	68
5.10	$B_c \rightarrow \Lambda + X$: Contribution of inclusive QEC	68
5.11	$B_c \rightarrow \Lambda + X$: Data efficiencies	69
5.12	Errors of the total signal efficiency for $\Lambda_c^+ \rightarrow \Lambda \pi^+ \pi^+ \pi^-$	72
5.13	Errors of the total signal efficiency for $\Lambda_c^+ \rightarrow \Lambda e^+ \nu_e$	72
5.14	Errors of the total signal efficiency for $B_c \rightarrow \Lambda + X$	73
5.15	Upper limits for the signal samples	74
5.16	Total signal efficiencies	74
5.17	Upper limits for the relative the QEC cross sections	74

Chapter 1

Introduction

One of the important discoveries of the last decade has been the convincing evidence for neutrino oscillations which indicate a non-zero neutrino mass and flavor mixing [1, 2, 3]. The accurate determination of mixing angles and mass differences between the neutrinos remains a task of current and future neutrino experiments. For the τ appearance experiments, which search for $\nu_\mu \rightarrow \nu_\tau$ oscillations via the charged current reaction of the ν_τ , it is essential to know the charm production cross section since charmed hadrons constitute one of the main background sources.

Even though the first measurements of charmed baryon production in charged current neutrino reactions were performed in bubble chamber experiments more than 20 years ago [4], there is still little data available compared to the charmed mesons. Near the charm threshold a significant fraction of the charm production might be due to the quasi elastic processes

$$\nu_\mu + n \rightarrow \mu^- + \Lambda_c^+(2285) \quad (1.1)$$

$$\nu_\mu + n \rightarrow \mu^- + \Sigma_c^+(2455) \quad (1.2)$$

$$\nu_\mu + n \rightarrow \mu^- + \Sigma_c^{*+}(2520) \quad (1.3)$$

and

$$\nu_\mu + p \rightarrow \mu^- + \Sigma_c^{++}(2455) \quad (1.4)$$

$$\nu_\mu + p \rightarrow \mu^- + \Sigma_c^{*++}(2530). \quad (1.5)$$

Besides improving the knowledge of the total charm production cross section, the study of these processes can give useful information about the form factors for weak transitions of the nucleon into baryons containing a heavy quark. Also, the determination of the cross section is crucial for the understanding of the quasi elastic processes, since the predictions of the existing theoretical models disagree by more than one order of magnitude among themselves [5, 6, 7, 8, 9, 10, 11, 12]. Furthermore, quasi elastic charm production might offer a possibility for a model independent measurement of the branching fractions of Λ_c^+ decays [13].

Several experiments have searched for quasi elastic charm production processes in the last 25 years, most of them using bubble chambers [14, 15, 16, 17] which suffered from poor statistics. Also, two emulsion experiments have searched for quasi elastic charm events: E531 [18] at Fermilab and CHORUS [19] at CERN. The NOMAD experiment, which was exposed to the CERN SPS wide band neutrino beam, provides data with high statistics and good tracking resolution.

A search for quasi elastic charm production has been undertaken, exploiting the specific characteristics of the events and identifying the charmed baryons via the decays:

$$\Lambda_c^+ \rightarrow \Lambda \pi^+ \pi^+ \pi^- \quad (1.6)$$

$$\Lambda_c^+ \rightarrow \Lambda e^+ \nu_e \quad (1.7)$$

$$\Lambda_c^+, \Sigma_c, \Sigma_c^* \rightarrow \Lambda \text{ anything.} \quad (1.8)$$

In Chapter 2, a brief overview of the Standard Model is given with emphasis on the weak interactions. Also, the kinematics of neutrino-nucleon scattering are explained and a short introduction to the theoretical treatment of quasi elastic charm production is presented.

The CERN SPS wide band neutrino beam and the NOMAD detector are described in Chapter 3.

In Chapter 4, the Monte Carlo simulation used for background estimations is described and a comparison with data is given. Also, two models for quasi elastic charm production [6, 7, 12] are presented explicitly along with their cross section predictions. Furthermore, a short description of the Monte Carlo programs which simulate the signal events is given.

Chapter 5 comprehends an elaborate description of the data analysis, showing all the steps done in order to search for quasi elastic charm events. Also, the tools used to calculate confidence intervals are introduced and an estimation of uncertainties is given. The results, being upper confidence limits for the quasi elastic charm production cross section, are compared with the cross section measurements of other experiments and the influence of the model uncertainty is discussed.

Finally, in Chapter 6 a short summary of the analysis is given and the most important results are recapitulated.

Throughout this thesis, the convention $c = \hbar = 1$ is used for analytic calculations.

Chapter 2

Theoretical Background

2.1 Brief Overview of the Standard Model

Today's understanding of particles and of the interactions between them is summarized in the so called *Standard Model* of particle physics [20, 21, 22, 23]. Initially devised by Glashow, Weinberg and Salam, it includes today the theory of the unified electroweak interactions and Quantum Chromodynamics (QCD), the theory of the strong interactions. The particles of the Standard Model can be divided in two fundamental classes, namely:

- *Fermions* with spin $1/2$ are the particles of which matter is made,
- *Gauge Bosons* with spin 1 act as the mediators of the different interactions.

The fermions are either *leptons* which are not affected by the strong interactions or *quarks* which are the fundamental constituents of the *hadrons*, the particles interacting via the strong force. Leptons and quarks can be grouped into three generations according to their masses as shown in Table 2.1. Ordinary matter consists of the fermions of the first generation. The higher mass fermions of the second and third generation are produced by the high energies of particle accelerators and cosmic rays. For every fermion there is an associated anti-fermion with the same mass but opposite additive quantum numbers.

The fermions interact with each other via the exchange of the gauge bosons listed in Table 2.2. The photon is the gauge boson of the electromagnetic interactions which affects all charged particles. All fermions interact weakly with the exchange of the massive gauge bosons W^\pm and Z^0 . The strong interaction acts only on quarks and is carried by the gluon. To complete the list of the known forces, gravity has to be mentioned. It affects all particles and is assumed to be carried by the graviton, a spin-2 boson. However, since the effects of gravity are negligible when considering the interactions of elementary particles, it will not be discussed further.

The interactions of the Standard Model are based on the principle of local gauge invariance which demands the *Lagrangian* of the theory to be invariant under transformations of the gauge group $SU(3) \times SU(2) \times U(1)$. QCD is governed by the symmetry group $SU(3)$, the electroweak theory by $SU(2) \times U(1)$. The non-Abelian character of $SU(3)$

Quarks			
Generation	Flavor	Charge (e)	Mass (MeV/c ²)
1st	u	$+2/3$	$1.5 - 4$
	d	$-1/3$	$4 - 8$
2nd	c	$+2/3$	$1150 - 1350$
	s	$-1/3$	$80 - 130$
3rd	t	$+2/3$	≈ 178000
	b	$-1/3$	$4100 - 4400$

Leptons			
Generation	Flavor	Charge (e)	Mass (MeV/c ²)
1st	ν_e	0	$< 3 \times 10^{-6}$
	e^-	-1	0.511
2nd	ν_μ	0	< 0.19
	μ^-	-1	105.7
3rd	ν_τ	0	< 18.2
	τ^-	-1	1777

Table 2.1: Properties of the fermions of the Standard Model [24, 25]. Since quarks do not exist as free particles, their masses cannot be measured directly, but have to be derived from hadron properties. Therefore, the values of the quark masses depend on how they are defined. The *constituent* masses of the quarks are inferred from the hadron mass spectra, while the masses that enter as parameters in the QCD Lagrangian are called *current* masses. The values stated in the Table refer to the latter.

Interaction	Gauge boson(s)	Relative strength	Range (m)	Participating fermions
strong	gluons (g)	1	10^{-15}	quarks
electromagnetic	photons (γ)	10^{-2}	∞	all charged
weak	W^\pm, Z^0	10^{-7}	10^{-18}	all
gravitational	[graviton (G)]	10^{-39}	∞	all

Table 2.2: Interactions and corresponding gauge bosons of the Standard Model. The relative strengths of the forces are roughly given for short distance scales of a few GeV [26]. Since there is no quantized renormalizable theory of gravity in the Standard Model, the graviton has to be considered a hypothetical particle.

and $SU(2)$ leads to self-interactions between the gauge bosons. In the case of QCD, this self-interaction accounts for the fact that quarks are confined to hadrons, i. e., they cannot be observed as individual particles. However, probed at high energies they begin to behave as free particles, a property referred to as asymptotic freedom.

Whereas the gauge bosons of the electromagnetic and the strong interaction are massless, the theory of the weak interactions must accomplish the massive W^\pm and Z^0 gauge particles. In order to achieve this, while retaining the gauge invariant structure of the theory, the Higgs mechanism was introduced. This, however, requires at least one additional particle, the Higgs particle, yet to be found.

Although the Standard Model is a mathematically consistent, renormalizable field theory, it cannot be the final answer [27]. Even if the recently discovered neutrino masses were incorporated, more fundamental shortcomings can be noted. For example, the minimal version of the model has more than 20 parameters, which, as most physicists believe, are too many for a fundamental theory. Although incorporated in the Standard Model, there is no explanation for the fundamental fact of charge quantization or for the CP (charge-conjugation and parity) violating interactions. There is no explanation for the existence of the heavier fermion generations which have no obvious role in nature. Furthermore, there is no prediction of the fermion masses which vary by five orders of magnitude. As accelerators reach higher energies and results become more precise answers for some of the current questions will certainly be found.

2.2 Weak Interactions

Since this thesis is about neutrino physics, the weak interactions will be discussed in some detail. According to Quantum Field Theory, the fundamental processes of fermion interactions are of the kind $f \rightarrow f' + V$ where a fermion f passes into a fermion f' thereby emitting a vector boson V (f - f' - V -vertex). These processes are governed by the Lagrangian given at a point x in space-time:

$$\begin{aligned}\mathcal{L}(x) &= g \cdot \bar{\psi}_{f'}(x) \Gamma_\alpha(x) \psi_f(x) \cdot V^\alpha(x) + \text{Herm. conj.} \\ &= g \cdot j_\alpha(x) \cdot V^\alpha(x) + \text{Herm. conj.}\end{aligned}\tag{2.1}$$

with the fermion current

$$j_\alpha(x) = \bar{\psi}_{f'}(x) \Gamma_\alpha(x) \psi_f(x).\tag{2.2}$$

The *Dirac spinor* ψ_f is the field operator which annihilates a fermion f or creates an anti-fermion \bar{f} ; the field operator $\bar{\psi}_{f'} = \psi_{f'}^\dagger \gamma^0$ creates a fermion f' or annihilates an anti-fermion \bar{f}' . This means, the ordered product of the two, including a 4×4 -matrix Γ which depends on the interaction, causes a transition from a fermion f in the initial state to a fermion f' in the final state. Together with the vector field operator V^α , which creates a boson V or annihilates a boson \bar{V} , this describes the desired process shown in Figure 2.1.

For physical particles these processes are forbidden. The 4-momentum conservation at the vertex can only be fulfilled if one of the particles is *off-shell* (or *virtual*), i. e., the

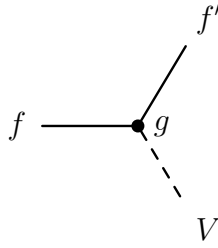


Figure 2.1: Vertex graph for the virtual process $f \rightarrow f' + V$ with coupling constant g .

square of its 4-momentum is not equal to its mass. A physical reaction is obtained as a combination of e. g. two of these f - f' - V -vertices by connecting them with one of the participating particles (see Figure 2.2). Since this particle is not observable, it may be off-shell, thereby allowing the in- and outgoing particles to be real.

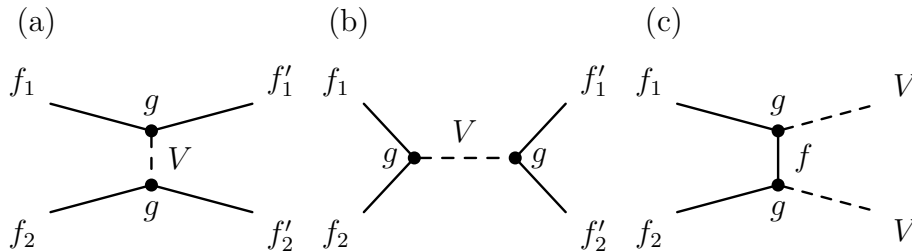


Figure 2.2: Some examples of first order *Feynman diagrams* obtained as a combination of two vertex graphs. Diagram (a) and (b) correspond to the fermion scattering $f_1 + f_2 \rightarrow f'_1 + f'_2$ while (c) shows the annihilation process $f_1 + f_2 \rightarrow V + V$. The time direction is from left to right.

In the case of the weak interactions, two classes have to be distinguished, namely the charged current (cc) interactions and the neutral current (nc) interactions. Also, there is a slightly different treatment for quarks and leptons due the small and yet undetermined masses of the neutrinos

2.2.1 Charged Current Interactions

The emission of a charged vector boson W^\pm causes a transition between the left-handed fermions within a weak isospin doublet, i. e., the doublet of the two eigenstates¹ with total weak isospin $1/2$:

$$\begin{pmatrix} f^\uparrow \\ f^\downarrow \end{pmatrix}. \quad (2.3)$$

¹The particles f^\uparrow and f^\downarrow have weak isospin $\pm 1/2$ along the “z-axis”.

These processes $f^\downarrow \rightarrow f^\uparrow + W^-$ and $f^\uparrow \rightarrow f^\downarrow + W^+$ are governed by the Lagrangian

$$\mathcal{L}^{\text{cc}} = g_{\text{cc}} \cdot (j_{\text{cc}}^{\alpha+} \cdot W_\alpha^+ + j_{\text{cc}}^{\alpha-} \cdot W_\alpha^-) \quad (2.4)$$

with the vector field operators² W_α^\pm and the fermion currents $j_{\text{cc}}^{\alpha^\pm}$ summed over the 3 doublets for leptons and quarks respectively:

$$j_\alpha^{\text{cc}+} = \sum_{i=1}^3 \bar{l}_i^\uparrow \gamma_\alpha (1 - \gamma_5) l_i^\downarrow + \sum_{i=1}^3 \bar{q}_i^\uparrow \gamma_\alpha (1 - \gamma_5) q_i^\downarrow. \quad (2.5)$$

Here, the field operators ψ_f have been replaced by the particle symbols ($l \leftrightarrow$ leptons, $q \leftrightarrow$ quarks) for simplicity. The current $j_\alpha^{\text{cc}-}$ is the Hermitian conjugate of $j_\alpha^{\text{cc}+}$. The projection operator $\frac{1}{2}(1 - \gamma_5)$ assures that only leptons with left-handed chirality are taking part in the process:

$$\bar{f}^\uparrow \gamma_\alpha \frac{1}{2}(1 - \gamma_5) f^\downarrow = \bar{f}_L^\uparrow \gamma_\alpha f_L^\downarrow. \quad (2.6)$$

For massive fermions the weak isospin eigenstates are generally a mixture of the mass eigenstates. A unitary (3×3)-matrix describing the relation between the two sets can be introduced:

$$\begin{pmatrix} f_1^\downarrow \\ f_2^\downarrow \\ f_3^\downarrow \end{pmatrix} = U \begin{pmatrix} f_{1,m}^\downarrow \\ f_{2,m}^\downarrow \\ f_{3,m}^\downarrow \end{pmatrix}, \quad (2.7)$$

or equivalently for f_i^\uparrow . The charged fermion current can now be rewritten as a sum over the physical fermions:

$$j_\alpha^{\text{cc}} = (\bar{\nu}_{1,m}, \bar{\nu}_{2,m}, \bar{\nu}_{3,m}) U_l^+ \gamma_\alpha (1 - \gamma_5) \begin{pmatrix} e \\ \mu \\ \tau \end{pmatrix} + (\bar{u}, \bar{c}, \bar{t}) \gamma_\alpha (1 - \gamma_5) U_q \begin{pmatrix} d \\ s \\ b \end{pmatrix}. \quad (2.8)$$

The quarks and charged leptons correspond to the particles shown in Table 2.1. Equation (2.7) essentially implicates that charged current weak interactions cause transitions between quarks or leptons of all generations.

Charged Leptonic Current

The recently found neutrino oscillations imply that the neutrinos ν_e , ν_μ and ν_τ do not correspond to the mass eigenstates $\nu_{i,m}$. This means, the mixing matrix U_l is not diagonal [25]. In fact, current limits indicate mixing angles which correspond to almost maximal mixing for $\nu_e \leftrightarrow \nu_\mu$ and $\nu_\mu \leftrightarrow \nu_\tau$. Also, there might be more than three neutrinos taking part in the mixing. Because of the small masses of the neutrinos and since they interact only weakly, the mass eigenstates are not yet directly observable, but have to be determined

² W_α^+ is the operator that annihilates a W^+ or creates W^-

by means of oscillation rates and cosmological measurements. The charged leptonic current is therefore usually written in terms of the weak eigenstates:

$$j_{\alpha}^{\text{cc},l^{+}} = (\bar{\nu}_e, \bar{\nu}_{\mu}, \bar{\nu}_{\tau}) \gamma_{\alpha} (1 - \gamma_5) \begin{pmatrix} e \\ \mu \\ \tau \end{pmatrix}. \quad (2.9)$$

Charged Quark Current

The mixing in the quark sector is described by the Cabibbo-Kobayashi-Maskawa (CKM) Matrix:

$$U_q = \begin{pmatrix} U_{ud} & U_{us} & U_{ub} \\ U_{cd} & U_{cs} & U_{cb} \\ U_{td} & U_{ts} & U_{tb} \end{pmatrix}. \quad (2.10)$$

The matrix elements $|U_{ij}|^2$ give the probability of the quark q_i^{\uparrow} to pass into the quark q_j^{\downarrow} . Conservation of probability requires the CKM matrix to be unitary. In principle, the individual matrix elements can all be measured in weak decays of the relevant quarks or in deep inelastic neutrino-nucleon scattering. The 90 % confidence limits on the magnitude of the matrix elements, as given in [25], are:

$$\begin{pmatrix} 0.9739 - 0.9751 & 0.221 - 0.227 & 0.0029 - 0.0045 \\ 0.221 - 0.227 & 0.9730 - 0.9744 & 0.039 - 0.044 \\ 0.0048 - 0.014 & 0.037 - 0.043 & 0.9990 - 0.9992 \end{pmatrix}. \quad (2.11)$$

The standard parametrization with three mixing angles and one phase was originally proposed by Chau and Keung [28]:

$$U_q = \begin{pmatrix} c_{12}c_{13} & s_{12}c_{13} & s_{13}e^{-i\delta_{13}} \\ -s_{12}c_{23} - c_{12}s_{23}s_{13}e^{i\delta_{13}} & c_{12}c_{23} - s_{12}s_{23}s_{13}e^{i\delta_{13}} & s_{23}c_{13} \\ s_{12}s_{23} - c_{12}c_{23}s_{13}e^{i\delta_{13}} & -c_{12}s_{23} - s_{12}c_{23}s_{13}e^{i\delta_{13}} & c_{23}c_{13} \end{pmatrix} \quad (2.12)$$

with $c_{ij} = \cos \theta_{ij}$ and $s_{ij} = \sin \theta_{ij}$ for the generation labels $i, j = 1, 2, 3$. The phase δ_{ij} is responsible for CP violation. The advantage of this parametrization is that if one of the angles θ_{ij} vanishes, so does the mixing between the two generations. In the limit $\theta_{23} = \theta_{13} = 0$ the third generation decouples, resulting in the usual Cabibbo mixing of the first two generations with the Cabibbo angle θ_{12} .

In contrast to the leptonic sector, the mixing in the quark sector is easily observable, since the mass differences are bigger and the quarks interact also via the strong force. If a mass eigenstate q_m^{\uparrow} changes into a quark q_{\downarrow} , the strong interaction forces the latter during the process of *hadronization* into a mass eigenstate q_m^{\downarrow} .

2.2.2 Charged Current Reactions in the Low Energy Limit

The combination of the total weak current $j_{\alpha}^{\text{cc}+}$ with its Hermitian conjugate $j_{\alpha}^{\text{cc}-}$ by the exchange of a W boson, i. e., the connection of $f_1 \rightarrow f_1' + W$ and $f_2 + W \rightarrow f_2'$, results in

weak charged current reactions of the form:

$$f_1 + f_2 \rightarrow f'_1 + f'_2 \quad (2.13)$$

The *matrix element* of such a process in lowest order of perturbation theory is given by

$$\mathcal{M} = g_{cc}^2 \cdot \langle f'_1 | j_{\alpha}^{cc+} | f_1 \rangle \cdot \frac{-g^{\alpha\beta} + q^{\alpha}q^{\beta}/m_W^2}{q^2 - m_W^2} \cdot \langle f'_2 | j_{\beta}^{cc-} | f_2 \rangle \quad (2.14)$$

where

$$\frac{-g^{\alpha\beta} + q^{\alpha}q^{\beta}/m_W^2}{q^2 - m_W^2} \equiv P^{\alpha\beta} \quad (2.15)$$

is the *W-propagator* which describes the exchange of a *W* boson with 4-momentum q . The *W* is generally *off-shell* (or *virtual*), i. e. $q^2 \neq m_W^2$. The corresponding Feynman diagram is shown in Figure 2.3.

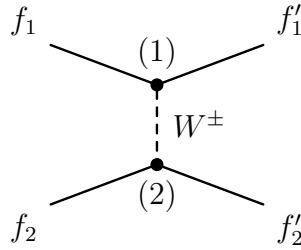


Figure 2.3: First order Feynman diagram for the charged current reaction $f_1 + f_2 \rightarrow f'_1 + f'_2$. The virtual *W* boson is emitted at the space-time-position (1) and absorbed at the space-time-position (2) (or the other way around).

In the limit of low center of mass energies $\sqrt{s} \ll m_W$, the momentum transfer becomes small, $q^2 \ll m_W^2$, and thus,

$$P^{\alpha\beta} \simeq \frac{g^{\alpha\beta}}{m_W^2}. \quad (2.16)$$

Hence, the matrix element (2.14) can be written as

$$\begin{aligned} \mathcal{M} &\simeq \frac{g_{cc}}{m_W^2} \cdot \langle f'_1 | j_{\alpha}^{cc+} | f_1 \rangle \langle f'_2 | j_{\alpha}^{cc-} | f_2 \rangle \\ &= \frac{g_{cc}}{m_W^2} \cdot \langle f'_1 f'_2 | j_{\alpha}^{cc+} \cdot j_{\alpha}^{cc-} | f_1 f_2 \rangle \\ &= \frac{G_F}{\sqrt{2}} \cdot \langle f'_1 f'_2 | j_{\alpha}^{cc+} \cdot j_{\alpha}^{cc-} | f_1 f_2 \rangle \end{aligned} \quad (2.17)$$

and corresponds to an effective Lagrangian:

$$\mathcal{L} = \frac{G_F}{\sqrt{2}} \cdot j_{\alpha}^{cc+} \cdot j_{\alpha}^{cc-} \quad (2.18)$$

with the well known *Fermi constant* G_F . Due to the vanishing range of the weak interaction in the low energy limit, this approximation is usually referred to as point like four-fermion-interaction or current-current-interaction.

2.2.3 Neutral Current Interactions

The fundamental process of the weak neutral current interactions is the emission of a Z^0 boson, $f \rightarrow f + Z^0$. The Z boson, just as the photon, is a mixture of the third gauge field of the $SU(2)$ symmetry group (the other two being W^+ and W^-) and the gauge field of the $U(1)$ symmetry group. The form of the weak neutral current, therefore, also depends on whether or not the fermions carry charge. The corresponding Lagrangian is given by

$$\mathcal{L} = g_{\text{nc}} \cdot j_{\text{nc}}^\alpha \cdot Z_\alpha^0. \quad (2.19)$$

The coupling constant g_{nc} is related to the charged current coupling constants g_{cc} by

$$g_{\text{nc}} = \sqrt{2}g_{\text{cc}} \frac{1}{\cos \theta_W} = \sqrt{2}g_{\text{cc}} \frac{m_Z}{m_W} \quad (2.20)$$

where θ_W is the *Weinberg angle* defined by $\cos \theta_W = m_W/m_Z$. The neutral current is summed over all fermions:

$$\begin{aligned} j_\alpha^{\text{nc}} &= \sum_i \bar{f}^i [\gamma_\alpha (T_3^i (1 - \gamma_5) - 2Q^i \sin^2 \theta_W)] f^i \\ &= \sum_i \bar{f}^i \gamma_\alpha (g_V^i - g_A^i \gamma_5) f^i \end{aligned} \quad (2.21)$$

and

$$g_V^i = T_3^i - 2Q^i \sin^2 \theta_W \quad (2.22)$$

$$g_A^i = T_3^i \quad (2.23)$$

where T_3 is the weak isospin of the left-handed component of the fermion along the z -axis, i. e. $\pm 1/2$, and Q is the charge of the fermion in units of e .

2.3 Neutrino-Nucleon Scattering

As neutrinos are structureless and comparatively easy to produce in accelerators, they make an exceptional probe of hadronic matter. Investigating neutrino collisions in fixed target experiments is an excellent means for retrieving information about the structure of protons and neutrons. In order to provide a basis for further discussions of such scattering processes, some definitions have to be introduced. All the relevant expressions are given for charged current interactions, since this is what this thesis is concerned with. Also, since referring to the NOMAD experiment, the neutrino is always assumed to be a ν_μ .

2.3.1 Kinematic Definitions

Figure 2.4(a) shows the Feynman diagram for neutrino-nucleon scattering:

$$\nu_\mu + N \rightarrow \mu^- + X \quad (2.24)$$

where X denotes a not yet specified hadronic final state. The variables k and p_N denote the 4-momenta of the particles in the initial state, the neutrino and the nucleon. The 4-momentum of the final state muon is k' . The hadronic final state is somewhat more complex as it may consist of several particles. Considered as a whole, it is assigned with the 4-momentum p_X which is a sum of all the individual hadron 4-momenta p_h . The W-boson emitted by the neutrino carries the four-momentum q which will be called 4-momentum transfer from here on.

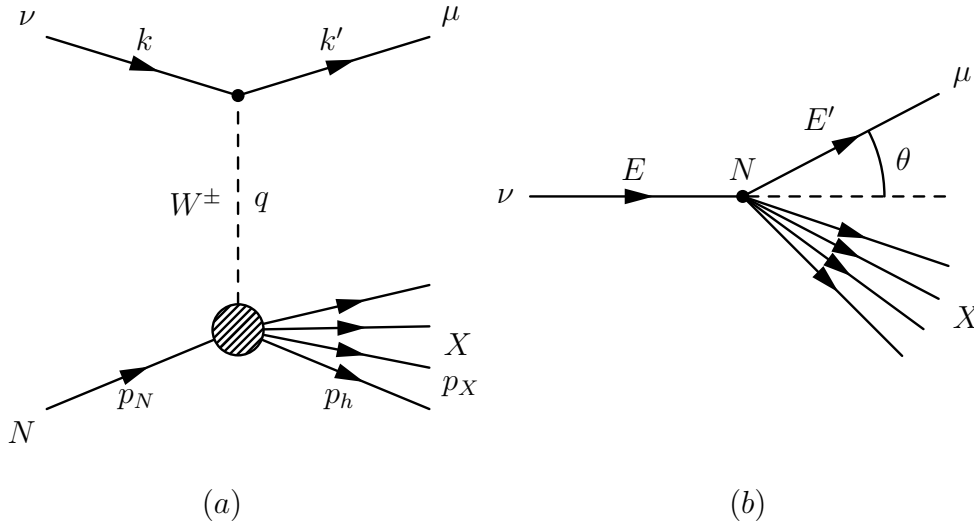


Figure 2.4: Diagram for the reaction $\nu + N \rightarrow \mu + X$. (a) Feynman diagram, (b) in the laboratory frame.

In the rest frame of the nucleon, which corresponds to the laboratory system (neglecting the Fermi motion) shown in Figure 2.4(b), these momenta can be written as:

$$\begin{aligned} k &= (E, \mathbf{k}), & k' &= (E', \mathbf{k}'), & q &= (\nu, \mathbf{q}) \\ p_N &= (M, \mathbf{0}), & p_X &= (E_X, \mathbf{p}_X), & p_h &= (E_h, \mathbf{p}_h) \end{aligned} \quad (2.25)$$

with M being the nucleon mass, $M = m_N$. Neglecting the mass of the μ , the kinematic event variables can be expressed as follows:³

- The total energy in the center of mass system \sqrt{s} :

$$s = (k + p_N)^2 = 2ME + M^2 \approx 2ME \quad (2.26)$$

³The approximation “ \approx ” indicates the neglected mass m_μ , whereas “ \simeq ” only holds for $E \gg M$

- The negative square of the 4-momentum transfer Q^2 :

$$Q^2 = -q^2 = -(k - k')^2 = -(E - E')^2 + (\mathbf{k} - \mathbf{k}')^2 \simeq 4EE' \sin^2 \frac{\theta}{2} > 0. \quad (2.27)$$

where $\theta = \theta_\mu$ is the scattering angle of the muon.

- The energy transfer ν in the laboratory frame:

$$\nu = \frac{q \cdot p_N}{M} = E - E' = E_X - M \quad (2.28)$$

and

$$\nu_{\max} \simeq \frac{2E^2}{2E + Mx_{\text{Bj}}} = E \quad \text{for } x_{\text{Bj}} = 0. \quad (2.29)$$

with x_{Bj} defined below in equation (2.32).

- The total energy W of the outgoing hadrons X in their center of mass frame corresponds to an effective mass of the hadronic final state:

$$W^2 = p_X^2 = E_X^2 - \mathbf{p}_X^2 = (E - E' + M)^2 - (\mathbf{k} - \mathbf{k}')^2 = -Q^2 + 2M\nu + M^2 \quad (2.30)$$

with

$$\begin{aligned} W_{\max}^2 &\simeq 2ME + M^2 = s & (2.31) \\ \text{where } \nu &= \nu_{\max} \simeq E \\ Q^2 &\simeq 0 \end{aligned}$$

- The Bjorken scaling variable x_{Bj} :⁴

$$x_{\text{Bj}} = \frac{-q^2}{2q \cdot p_N} = \frac{Q^2}{2M\nu} \quad \text{with: } 0 \leq x_{\text{Bj}} \leq 1. \quad (2.32)$$

Combining equation (2.30) and (2.32) yields:

$$W^2 = M^2 + Q^2 \left(\frac{1}{x_{\text{Bj}}} - 1 \right). \quad (2.33)$$

- The inelasticity or relative energy transfer y :⁴

$$\begin{aligned} y &= \frac{q \cdot p_N}{k \cdot p_N} = \frac{\nu}{E} = 1 - \frac{E'}{E} = \frac{Q^2}{2MEx_{\text{Bj}}} & (2.34) \\ \text{with: } 0 &\leq y \leq \left(1 + \frac{Mx_{\text{Bj}}}{2E} \right)^{-1} \approx 1 \end{aligned}$$

⁴The boundaries for x_{Bj} and y are given, neglecting the mass m_μ of the outgoing muon.

From (2.32) and (2.34) another useful relation can be given:

$$yx_{\text{Bj}} = \frac{Q^2}{2ME} = \frac{Q^2}{s - M^2} \quad (2.35)$$

For a given neutrino energy $E = E_\nu$, the measurement of two independent variables, e.g. (E', θ) or (Q^2, ν) or (x, Q^2) or (x, y) , is sufficient to characterize a scattering event of the form (2.24).

2.3.2 Deep Inelastic Scattering

If a neutrino is scattered off a nucleon with sufficiently large Q^2 , the nucleon will break apart. In the limit $Q^2 \gg M^2$, referred to as *deep inelastic scattering* (DIS), this reaction can be described as scattering between a neutrino and a free quark with momentum $p_q = \xi p_N$ (see Figure 2.5). It can be shown that in lowest order perturbation theory $\xi = x_{\text{Bj}}$, i. e. the Bjorken scaling variable x_{Bj} is equal to the fraction of the nucleon momentum that is carried by the interacting quark. The quark content of a nucleon is specified via the quark distribution or *parton density functions*⁵ $q(\xi)$ which are defined as follows:

$$q(\xi)d\xi = \text{Number of quarks } q \text{ in the nucleon with a momentum fraction between } \xi \text{ and } \xi + d\xi. \quad (2.36)$$

The distributions $u(\xi)$ and $d(\xi)$ can be divided into *valence* quark and *sea* quark distributions:

$$u(\xi) = u_V(\xi) + u_S(\xi) \quad (2.37)$$

$$d(\xi) = d_V(\xi) + d_S(\xi). \quad (2.38)$$

For symmetry reasons it is assumed that the following relations hold for the sea quark distributions:

$$\begin{aligned} u_S(\xi) &= \bar{u}(\xi) & s(\xi) &= \bar{s}(\xi) \\ d_S(\xi) &= \bar{d}(\xi) & c(\xi) &= \bar{c}(\xi) \end{aligned} \quad (2.39)$$

where the $\bar{q}(\xi)$ denote the anti-quark distributions. For a proton consisting of three valence quarks, two u and one d , the distributions must fulfill:

$$\int_0^1 u_V(\xi)d\xi = \int_0^1 [u(\xi) - \bar{u}(\xi)]d\xi = 2 \quad (2.40)$$

$$\int_0^1 d_V(\xi)d\xi = \int_0^1 [d(\xi) - \bar{d}(\xi)]d\xi = 1. \quad (2.41)$$

⁵The distribution functions $q(\xi)$ should not be confused with the Dirac spinors $f(x)$ introduced in Section 2.2

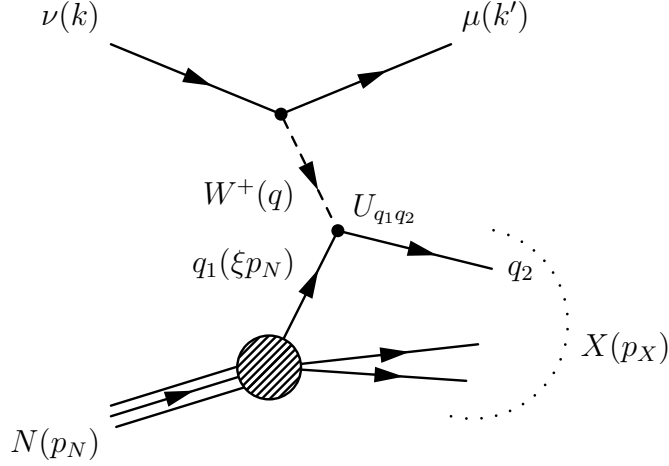


Figure 2.5: Feynman diagram for DIS neutrino-nucleon scattering. The neutrino scatters off a quasi free quark q_1 causing the reaction $\nu q_1 \rightarrow \mu q_2$. The amplitude for this process is proportional to the element, $U_{q_1 q_2}$, of the CKM matrix.

In lowest order the differential cross section for deep inelastic neutrino-nucleon scattering can then be given as an incoherent sum of the differential cross sections for elastic neutrino-quark scattering:

$$\frac{d\sigma}{dx_{\text{Bj}} dy} = \sum_{q, q'} q(x_{\text{Bj}}) \frac{d\sigma}{dy}(\nu q \rightarrow \mu^- q') + \sum_{\bar{q}, \bar{q}'} \bar{q}(x_{\text{Bj}}) \frac{d\sigma}{dy}(\nu \bar{q} \rightarrow \mu^- \bar{q}'). \quad (2.42)$$

The differential cross sections $d\sigma/dy$ correspond to scattering processes of elementary fermions and can easily be calculated. Neglecting the W-propagator for not too high energies (see Section 2.2.2: $s x_{\text{Bj}} \ll m_W^2$), they are given by

$$\frac{d\sigma}{dy}(\nu q \rightarrow \mu^- q') = \frac{2G_F^2}{\pi} x_{\text{Bj}} M E |U_{qq'}|^2 \quad (2.43)$$

and

$$\frac{d\sigma}{dy}(\nu \bar{q} \rightarrow \mu^- \bar{q}') = \frac{2G_F^2}{\pi} x_{\text{Bj}} M E |U_{qq'}|^2 (1-y)^2 \quad (2.44)$$

where $U_{qq'}$ are the elements of the CKM matrix. Taking advantage of $|U_{ud}|^2 + |U_{cd}|^2 \simeq |U_{us}|^2 + |U_{cs}|^2 \simeq 1$, the cross section (2.42) becomes

$$\frac{d\sigma}{dx_{\text{Bj}} dy}(\nu N) = \sigma_0 \cdot 2x_{\text{Bj}} ([d(x_{\text{Bj}}) + s(x_{\text{Bj}})] + [\bar{u}(x_{\text{Bj}}) + \bar{c}(x_{\text{Bj}})](1-y)^2) \quad (2.45)$$

for W above the charm threshold ($W > 2.5 \text{ GeV}/c^2$), with

$$\sigma_0 = \frac{G_F^2 M E}{\pi} = 1.538 \times 10^{-38} \frac{\text{cm}^2}{\text{GeV}} \cdot E. \quad (2.46)$$

An integration over x_{Bj} and y yields the total cross sections which are linear functions of the neutrino energy. As shown in Figure 2.6, this behavior is well confirmed by experiments.

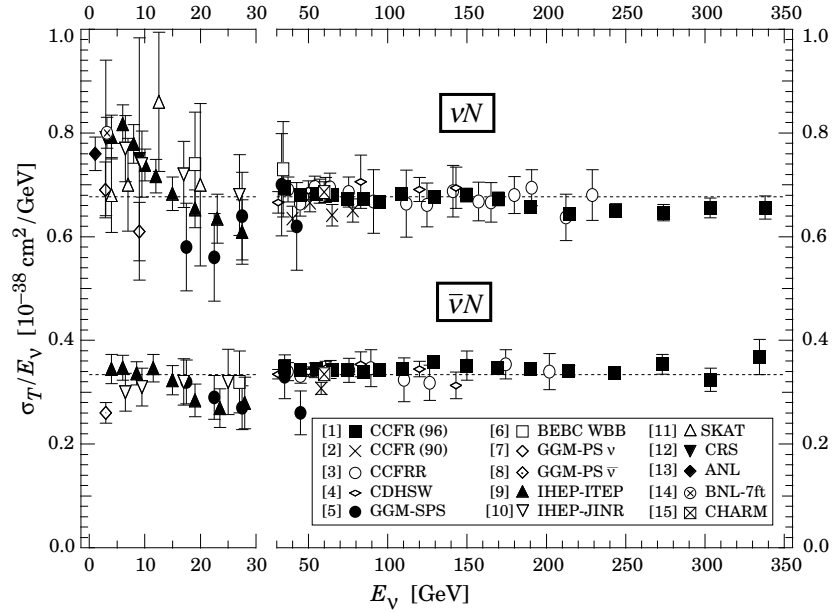


Figure 2.6: σ_{cc}/E_ν for the total charged current cross section of neutrino- and anti-neutrino-nucleon scattering, as a function of the neutrino energy. The original plot as well as the references of the individual measurements can be found in [29].

2.3.3 Quasi Elastic Charm Production

In quasi elastic scattering events the neutrino interacts with the nucleon as a whole and leaves it intact. As in the case of elastic scattering, the reaction has only one degree of freedom because it involves two incoming and two outgoing particles with definite masses. Due to the mass difference between the initial and the final state baryon, as well as between the neutrino and the charged lepton, the charged current process is not completely elastic. The most prominent and well measured quasi elastic processes are

$$\begin{aligned} \nu_\mu + n &\rightarrow \mu^- + p & E_{\text{thr}} &= 110 \text{ MeV} \\ \bar{\nu}_\mu + p &\rightarrow \mu^+ + n & E_{\text{thr}} &= 113 \text{ MeV} \end{aligned} \quad (2.47)$$

where for neutrino energies above the threshold energy E_{thr} a transition between the quarks of the first generation $u \leftrightarrow d$ is induced. As a consequence of the quark mixing, the same mechanism should be able to produce charmed baryons quasi elastically in the following reactions:

$$\nu_\mu + n \rightarrow \mu^- + \Lambda_c^+(2285) \quad (2.48)$$

$$\nu_\mu + n \rightarrow \mu^- + \Sigma_c^+(2455) \quad (2.49)$$

$$\nu_\mu + n \rightarrow \mu^- + \Sigma_c^{*+}(2520) \quad (2.50)$$

and

$$\nu_\mu + p \rightarrow \mu^- + \Sigma_c^{++}(2455) \quad (2.51)$$

$$\nu_\mu + p \rightarrow \mu^- + \Sigma_c^{*++}(2530). \quad (2.52)$$

In the processes (2.48)-(2.52) a d quark has to change into a c quark. Hence, they are all *Cabibbo suppressed*, i. e., they have a cross section proportional to $\sin^2 \theta_c \simeq 0.05$. Since for *quasi elastic charm production* (QEC) the hadronic final state consists of only one charmed baryon, the threshold energy is lower than for DIS charm production where the hadronic final state must involve at least one baryon and one charmed meson. The lower bound for the energy of the hadronic system is thus given by:

$$W_{\text{QEC}} > m_{\Lambda_c^+} = 2285 \text{ MeV}/c^2 \quad (2.53)$$

and

$$W_{\text{DIS}} > m_p + m_{D^0} = 2802 \text{ MeV}/c^2 \quad (2.54)$$

for QEC and DIS respectively. The matrix element for the QEC process, shown in Figure

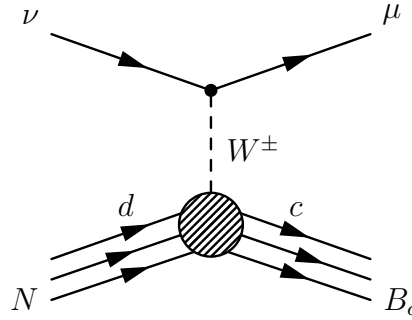


Figure 2.7: Feynman diagram for quasi elastic charm production.

2.7, can be written as⁶:

$$\mathcal{M} = \frac{G_F \sin \theta_C}{\sqrt{2}} \bar{u}_\mu(k') \gamma_\alpha (1 - \gamma_5) u_\nu(k) \langle B_c(p') | J_{D^+}^\alpha | N(p) \rangle \quad (2.55)$$

where N and B_c denote the initial and final state baryons, and the hadronic current $J_{D^+}^\alpha$ describes the quasi elastic transition. In contrast to DIS, the hadronic current $J_{D^+}^\alpha$ is not calculable with perturbative QCD because the q^2 dependent, effective coupling constant of the strong interactions, α_s , is of the order of one in this kinematic region. However, if the effective interaction is assumed to be of the V-A type, the general form of the matrix element of the hadronic current [30, 31, 32] is given by

$$\langle B_c(p') | J_{D^+}^\alpha | N(p) \rangle = \bar{u}_{B_c}(p') \Gamma^\alpha u_N(p) \quad (2.56)$$

⁶Here, the $u_f(p)$ denotes the spinor of the particle f in “momentum-space”.

and

$$\Gamma^\alpha = \gamma^\alpha(g_V + g_A\gamma_5) + \frac{i\sigma^{\alpha\beta}}{(m_N + m_{B_c})}q_\beta(f_V + f_A\gamma_5) + iq^\alpha(h_V + h_A\gamma_5) \quad (2.57)$$

with

$$\sigma^{\alpha\beta} = \frac{i}{2}(\gamma^\alpha\gamma^\beta - \gamma^\beta\gamma^\alpha). \quad (2.58)$$

In general, the form factors g_V , g_A , f_V , f_A , h_V , h_A are complex and depend on q^2 . The invariance under *time reversal* (T) implies, however, that all the form factors in (2.57) are real. If *charge symmetry* is assumed, the form factors f_A and h_V , corresponding to the second class currents, have to be imaginary, hence

$$f_A = h_V = 0. \quad (2.59)$$

In other words, there are no second class currents if both T invariance and charge symmetry is assumed. The term corresponding to the form factor h_A can be neglected, since it gives a contribution proportional to the muon mass. It can be shown that only three combinations of the six form factors can be determined if the helicities of the leptons are not measured [30]. Neglecting the muon mass, the cross section can be written as:

$$\frac{d\sigma}{dQ^2} = \frac{G_F^2 \sin^2 \theta_C}{8\pi E^2} \left[-2q^2 W_1 + (4EE' + q^2)W_2 + \frac{E + E'}{m_N} q^2 W_3 \right] \quad (2.60)$$

with structure functions

$$W_1 = \frac{1}{4m_N^2} \{ [(m_{B_c} - m_N)^2 - q^2](g_V + f_V)^2 + [(m_{B_c} + m_N)^2 - q^2]g_A^2 \}, \quad (2.61)$$

$$W_2 = g_V^2 - \frac{q^2}{(m_N + m_{B_c})^2} f_V^2 + g_A^2 \quad (2.62)$$

and

$$W_3 = 2g_A(g_V + f_V) \quad (2.63)$$

Since the center of mass energy of the hadronic final state W is fixed to the mass of the charmed baryon, the reaction has only one degree of freedom. For a given neutrino energy a quasi elastic event can therefore be characterized by a single variable, e. g. Q^2 .

Many authors have given predictions for the cross sections of QEC, based on the formula (2.60). An overview of the various results is given in Table 2.3, where the cross section values are given for a neutrino energy of 10 GeV. A common feature of all the models is a nearly constant cross section for neutrino energies above 15 GeV. The differences between the predictions, which can be more than one order of magnitude, arise from the fact that the form factors cannot be established on the basis of the theory. In the calculations [5, 6, 7, 8, 9, 10, 11] the q^2 dependence of the form factors is parametrized with dipole formulas

$$D(q^2) \propto \frac{1}{(1 - \frac{q^2}{m_{ex}^2})^2} \quad (\text{dipole}) \quad (2.64)$$

$$m_{ex} = \text{mass of the virtual exchange meson}$$

Process σ in 10^{-40} cm ²	$\nu_\mu n \rightarrow \mu \Lambda_c^+$		$\nu_\mu n \rightarrow \mu \Sigma_c^+$		$\nu_\mu p \rightarrow \mu \Sigma_c^{++}$	
	σ	σ/σ_{cc}	σ	σ/σ_{cc}	σ	σ/σ_{cc}
Finjord, Ranvndal [5]	1.2	0.18 %	0.06	0.009 %	0.12	0.018 %
Shrock, Lee [6, 7]	23.0	3.4 %	5.0	0.74 %	9.0	1.3 %
Avilez et al [8, 9, 10]	41.0	6.1 %	—	—	8.4	1.3 %
Amer et al [11]	3.2	0.48 %	0.6	0.089 %	1.1	0.17 %
Kovalenko [12]	5.0	0.74 %	1.5	0.22 %	3.0	0.45 %

Table 2.3: Predicted QEC production cross sections for a neutrino energy of 10 GeV. Also, the production cross section relative to the total charged current cross section is given.

which are the empirical result of the analysis of experimental data on the electromagnetic and weak nucleon form factors.

In this thesis the calculations of Kovalenko [12] and those of Shrock and Lee [6, 7] are used. The model of Kovalenko tries to give an upper limit for the QEC cross section by taking advantage of the *local duality* [33], which establishes a relation between the structure function $F^{th}(x, Q^2)$ of DIS, calculated in QCD, and the observed structure function $F^{ph}(x, Q^2)$, which at small Q^2 contains resonance peaks corresponding to the ground and excited states of baryons. The average of the two structure functions coincides to good accuracy, both, over the whole range of variation $0 \leq x \leq 1$ (global duality)

$$\int_0^1 [F^{th}(x, Q^2) - F^{ph}(x, Q^2)] dx \simeq 0, \quad (2.65)$$

as well as in the vicinity of an individual resonance $x_{\min} \leq x \leq x_{\max}$ (local duality)

$$\int_{x_{\min}}^{x_{\max}} [F^{th}(x, Q^2) - F^{ph}(x, Q^2)] dx \simeq 0. \quad (2.66)$$

A modified version of these relations, taking into account some of the dominant corrections of $F^{th}(x, Q^2)$ in the region of small and moderate Q^2 , can be used for an estimation of the structure functions W_1 , W_2 and W_3 .

The choice of the calculations of Shrock and Lee as a reference model is somewhat arbitrary in the sense that there are no fundamental formal discrepancies compared to the models [5, 8, 9, 10, 11]. Using the approximate $SU(4)$ symmetry of the strong interaction⁷, the form factors in the model of Shrock and Lee are derived from those found in the reactions (2.47) and the neutron decay. The form factors are combinations of dipole terms with parameters m_{ex} being set to the masses of the exchanged charmed mesons. A more detailed description of the two models will be given in Section 4.2.

⁷If the masses of the quarks u, d, c, s are assumed to be equal, the strong interaction becomes invariant under $SU(4)$ “rotations” of these quark flavors

Chapter 3

The Experiment

The NOMAD (Neutrino Oscillation Magnetic Detector) experiment was situated at CERN in Geneva, Switzerland. Proposed by Astier et al. 1991 [34], the construction was completed in 1995 and data was collected from 1995 to the end of 1998. NOMAD combined the benefits of counter experiments and bubble chambers, namely high statistics and high spatial resolution. The main goal of the NOMAD experiment was a short baseline search for $\nu_\mu \rightarrow \nu_\tau$ neutrino oscillations in the CERN SPS wide band neutrino beam. The ν_τ was searched for via its charged current reaction $\nu_\tau + N \rightarrow \tau^- + X$. For the energies considered, the charged τ leptons travel about 1 mm before decaying. Since the spatial resolution of NOMAD was not sufficient to resolve impact parameters associated with such decay tracks, the τ^- were identified using kinematic criteria, based on a precise measurement of the missing transverse momentum in the final state. Final results can be found in [35]. The large sample of recorded interactions has allowed for a wide range of measurements. In particular a search for $\nu_\mu \rightarrow \nu_e$ oscillation has been undertaken [36].

3.1 The Neutrino Beam

The geometry of the West Area Neutrino Facility (WANF) is shown in Figure 3.1. The Super Proton Synchrotron (SPS) at CERN supplied a beam of 450 GeV protons which was directed onto a beryllium target, thereby producing a large number of secondary hadrons. In every accelerator cycle (14.4 s) the protons used to produce neutrinos were extracted from the SPS in two spills, which were separated by 2.7 s. Each spill had a full width at half maximum of 3 ms and contained about 1.8×10^{13} protons. The number of protons incident on the target was monitored by a beam current transformer (BCT). The number of produced neutrinos was often expressed in units of protons on target (POT). The multiplicity and charge asymmetry of the secondary particles was measured by secondary emission monitors (SEMs) placed before and after the target. The beam focusing elements, downstream of the target, were large magnets, designed to collimate the positively charged secondary particles, while deflecting the negatively charged particles away from the beam axis. Most of the focusing was done by the first element, called the horn. The second

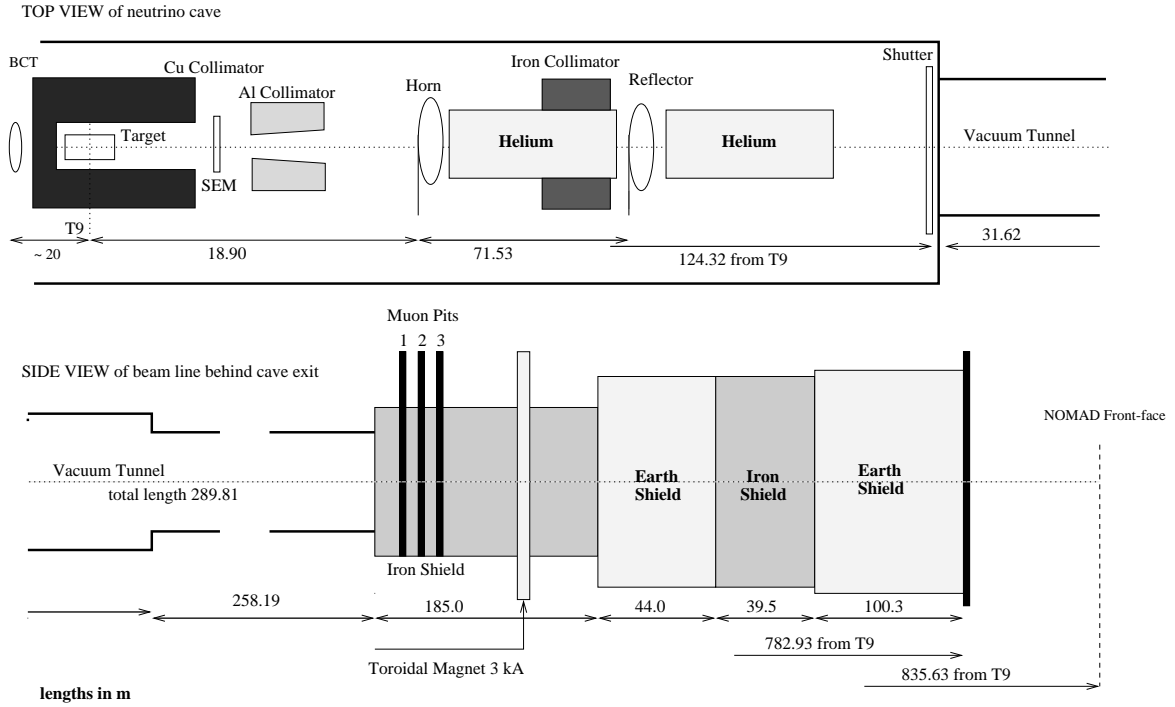
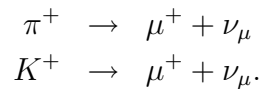


Figure 3.1: Schematic layout of the WANF beam line (all lengths in m).

element, the reflector, focused the smaller angle particles which had been missed by the horn. Two helium bags were installed in order to increase the neutrino flux by reducing multiple scattering and secondary interactions along the beam. Downstream of the focusing elements was a vacuum decay tunnel of 290 m length in which the positively charged particles could decay and, thereby, produce the neutrinos. The major contributions to the ν_μ flux came from the reactions:



The charge conjugate reactions also occurred, giving rise to a $\bar{\nu}_\mu$ component in the beam. Earth and iron shielding directly after the decay tunnel filtered out all but neutrinos and some muons. Silicon detectors in several pits within the shielding region measured the muon multiplicity and could be used to monitor the beam and determine the absolute flux. An additional toroidal magnet, which was placed after the muon pits, deflected most of the remaining muons. The resulting neutrino beam reached the NOMAD detector 835 m downstream of the proton target with the composition and properties shown in Figure 3.2 and Table 3.1 [37]. The predictions of the neutrino fluxes are based on Monte Carlo simulations. For further reference on the WANF layout and the alignment procedures, see [38].

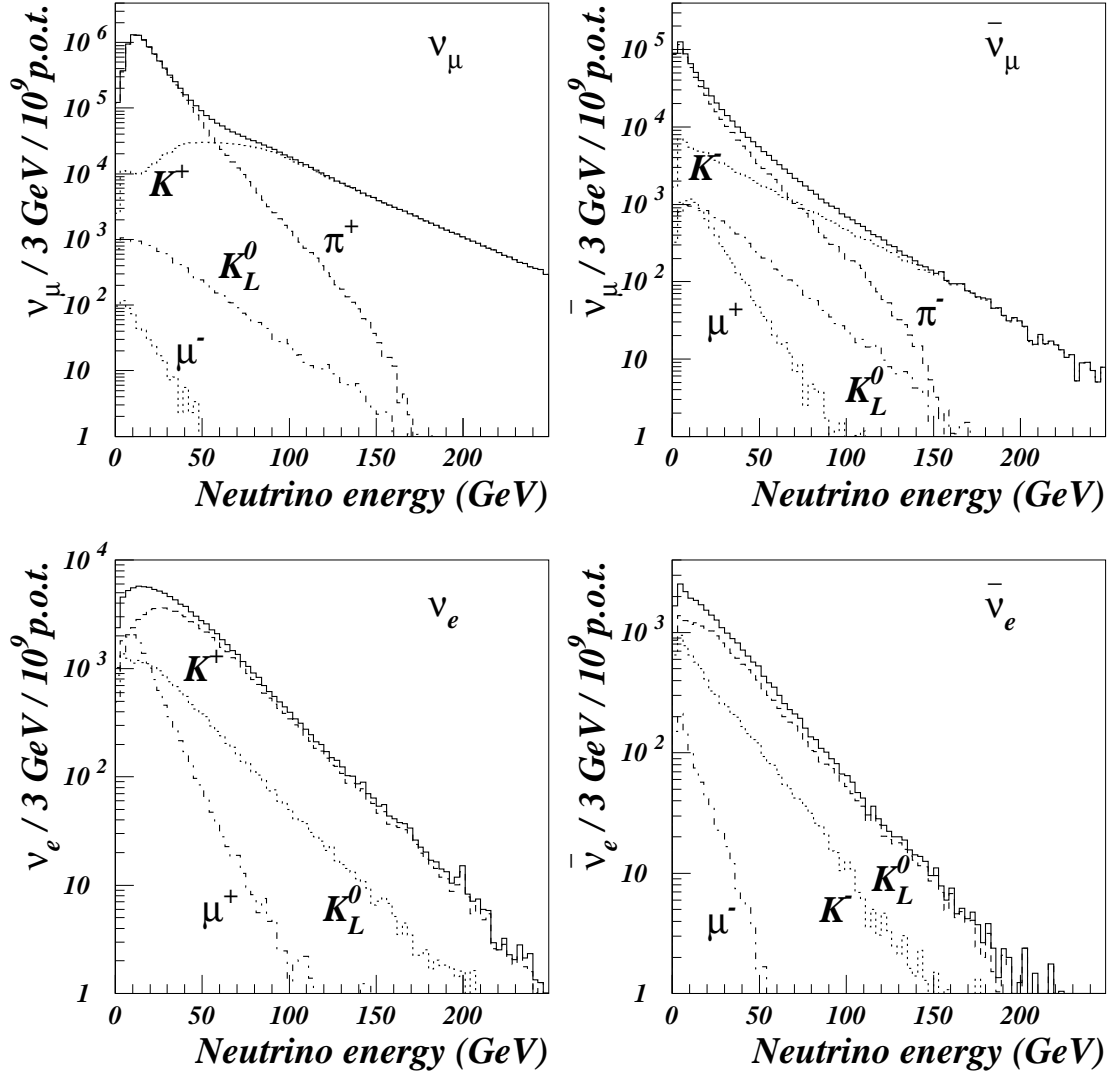


Figure 3.2: Composition of the neutrino beam and the ν_μ , $\bar{\nu}_\mu$, ν_e and $\bar{\nu}_e$ energy spectra at NOMAD, within the transverse fiducial area of $260 \times 260 \text{ cm}^2$. The Figures are taken from [37].

Neutrino Species	Neutrino Flux		Source							
			π^+ or π^-		K^+ or K^-		K_L^0		μ^+ or μ^-	
	Rel. Abund.	$\langle E_\nu \rangle$	%	$\langle E_\nu \rangle$	%	$\langle E_\nu \rangle$	%	$\langle E_\nu \rangle$	%	$\langle E_\nu \rangle$
ν_μ	1.0	24.3	90.4	19.1	9.5	73.0	0.1	26.8	< 0.1	11.4
$\bar{\nu}_\mu$	0.0678	17.2	84.0	13.8	12.8	38.1	1.9	26.9	1.2	17.0
ν_e	0.0102	36.4	—	—	68.0	41.8	17.8	30.3	13.6	16.8
$\bar{\nu}_e$	0.0027	27.6	—	—	25.1	22.8	68.2	30.4	3.5	11.1

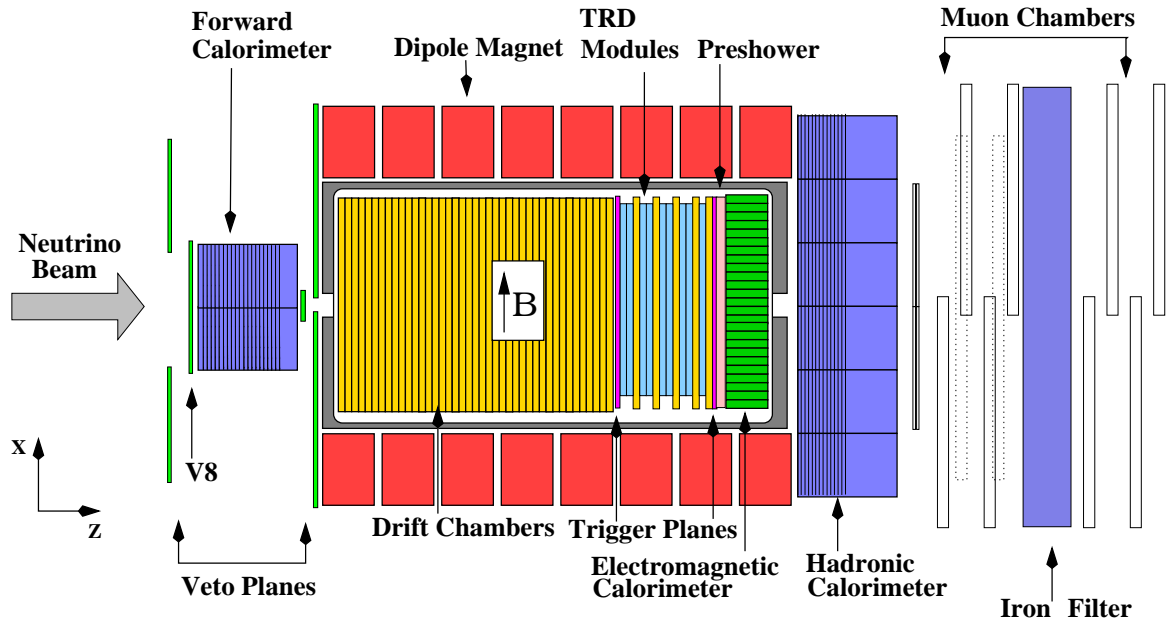
Table 3.1: Composition of the neutrino beam and the sources of the different components [37].

3.2 The Detector

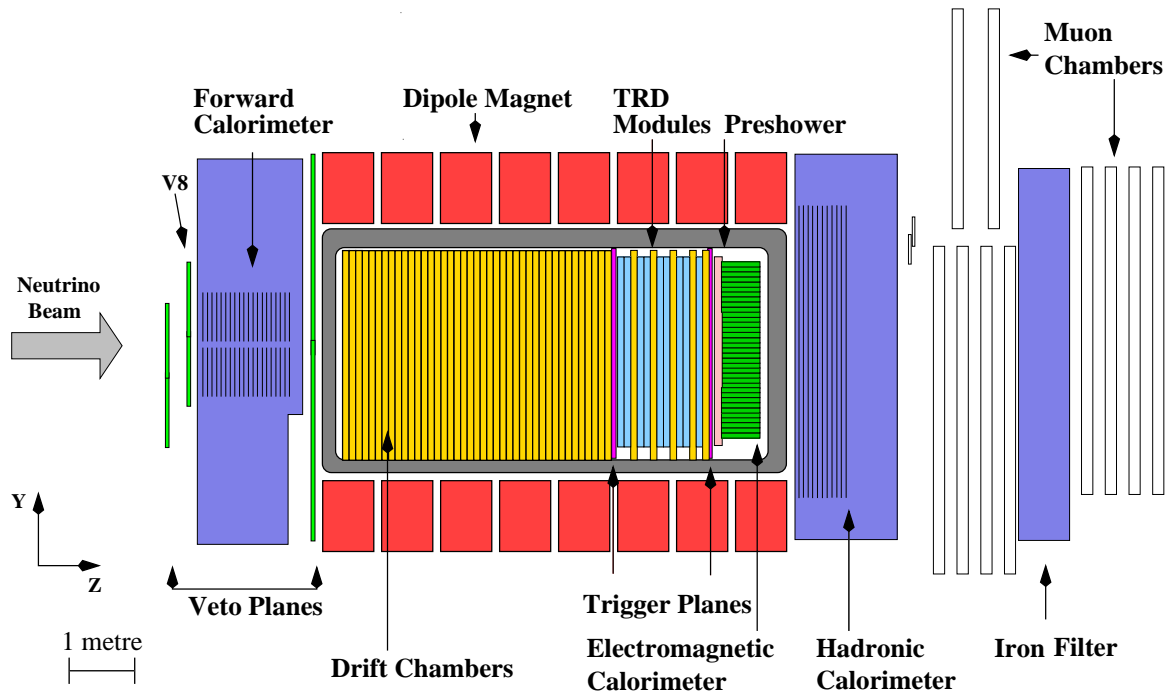
The NOMAD detector [39] was composed of several independently working sub-detectors. A schematic view of the detector is shown in Figure 3.3 along with the co-ordinate system. The sub-detectors were placed along the beam-line with positional sensitivity transverse to the beam direction. Most of the secondary particles which were produced in neutrino interactions traveled in the beam direction since the interaction momentum was mainly provided by the neutrinos. The *veto* system upstream of the detector allowed a fast identification of muons entering the detector. Following the muon veto, there was the *forward calorimeter* (FCAL) which was used as a target for studies requiring very high statistics while sacrificing some resolution in the vertex finding. The *drift chambers* (DCH) in the center of the detector served as an active target and hence the most interesting of the detected interactions occurred there. Further downstream, the *trigger planes*, the *transition radiation detector* (TRD), the *preshower* (PRS) and the *electromagnetic calorimeter* (ECAL) were situated. These inner detectors (DCH to ECAL) were all surrounded by a dipole magnet which provided a constant magnetic field. The *hadronic calorimeter* (HCAL) followed downstream of the inner detectors and at the very end there were the *muon chambers*. The x and y axes of the co-ordinate system were centered in the middle of the first drift chamber. The neutrino beam entered with an angle of 42 mrad to the z axis. It intercepted from below with the origin of the y axis in the ECAL.

3.2.1 The Magnet

The NOMAD detector reused the dipole magnet from the former UA1 experiment which is described in [40]. The magnet coil was made from aluminum and provided a near constant field of 0.4 Tesla which required a current of 5713 kA. The field, which was perpendicular to the z axis throughout the DCH and the TRD region, allowed an accurate momentum reconstruction for charged particles traversing the central detector. The two iron supports, which acted as yokes, had been instrumented as calorimeters. The front pillar was used to form the forward calorimeter, the back pillar formed the hadronic calorimeter.



(a) top view



(b) side view

Figure 3.3: Top and side view of the NOMAD detector.

3.2.2 The Veto Counters

Being the most upstream detector, the veto consisted of 59 scintillator counters and covered an area of $5.4 \times 5 \text{ m}^2$. It was used to detect muons traveling with the neutrino beam and charged particles from upstream interactions, and prevented them from causing valid triggers. An additional veto plane was positioned between the FCAL and the DCH. Charged particles from interactions downstream of the veto, e. g. in the magnet coil or the support structures of the drift chambers, were removed during analysis by constraints on the vertex position.

The scintillators were read out by photo-multipliers and a veto signal was constructed from a logical OR of all the individual counters. The efficiency of the veto was constantly monitored and found to be stable at about 96% – 97%. The contribution of the veto to the overall dead time of the experiment during the two neutrino spills amounted to about 4%. A detailed description of the veto system can be found in [41].

3.2.3 The Forward Calorimeter (FCAL)

The forward calorimeter, being the instrumented front pillar of the magnet, was used as a massive active target and allowed neutrino physics studies including di-muon production and neutral heavy lepton searches. The FCAL consisted of 23 iron plates, which were 4.9 cm thick and separated by 1.8 cm air gaps. The first 20 gaps were instrumented with scintillator counters. The dimensions of the scintillators were $175 \times 18.5 \times 0.6 \text{ cm}^3$. Five consecutive counters along the beam direction were bunched together via light guides to form a module which was read out at both ends by photo-multipliers (see Figure 3.4). Ten such modules were arranged vertically to form a stack. There were four stacks aligned along the beam axis. The active region of the FCAL had a mass of 17t, was about 5 nuclear interaction lengths in depth and had an active area transverse to the beam of $175 \times 190 \text{ cm}^2$. Further details can be found in [39].

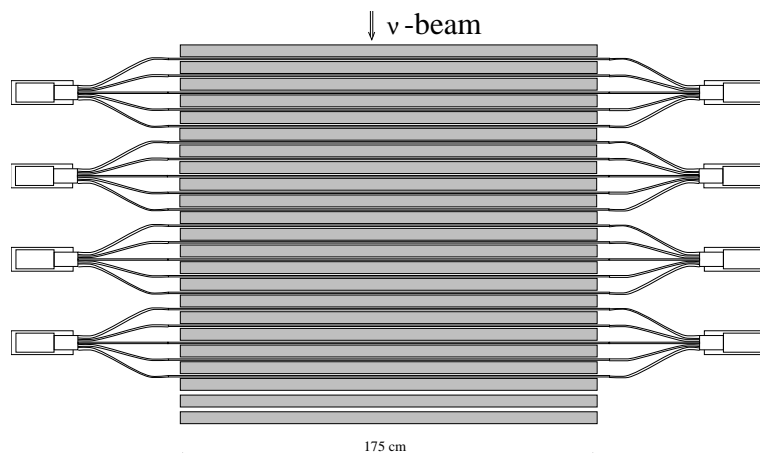


Figure 3.4: Top view of the FCAL.

3.2.4 The Drift Chambers (DCH)

A crucial part of the detector were the drift chambers which provided at the same time the target material and the track and vertex reconstruction of the charged particles. This double function implied conflicting requirements for the walls of the drift chambers, for they had to be as massive as possible to guarantee a large number of neutrino interactions and as light as possible to minimize multiple scattering of particles, secondary particle interactions and photon conversions. In order to reduce the radiation length for a given target mass, the chambers were made of low density and low atomic number materials which resulted in less than 1% of a radiation length in the inactive area between two consecutive measurements. The full drift chamber region consisted of 11 modules, each made up of four individual drift chambers. In addition to these 44 drift chambers, there were another 5 chambers in the TRD region, providing additional tracking. The chambers were built on panels made of aramid fibers in a honeycomb structure and sandwiched between two kevlar-epoxy resin skins. These skins ensured the mechanical rigidity and flatness over the area of $3 \times 3 \text{ m}^2$. Each drift chamber comprised four panels with three gaps of 8 mm in between. The gaps were filled with a mixture of argon (40%) and ethane (60%), and equipped with sense wires. Since the chambers were not completely gas tight, the gas was circulated permanently in a closed circuit with a purifier section that removed oxygen and water vapor. The volume with maximal acceptance and reconstruction efficiencies was referred to as fiducial volume and had the dimensions of $2.6 \times 2.6 \times 4 \text{ m}^3$ with a mass of 2700 kg. The overall density of 100 kg/m^3 was about equal to the density of liquid helium. Table 3.2 shows the atomic composition of the fiducial volume in detail. The sense wires

Atom	Proportion of Weight (%)	Atomic Weight
carbon	64.3	12.011
oxygen	22.13	15.999
nitrogen	5.92	14.007
hydrogen	5.14	1.008
aluminum	1.71	26.982
chlorine	0.31	35.453
silicon	0.27	28.086
argon	0.19	39.948
copper	0.03	63.546
Total	100.00	
protons	52.43	
neutrons	47.57	

Table 3.2: Composition of the drift chamber fiducial volume [42].

in the three gaps of a drift chamber were oriented with -5, 0 and +5 degrees with respect to the magnetic field direction, corresponding to the NOMAD x axis. The three ionization

signals produced by a particle traversing a drift chamber allowed a hit positioning accurate to about 1.5 mm in the x direction, due to the angles between the wires. Transverse to the wires (y direction) a position accuracy of $150 \mu\text{m}$ was reached by the separation of the wires and a constant gas drift velocity. The position along the beam line (z direction) was determined by the position of the wire planes which was constantly monitored. The efficiency of each wire to record a hit was typically 97%. The three dimensional information from each drift chamber could be used to reconstruct the helical path of charged particles through the magnetic field. The curvature allowed the measurement of the momentum of the particles through the relation

$$p \cos \theta_\lambda = qBr \quad (3.1)$$

where p is the momentum and q the charge of the particle, θ_λ the pitch angle of the helix, r the radius of curvature and B the magnetic field. The momentum resolution was a function of the particle momentum and track length. For muons and charged hadrons with normal incidence to the measuring planes the momentum resolution could be parametrized by

$$\left(\frac{\sigma_p}{p}\right)^2 = \left(\frac{a}{\sqrt{L}}\right)^2 + \left(\frac{bp}{\sqrt{L^5}}\right)^2 \quad (3.2)$$

with

$$\begin{aligned} a &= 0.05 \text{ m}^{1/2} \\ b &= 0.008 \text{ m}^{5/2} (\text{GeV}/c)^{-1} \end{aligned} \quad (3.3)$$

and L denoting the length of the track. The first term in (3.2) corresponds to the error due to multiple-scattering, the second term arises from the single hit resolution. A detailed description of the drift chamber is given in [43].

3.2.5 The Transition Radiation Detector (TRD)

The purpose of the transition radiation detector was to separate electrons from pions. A pion rejection factor larger than 10^3 was reached for an electron identification of 90% in the momentum range from 1 to 50 GeV/c. Together with the additional rejection provided by the preshower and the electromagnetic calorimeter, a pion rejection factor greater than 10^5 was achieved. This was necessary for the oscillation search in the favored channel, $\tau^- \rightarrow e^- + \bar{\nu}_e + \nu_\tau$, in order to eliminate neutral current background events with an isolated pion mimicking an electron.

Transition radiation is produced by charged particles crossing the boundaries between media which have different electron densities [44, 45]. The number of photons produced is proportional to the Lorentz factor $\gamma = E/m$. Particles with higher mass, having a Lorentz factor $\gamma < 500$, deposited their energy mainly due to ionization loss, whereas electrons in NOMAD typically had a Lorentz factor $\gamma > 500$ and thus produced also transition radiation. Since the number of photons produced per transition is small, a large number of layers had to be used. The TRD, shown in Figure 3.5, consisted of 9 identical modules which included a radiator and a detection plane. The radiator comprised 315

polypropylene foils separated by $250\ \mu\text{m}$ air gaps. Each foil was $15\ \mu\text{m}$ thick and had an area of $2.85 \times 2.85\ \text{m}^2$. The detection plane was made up of 176 proportional tubes. The horizontal position of these tubes provided additional information about the position of tracks and was used to extrapolate the tracks from the drift chambers. More details about the TRD can be found in [46].

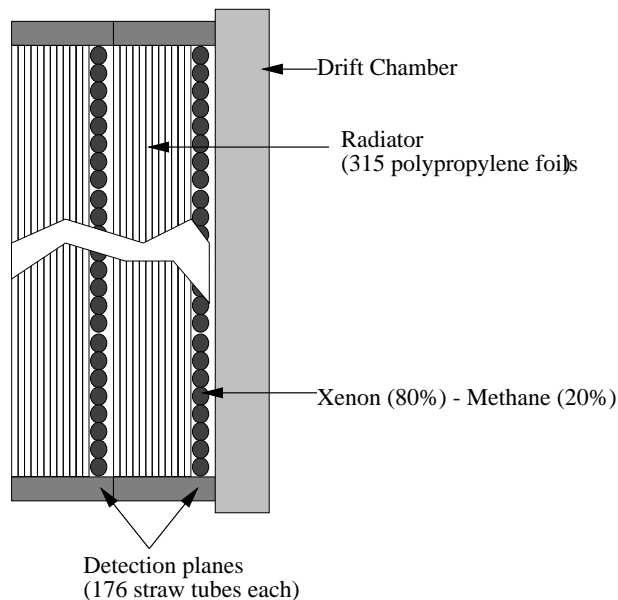


Figure 3.5: Top view of the TRD setup.

3.2.6 The Preshower Detector (PRS)

The preshower detector in NOMAD was placed directly in front of the electromagnetic calorimeter. It was composed of two 9 mm thick lead-antimony sheets, separated by a 2 mm thick aluminum plate and followed by two planes of proportional tubes, 286 horizontal and 288 vertical. An exploded view of the PRS is given in Figure 3.6. The higher energy deposit of electrons traversing the PRS compared to the energy deposited by hadrons allowed a distinction between the two particle types. Together with the TRD and the electromagnetic calorimeter, the PRS might be used for improving the pion rejection. The position information provided by the proportional tubes yielded a measurement of the interaction point of photons and helped in the resolution of overlapping energy clusters in the electromagnetic calorimeter.

3.2.7 The Electromagnetic Calorimeter (ECAL)

The electromagnetic calorimeter consisted of lead glass counters having a depth of 19 radiation lengths and a rectangular cross section of $79 \times 112\ \text{mm}$. The 875 counters were

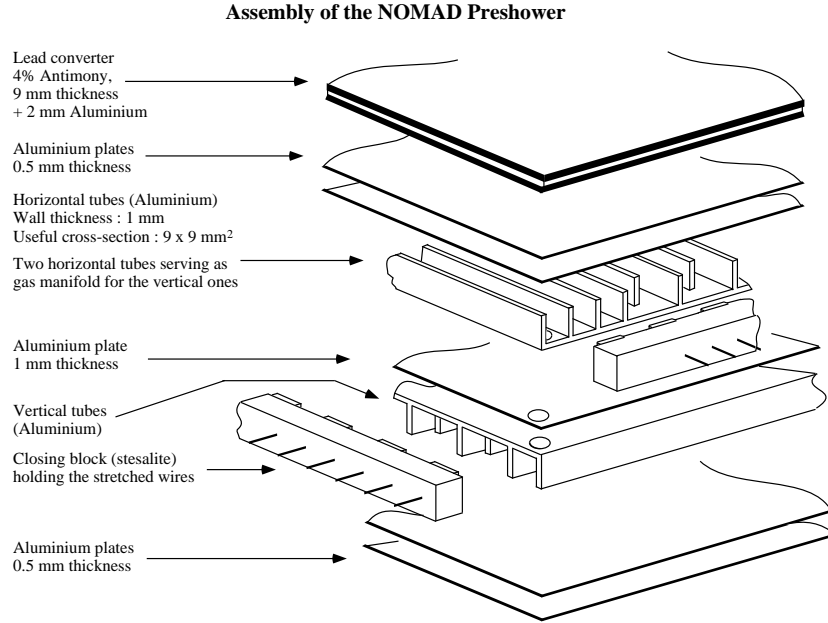


Figure 3.6: An exploded view of the preshower detector.

installed in a matrix of 35 rows and 25 columns. The ECAL was capable of measuring the energy of incident photons and electrons in a range from 100 MeV to 100 GeV with an energy resolution fitted with two parameters:

$$\frac{\sigma_E}{E} = a + \frac{b}{\sqrt{E}} \quad (3.4)$$

and

$$\begin{aligned} a &= (1.04 \pm 0.01) \times 10^{-2} \\ b &= (3.22 \pm 0.07) \times 10^{-2} \text{ GeV}^{1/2}. \end{aligned}$$

Using the PRS in conjunction with the ECAL, the discrimination of electrons and pions was improved substantially. The presence of the lead plates of the PRS degraded the energy resolution of the ECAL. However, by combining the ECAL with the proportional tubes of the PRS, the energy resolution could be partially recovered.

3.2.8 The Hadronic Calorimeter (HCAL)

The instrumented back pillar of the magnet served as the hadronic calorimeter in NOMAD. Being an iron-scintillator sampling calorimeter, it consisted of 11 scintillator planes, placed in the 1.8 cm gaps between the first 12 of the 23 iron plates which formed the support pillar. Each scintillator plane was made up of 18 horizontal paddles resulting in an area of $3.6 \times 3.5 \text{ m}^2$ transverse to the beam direction. Photo-tubes on both sides measured

the scintillation light which was directed through adiabatic light guides. In Figure 3.7 a schematic view of the HCAL is given. The HCAL served the purpose of measuring the

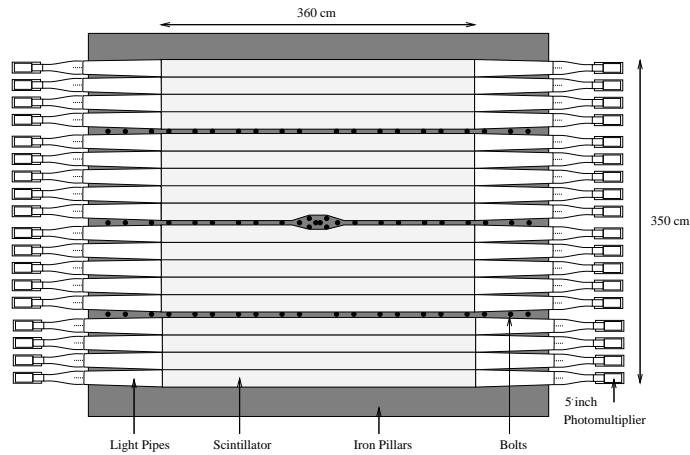


Figure 3.7: The front view of the HCAL.

energy and position of neutral hadrons. This was important in order to reconstruct kinematic quantities such as the missing transverse momentum. Additionally, the calorimetric measurement of charged particles could be used as a consistency check on the momentum measurement and as an aid in distinguishing between muons and charged hadrons. The horizontal signal position was determined from the ratio of signals at both ends of a scintillator paddle, giving a resolution of approximately 20 cm. The energy deposited in a scintillator module was obtained from the geometric mean of the two photo-tube signals. For further details see [39].

3.2.9 The Muon Chambers

The muon chambers comprehended 10 drift chambers as shown in Figure 3.8, each with an active area of $3.75 \times 5.55 \text{ m}^2$. The chambers were made of 48 vertical and 78 horizontal drift cells which provided the position of charged particles passing through, with a resolution of about $430 \mu\text{m}$ for tracks crossing at 0° with respect to the neutrino beam direction. The chambers were placed behind the HCAL and grouped into two stations which were separated by a 80 cm thick iron wall which acted as a hadron absorber additional to the HCAL. A muon passing through a station often gave rise to hits in at least two drift chambers thus providing positional and directional information. The average hit efficiency of the muon chambers was 92.5% with a dominant source of inefficiency being due to dead areas. A small gap between the muon chambers in the first station was closed in 1996 by the addition of scintillators.

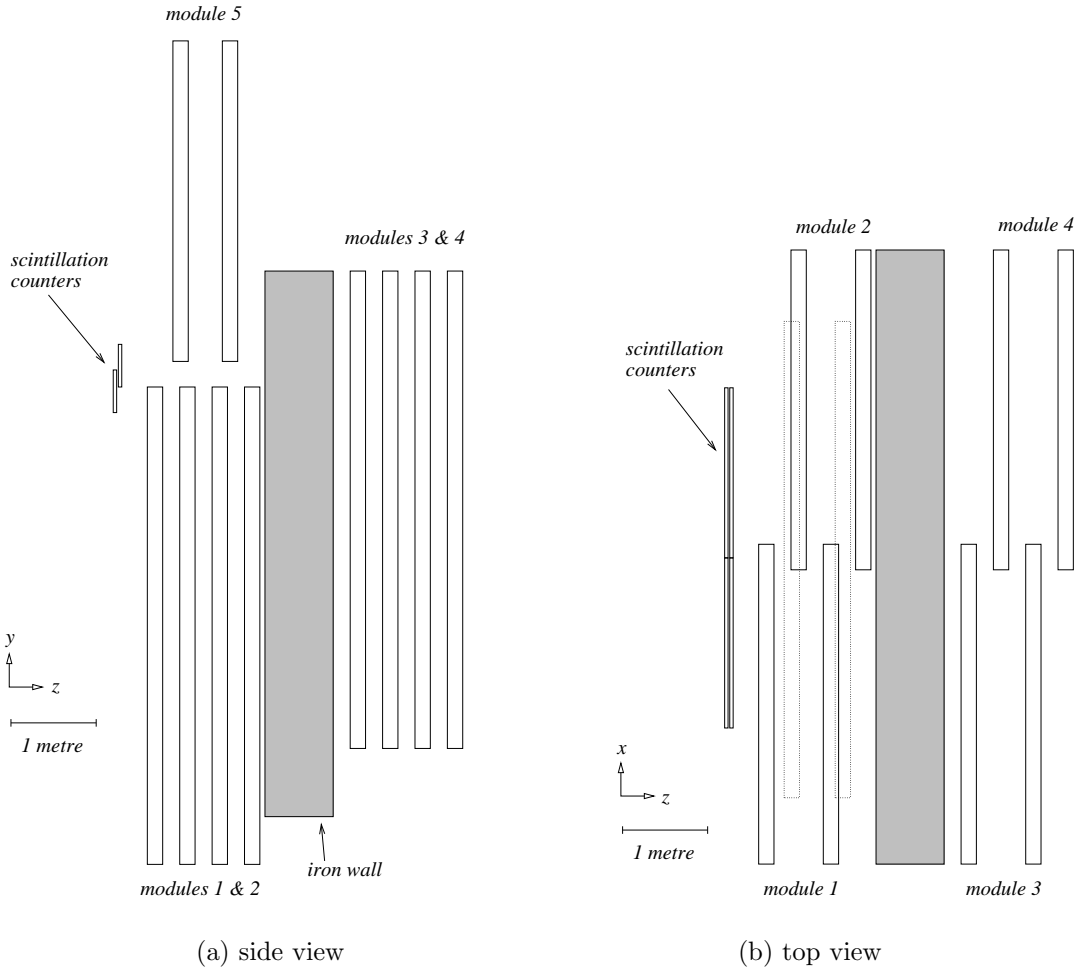


Figure 3.8: Layout of the muon chambers.

3.2.10 The Trigger System

Within the NOMAD magnet two planes of scintillator counters were placed downstream of the drift chambers (see Figure 3.3). These trigger planes, T_1 and T_2 , detected charged particles from neutrino interactions. Coincident signals from both trigger planes, together with the absence of a signal from the veto plane, defined the primary trigger for NOMAD, known as the $\bar{\nu}T_1T_2$ trigger. Events fulfilling this trigger condition corresponded mainly to neutrino interactions in the drift chambers. The time needed to acquire data from each sub-detector and the time interval of the veto signal caused a dead time for the experiment which was found to be approximately 17%. Using the information of the FCAL and ECAL, additional triggers could be defined for events occurring in the FCAL or ECAL, as well as for events recorded for calibration purposes. A detailed description of the trigger system and these additional triggers is given in [39].

Chapter 4

Monte Carlo Simulation

Today's experimental particle physics relies heavily on the simulation of physics processes. Such simulations are often needed to estimate efficiencies of event selection algorithms or to study the effects of detector acceptances on event distributions. Monte Carlo techniques are used to generate events randomly, according to a set of given physics criteria. The task of creating event samples, which describe the main physics processes, is done by so called Monte Carlo generators. The expected detector response to these generated events is then produced by detector simulations whose output is of the same form as data¹, with the substantial difference that the details of the underlying processes are known.

4.1 Charged Current Monte Carlo Sample

The NOMAD software environment includes a Monte Carlo simulation predicting the neutrino beam, an event generator describing neutrino-nucleon scattering, a detector simulation and a reconstruction package which transforms the raw output of the detector for data and Monte Carlo events into a form suitable for analysis.

4.1.1 The Neutrino Beam Simulation

A program entitled NUBEAM is used to simulate the neutrino flux in the NOMAD detector. It starts with the production of particles in the beryllium target by the incident proton beam. The distribution of emerging particles is obtained from the year 2000 version of the FLUKA software package [47]. The propagation of the secondary particles along the beam line is taken care of by a simulation package based on GEANT3 [48] which models the re-interactions behind the beryllium target and includes an accurate description of the magnetic fields in the horn and the reflector. The resulting energy spectra of the decay neutrinos are shown in Figure 3.2.

¹In this thesis the expression “data” is only used in connection with real events.

4.1.2 The Event Generation

The neutrino flux generated by NUBEAM is taken as input² for the generation of neutrino-nucleon scattering events in the NOMAD drift chambers. The Monte Carlo generator includes DIS, quasi elastic (QEL) and resonant (RES) processes. The DIS events are simulated with a modified version of the LEPTO 6.1 generator [49] where the Q^2 and W^2 cutoffs have been removed. The QEL and RES events are generated according to the formulas found in [30] and [50]. For the parton density functions, which describe the quark content of the nucleon, the GRV-HO parametrization [51] has been chosen. The Fermi motion of the nucleon is described according to [52] and truncated at 1 GeV/c. The fragmentation of the final state, which forms the hadrons out of the partons, as well as the strong and electromagnetic decays are performed by JETSET 7.4 [53].

The DIS Monte Carlo generates events with a W^2 above $1.8 \text{ GeV}^2/c^4$, the RES and the QEL Monte Carlo generate the events below. The RES Monte Carlo has been weighted such that the sum of RES and DIS events has a continuous W^2 distribution. The contribution of the QEL Monte Carlo events is determined by the well known cross section. For charged current interactions of muon neutrinos, this ends up in

$$\frac{N_{\text{QEL}}}{N_{\text{cc}}} = 2.3\% \quad (4.1)$$

$$\frac{N_{\text{RESO}}}{N_{\text{cc}}} = 3.8\%. \quad (4.2)$$

4.1.3 The Detector Simulation and Event Reconstruction

The detector simulation of NOMAD, called GENOM, is based on GEANT3 [48]. It simulates the propagation and interactions of the particles produced in the primary neutrino-nucleon scattering process within the detector. Also, the decays of particles living long enough to produce secondary vertices³, that can be distinguished from the primary vertex, are carried out by GENOM. Finally, it simulates the full detector response to the event and produces an output similar to the data. The reconstruction of Monte Carlo and data events is done in two stages by a program called RECON. First, hits, tracks, vertices and energy deposits in the individual sub-detectors are reconstructed, then, in the second stage, the individual particles are identified by matching the tracks in the drift chambers with the tracks and clusters in the other sub-detectors. The output of the reconstruction is stored in a DST (Data Summary Tape), the format which is used for the analyses.

4.1.4 Comparison with Data

After reconstruction, the Monte Carlo results can be compared with data. In order to receive a set of data events that consists mainly of charged current muon neutrino ($\nu_{\mu}\text{cc}$)

²The neutrino energy and the position of the interaction are given as input for the Monte Carlo event generator.

³Here, a vertex refers to the reconstructed position of an interaction.

events, the following selection criteria have to be fulfilled:

- **Detector:** Proper performance of detector and beam is demanded during the data taking period (*run*). Events from previously identified “bad” runs are rejected.
- **Trigger:** The events must fulfill the $\overline{V}T_1T_2$ trigger described in section 3.2.10.
- **Primary muon:** At least one identified muon with an energy $E_\mu > 5$ GeV has to be present at the primary vertex. A muon candidate is a drift chamber track that has been matched with a track reconstructed in the muon chambers. The primary muon, which is assumed to have the highest transversal momentum with respect to the neutrino beam direction, must be negatively charged.
- **Fiducial volume:** The primary vertex has to be in a confined region within the drift chambers. In the NOMAD co-ordinate system this region is given by:

$$\begin{aligned} -120 \text{ cm} &\leq x_{V^1} \leq 120 \text{ cm} \\ -120 \text{ cm} &\leq y_{V^1} \leq 120 \text{ cm} \\ 60 \text{ cm} &\leq z_{V^1} \leq 395 \text{ cm} \end{aligned} \quad (4.3)$$

- **Track multiplicity:** Including the μ^- , at least two reconstructed primary tracks must be found. Here, a track is assumed to originate from the primary vertex if its first hit has been found in a cylinder (*radius* = 30 cm, *length* = 40 cm) with axis along the neutrino beam direction and starting 10 cm in front of the primary vertex. The number of primary tracks is denoted⁴ by $n_{trksV^1}^{box}$.
- **Charge:** The charge sum of the primary track candidates has to fulfill

$$-1 \leq \sum_{box} Q_{trks} \leq 2. \quad (4.4)$$

Figures 4.1 - 4.4 show the comparison of the charged current Monte Carlo events with the data after applying the cuts described. The Monte Carlo sample which comprises about 3.8 times the number of events of the data sample, was normalized to the latter after the cuts. The error bars shown are statistically only and have been omitted for the Monte Carlo simulation.

Figure 4.1(a) shows the reconstructed neutrino energy which is given by

$$E_\nu^{vis} = |\mathbf{p}_\mu + \sum \mathbf{p}_c + \sum \mathbf{p}_n|, \quad (4.5)$$

because of momentum conservation. The momenta of the charged and neutral particles, \mathbf{p}_c and \mathbf{p}_n , have been determined during reconstruction by a kinematic fit of the measurements of the DCH and the ECAL. The agreement between data and Monte Carlo simulation is fairly good. Also, the distribution of the muon energy shown in Figure 4.1(b) is well described by the Monte Carlo simulation.

⁴A short description of the variables used in the analysis is given in appendix A

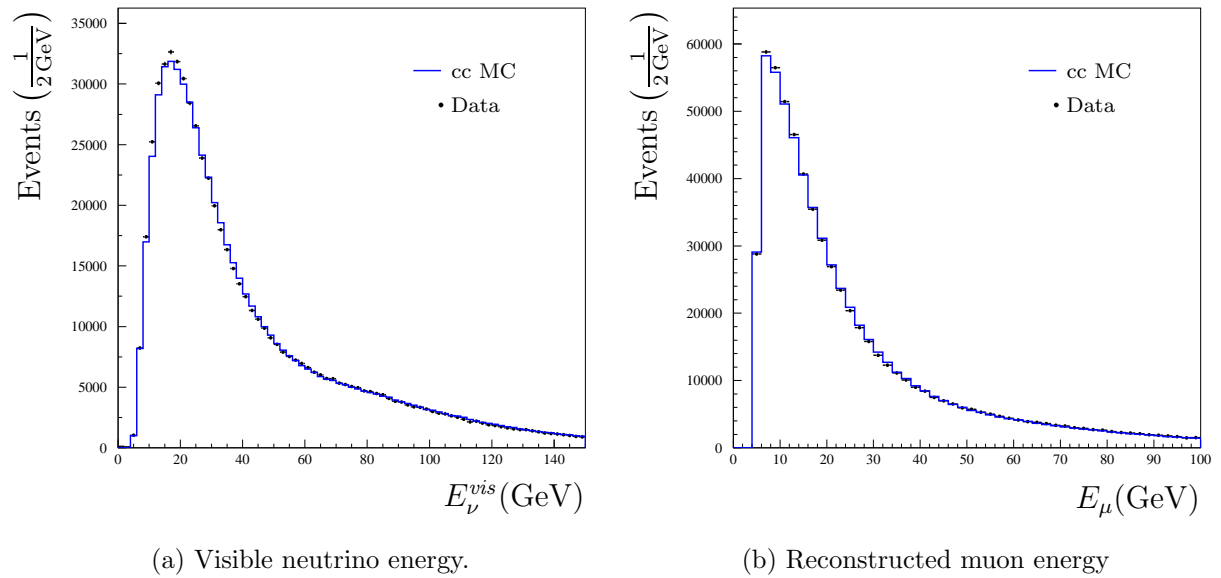
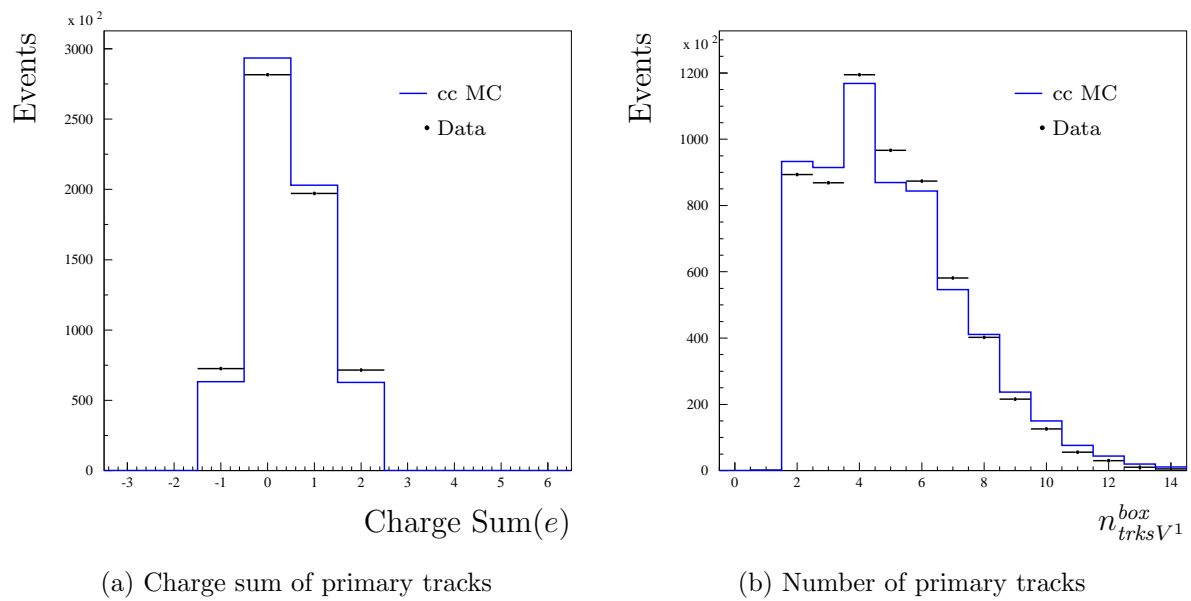
Figure 4.1: Reconstructed energies in $\nu_\mu cc$ events.

Figure 4.2: Charge and tracks multiplicities.

Figure 4.2(a) shows the distribution of the charge sum for data and Monte Carlo events. The distribution is peaked for the values zero and one, as it is expected from charge conservation for neutron and proton target nucleons. In events with total charge > 1 or < 0 some charged tracks have not been reconstructed or their charge has been misassigned. The charge distribution of the Monte Carlo events is slightly narrower than for real events. The tails have been removed by the ν_μ cc event selection cuts. In Figure 4.2(b) the number of primary tracks n_{trksV1}^{box} per event is plotted. Again, a good but not perfect agreement between data and the Monte Carlo simulation is found. The first two bins are empty due to the ν_μ cc selection criteria.

Figure 4.3 shows the distribution of the position of the primary vertex along the x , y and z axis of the NOMAD co-ordinate system. The comparison shows how well the geometry and the materials are implemented into the detector simulation. The vertex position distribution is well described by the Monte Carlo simulation. The peaks in the x and y plots arise from the support structures which have a higher density than the drift chambers. The small discrepancies in the z distribution have generally no effect on a physics analysis.

Figure 4.4 shows the distributions of the reconstructed kinematic variables Q_{vis}^2 , W_{vis}^2 , x_{vis} and y_{vis} which have been calculated from the reconstructed neutrino energy and the muon momentum. In order to simplify the kinematic calculations, a more suitable co-ordinate system, called the neutrino frame, has been introduced. This co-ordinate system is rotated around the x axis by 42 mrad with respect to the NOMAD co-ordinate system and, thus, has its z axis aligned with the neutrino beam direction. In the neutrino frame the kinematic variables become

$$Q_{vis}^2 = 2E_\nu^{vis}(E_\mu - p_\mu^z), \quad (4.6)$$

$$W_{vis}^2 = m_N^2 - Q_{vis}^2 + 2m_N(E_\nu^{vis} - E_\mu), \quad (4.7)$$

$$x_{vis} = \frac{Q_{vis}^2}{2m_N(E_\nu^{vis} - E_\mu)} \quad (4.8)$$

and

$$y_{vis} = \frac{E_\nu^{vis} - E_\mu}{E_\nu^{vis}}. \quad (4.9)$$

The Q_{vis}^2 distribution in Figure 4.4(a) is well described by the Monte Carlo simulation. The compliance for W_{vis}^2 in Figure 4.4(b) is not as good. The Monte Carlo distribution has a slightly steeper decline. The distributions of the Bjorken variable x_{vis} and the inelasticity y_{vis} in figures 4.4(c) and 4.4(d) are only reproduced qualitatively.

4.2 Signal Monte Carlo Sample: Quasi Elastic Charm Production

In order to study QEC events in the NOMAD Experiment, Monte Carlo generators for the model of Shrock and Lee [6, 7] and for the model of Kovalenko [12] have been written. As

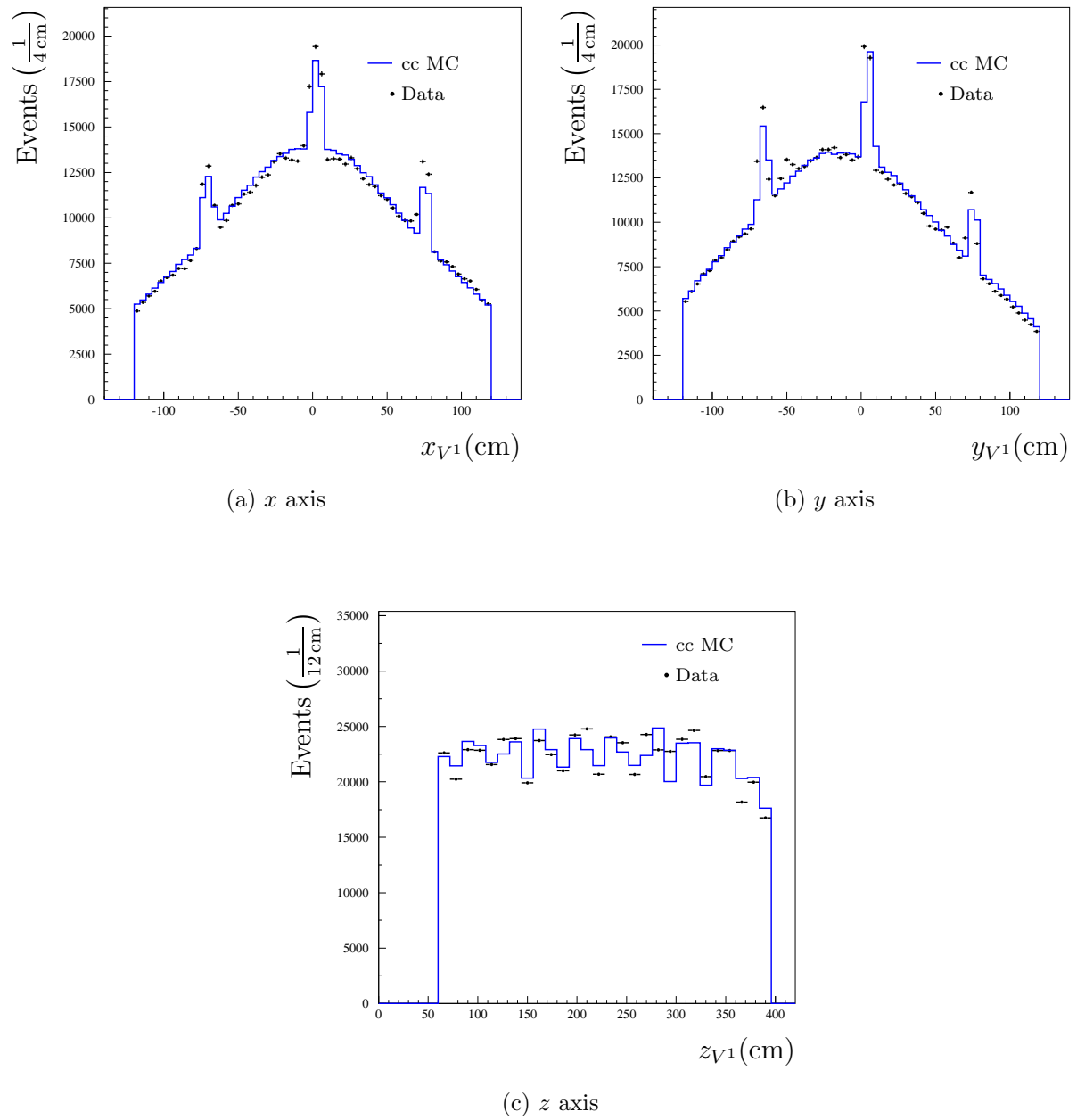
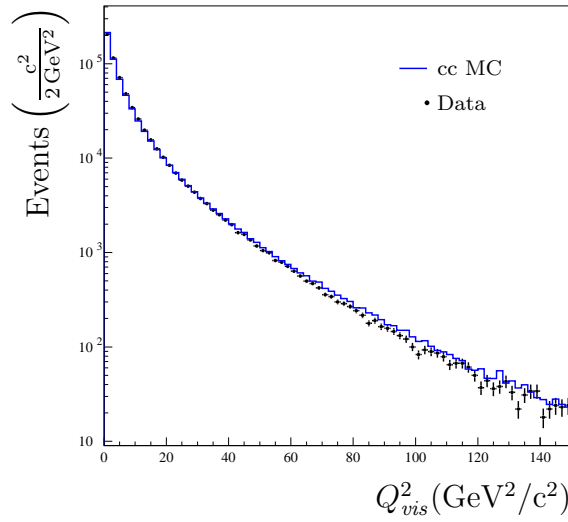
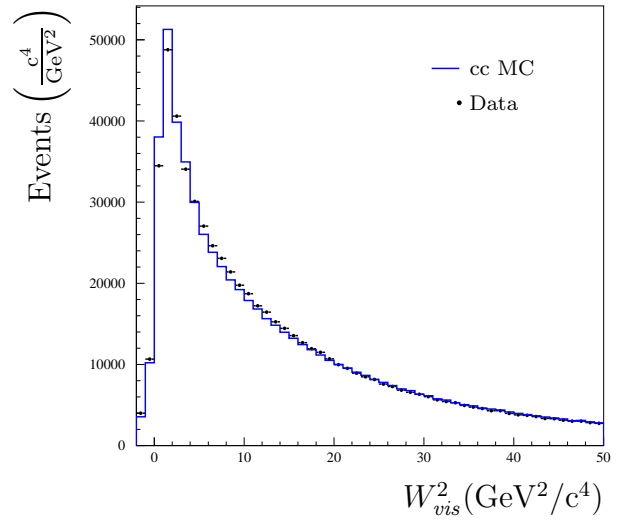


Figure 4.3: Position of the reconstructed primary vertex for data and Monte Carlo events.



(a) Square of the 4-momentum transfer



(b) Invariant mass of the hadronic system

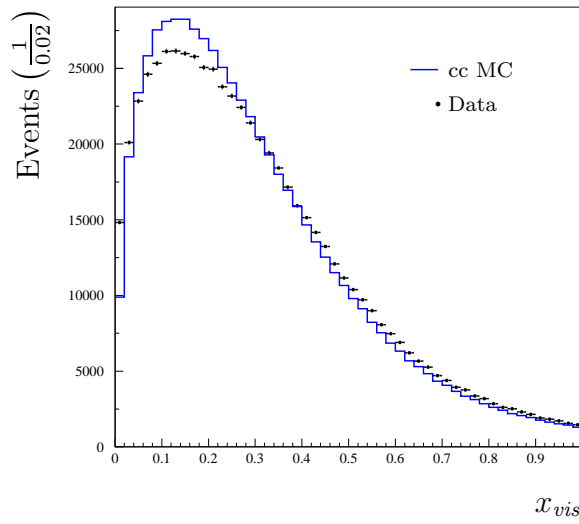
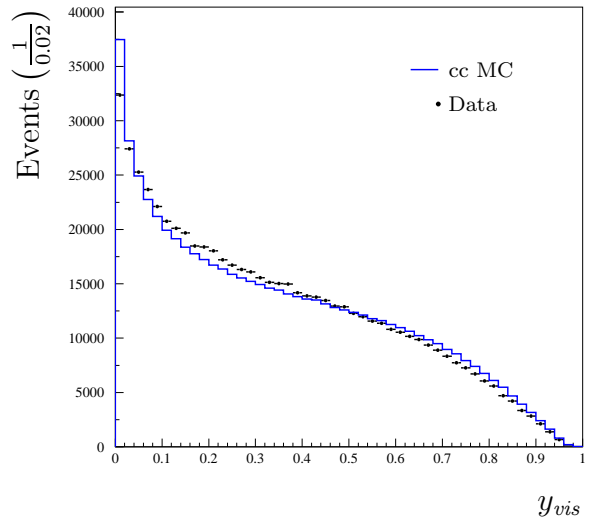
(c) Bjorken variable x_{Bj} (d) Inelasticity y

Figure 4.4: Reconstructed kinematic quantities for data and Monte Carlo events.

noticed in Section 2.3.3, QEC includes the processes (2.48)-(2.52). For this work, however, only the production of the ground state baryons,

$$\nu_\mu + n \rightarrow \mu^- + \Lambda_c^+ (2285) \quad (4.10)$$

$$\nu_\mu + n \rightarrow \mu^- + \Sigma_c^+ (2455) \quad (4.11)$$

and

$$\nu_\mu + p \rightarrow \mu^- + \Sigma_c^{++} (2455) \quad (4.12)$$

has been implemented. In the following some details about the cross section calculations for both models are given along with the values of the parameters used in the MC generators.

4.2.1 The QEC Model of Shrock and Lee

Assuming isospin symmetry for proton and neutron, the differential cross sections of the processes 4.11 and 4.12 are connected via the relation⁵:

$$\frac{d\sigma}{dQ^2}(\nu p \rightarrow \mu^- \Sigma_c^{++}) = 2 \frac{d\sigma}{dQ^2}(\nu n \rightarrow \mu^- \Sigma_c^+). \quad (4.13)$$

The cross sections are calculated, using the general formula

$$\frac{d\sigma}{dQ^2} = \frac{G_F^2 \sin^2 \Theta_C}{8\pi E^2} \left[-2q^2 W_1 + (4EE' + q^2)W_2 + \frac{E + E'}{m_N} q^2 W_3 \right] \quad (4.14)$$

with structure functions

$$W_1 = \frac{1}{4m_N^2} \{ [(m_{B_c} - m_N)^2 - q^2](g_V + f_V)^2 + [(m_{B_c} + m_N)^2 - q^2]g_A^2 \}, \quad (4.15)$$

$$W_2 = g_V^2 - \frac{q^2}{(m_N + m_{B_c})^2} f_V^2 + g_A^2 \quad (4.16)$$

and

$$W_3 = 2g_A(g_V + f_V). \quad (4.17)$$

The real form factors g_V , f_V and g_A can be calculated using the approximate $SU(4)$ symmetry (see Section 2.3.3). This results in

$$g_V = (3/2)^{1/2} F_1^p(Q^2) \quad (4.18)$$

$$f_V = (3/2)^{1/2} F_2^p(Q^2) \quad (4.19)$$

$$g_A = - (3/2)^{1/2} (1/3D + F)F_A(Q^2) \quad (4.20)$$

for $\nu_\mu n \rightarrow \mu^- \Lambda_c^+$ and

$$g_V = (3/2)^{1/2} (F_1^p(Q^2) + 2F_1^n(Q^2)) \quad (4.21)$$

⁵The variables are denoted as in Section 2.3.

$$f_V = (3/2)^{1/2} (F_2^p(Q^2) + 2F_2^n(Q^2)) \quad (4.22)$$

$$g_A = -(3/2)^{1/2} (F - D)F_A(Q^2) \quad (4.23)$$

for $\nu_\mu p \rightarrow \mu^- \Sigma_c^{++}$. The constants F and D can be determined via the measurement of baryon decays [54], e. g.

- $n \rightarrow pe^- \bar{\nu}_e$:

$$(F + D) = 1.2670 \pm 0.0035$$

- $\Sigma^- \rightarrow ne^- \bar{\nu}_e$:

$$(F - D) = -0.340 \pm 0.017$$

which yields

$$D = 0.8035 \pm 0.0087 \quad (4.24)$$

$$F = 0.4635 \pm 0.0087. \quad (4.25)$$

The Q^2 depending functions $F_1^{p,n}$ and $F_2^{p,n}$ are a weak generalization of the form factors appearing in the well known *Rosenbluth* formula for electron-nucleon scattering and can be expressed as

$$F_1^{p,n}(Q^2) = \frac{G_E^{p,n}(Q^2) + [Q^2/(m_N + m_{B_c})^2] G_M^{p,n}(Q^2)}{1 + Q^2/(m_N + m_{B_c})^2} \quad (4.26)$$

and

$$F_2^{p,n}(Q^2) = \frac{G_M^{p,n}(Q^2) - G_E^{p,n}(Q^2)}{1 + Q^2/(m_N + m_{B_c})^2} \quad (4.27)$$

with the dipole form factors

$$G_E^p(Q^2) = \frac{1}{(1 + Q^2/m_{D^*}^2)^2} \quad (4.28)$$

$$G_E^n(Q^2) \simeq 0 \quad (4.29)$$

$$G_M^p(Q^2) = \frac{1 + \mu_p}{(1 + Q^2/m_{D^*}^2)^2} \quad (4.30)$$

$$G_M^n(Q^2) = \frac{\mu_n}{(1 + Q^2/m_{D^*}^2)^2}. \quad (4.31)$$

The parameter m_{D^*} corresponds to the mass of the charmed vector meson

$$m_{D^*} = m_{D^*(2010)^+} = 2.01 \text{ GeV}/c^2 \quad (4.32)$$

and μ_n and μ_p refer to the anomalous magnetic moment of the neutron and the proton:

$$\mu_p = 1.7928473 \quad (4.33)$$

$$\mu_n = -1.913043. \quad (4.34)$$

The function F_A appearing in the axial-vector form factor g_A is also parametrized as a dipole:

$$F_A(Q^2) = \frac{1}{(1 + Q^2/m_A^2)^2} \quad (4.35)$$

with m_A standing for the mass of the charmed axial-vector meson:

$$m_A = m_{D_1(2420)^+} = 2.42 \text{ GeV}/c^2. \quad (4.36)$$

The values of the parameters m_{D^*} and m_A differ from the values stated in the original publication, since those were estimations for masses of particles not yet observed. Also, the values of F and D have been updated⁶. Implemented in the Monte Carlo generator is a modified version derived from [31] which includes also the term corresponding to h_A (see equation (2.57)). However, as the h_A term is proportional to the lepton mass, the differences to the calculation of Shrock and Lee are negligible.

4.2.2 The QEC Model of Kovalenko

As mentioned in Section 2.3.3, the model of Kovalenko gives an upper limit for the QEC cross section, by estimating the structure function appearing in the cross section formula (4.14) with the help of local duality (see (2.66)):

$$\int_{\bar{\xi}_{min}}^{\bar{\xi}_{max}} (F^{th}(\bar{\xi}, Q^2) - F^{ph}(\bar{\xi}, Q^2)) d\bar{\xi} \simeq 0 \quad (4.37)$$

where

$$\bar{\xi}(\nu, Q^2) = \frac{Q^2}{m_N (\nu + \sqrt{\nu^2 + Q^2})} \left[1 + \frac{M_0^2}{Q^2} \left(1 + \frac{M_0^2}{Q^2 + M_0^2} \right) \right] \quad (4.38)$$

replaces the Bjorken variable x_{Bj} , thereby taking into account some of the dominant power corrections to F^{th} for low and moderate Q^2 . In order to reproduce the cross section values given in the publication, the phenomenological parameter M_0 , which describes the scale of the internal nucleon dynamics, was set to $M_0 = \sqrt{0.1}$ in contradiction to the stated value $M_0 = 0.1$. The details of the rather tedious calculation can be found in the publication.

4.2.3 Calculation of the total QEC Cross Section

For a fixed neutrino energy E_ν the total cross section σ is obtained by integrating the differential cross section $d\sigma/dQ^2$ over the kinematically allowed Q^2 range. The variable Q^2 is determined by the 4-momentum vectors of the initial and the final state lepton:

$$\begin{aligned} Q^2 = -(k - k')^2 &= -m_l^2 + 2EE' - 2|\mathbf{k}||\mathbf{k}'| \cos \theta \\ &= -m_l^2 + 2EE' - 2E(E'^2 - m_l^2)^{1/2} \cos \theta \end{aligned} \quad (4.39)$$

⁶In the text of [6] F and D were interchanged by mistake. However, for the computation of the numerical results, the right values were used.

or equivalent by the initial and final state hadrons:

$$Q^2 = -(p_N - p_X)^2 = m_N^2 - W^2 + 2m_N(E - E') \quad (4.40)$$

where p_X denotes the 4-momentum of the hadronic final state which is in this case the charmed baryon. Equations (4.39) and (4.40) can be solved for the energy of the muon E' which yields a quadratic equation:

$$E'^2(4E^2 \cos^2 \theta - B^2) - E'(2AB) - (4E^2 m_l^2 \cos^2 \theta + A^2) = 0 \quad (4.41)$$

with

$$A = W^2 - M^2 - 2m_N E - m_l^2 \quad (4.42)$$

$$B = 2(m_N + E). \quad (4.43)$$

The solution for $|\cos \theta| = 1$ inserted into (4.39) gives the boundaries of the Q^2 range. In the process of forming equation (4.41), a second solution has been generated by squaring. This solution, however, is not valid, since it does not satisfy equation (4.39). If the neutrino energy E_ν is too small ($E_\nu < E_{\text{thr}}$), there exists no solution to the equations (4.39) and (4.41) and the total cross section vanishes. The threshold energies for the QEC processes, depending on lepton and target type, are given in Table 4.1.

Neutrino	Nucleon	E_{thr} (GeV)
ν_e	n	2.310
	p	2.738
ν_μ	n	2.571
	p	3.020
ν_τ	n	8.310
	p	9.065

Table 4.1: Threshold energy of QEC production for the different neutrinos and target nucleons in the rest frame of the nucleons.

Figure 4.5(a) and 4.5(b) show the total cross sections of the processes (4.10)-(4.12) for the model of Shrock and Lee and for the model of Kovalenko. Due to the steep Q^2 dependence of the differential cross sections (Figure 4.6(a) and 4.6(b)), the total cross sections become almost constant⁷ for neutrino energies above ≈ 15 GeV. This is a common feature of all QEC models. The energy dependence of the total cross section is mainly a result of the dilatation of the allowed Q^2 range. The flatness of the total cross section also implies that QEC can only be of relevance near its threshold energy, since the total charged current cross section rises linearly with the neutrino energy (i. e., the fraction $\sigma_{\text{QEC}}/\sigma_{\text{cc}}$ decreases). The different Q^2 dependence of the two models has an impact on the reconstruction efficiency in the NOMAD detector since it yields a different energy distribution of the produced

⁷ $\int_\xi^\infty \frac{1}{x^{1+\epsilon}} = \text{const.} < \infty$ for $\epsilon > 0$.

charmed baryons. The cross section calculated here with the model of Shrock and Lee is smaller than the one originally published (see Table 2.60): $\sigma_{\text{orig.}}(10 \text{ GeV}) = 2.3 \times 10^{-39} \text{ cm}^2$. This is an effect of the adjusted values of the mass parameters.

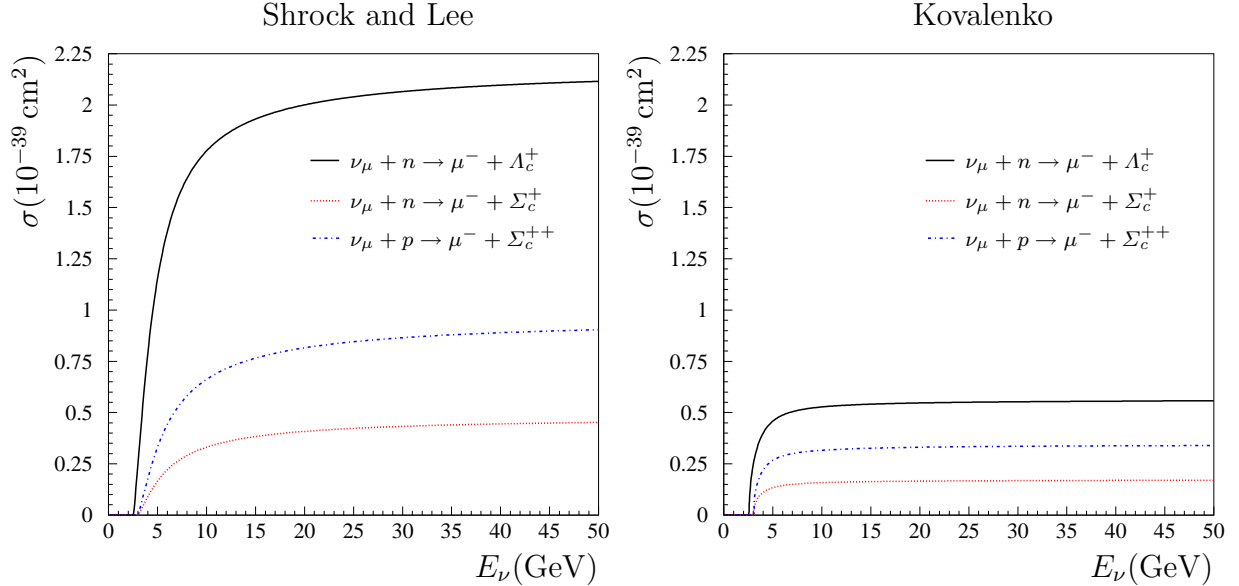


Figure 4.5: Total QEC cross sections for the model of Shrock and Lee (a) and for the model of Kovalenko (b).

4.2.4 Monte Carlo Generation of QEC Events

The purpose of Monte Carlo techniques is to map a uniform distribution of numbers $u(x)$ in an interval $[0, 1]$ to an arbitrary distribution $f(x)$ in an interval $[a, b]$. This is useful as uniform distributions $u(x)$ can be provided by random number generators on computers. There are several methods to accomplish this mapping task, depending on the properties of the function $f(x)$. Here, only the simplest method is outlined, however, more sophisticated approaches may be found in [53] and [55]. If the maximum of $f(x)$ in the range $[a, b]$ is known, $f(x) < f_{\text{max}}$, a hit-or-miss method is applicable which may be described as follows:

1. A number x_0 from the uniform distribution $u(x)$ is selected and mapped to the interval $[a, b]$ with the relation $x = a + (b - a)x_0$.
2. A second number x_1 from $u(x)$ in the interval $[0, 1]$ is selected and compared with the ratio $f(x)/f_{\text{max}}$. If $x_1 > f(x)/f_{\text{max}}$, the value x is rejected and the algorithm starts again at step 1.

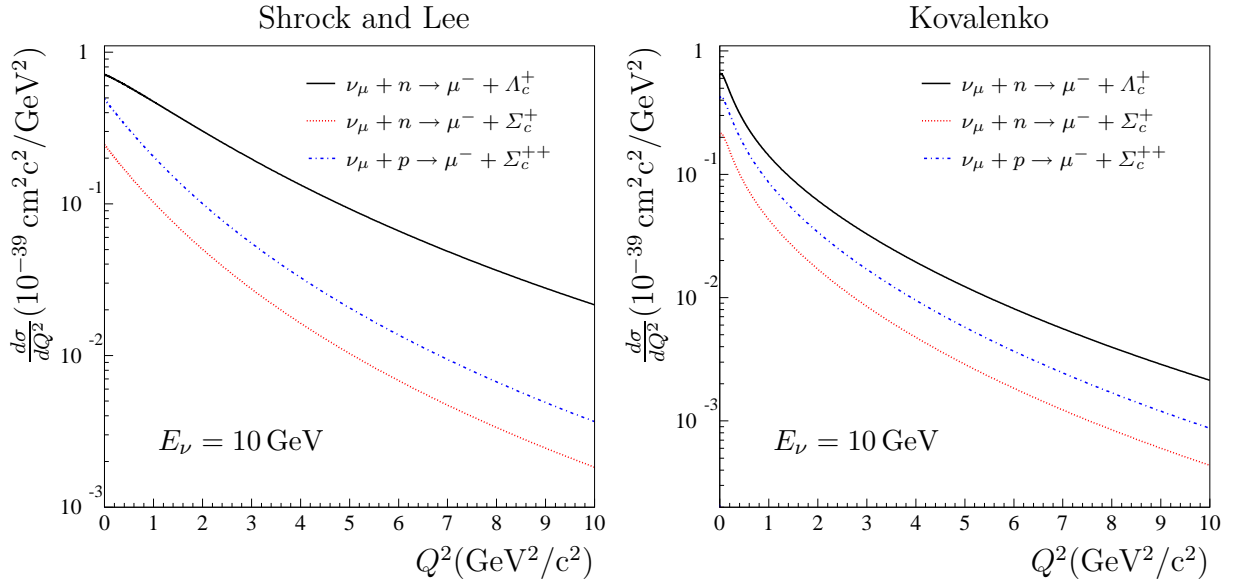


Figure 4.6: Differential QEC cross sections for the model of Shrock and Lee (a) and for the model of Kovalenko (b).

3. Otherwise, if $x_1 \leq f(x)/f_{\max}$, the value x is retained as final answer.

Since the probability that $x_1 \leq f(x)/f_{\max}$ is proportional to $f(x)$, the values x , selected by this algorithm, are distributed according to $f(x)$. This brute force method always works as long as the maximum f_{\max} is known. However, for sharply peaked functions $f(x)$, it becomes slow due to the high number of rejected values.

Since for a given neutrino energy the differential QEC cross section depends only on one variable, e. g. Q^2 , and has a known maximum, the hit-or-miss method can be applied in order to generate events with a Q^2 in the interval $[Q_{\min}^2, Q_{\max}^2]$, distributed like $d\sigma/dQ^2$. The selected Q^2 then determines the kinematics of the event, i. e. the 4-momenta of the muon p_μ and the charmed baryon p_{B_c} . Finally, the decay of the charmed baryon is taken care of by JETSET [53].

For the simulation of the detector response and for the reconstruction of the events the software packages GENOM and RECON, mentioned in Section 4.1.3, are used.

Chapter 5

Data Analysis

5.1 Introduction

The expected contribution of the QEC processes (4.10)-(4.12) to the total number of scattering events in the energy range of NOMAD,

$$\begin{aligned} N_{\text{QEC}} &= n_t \int \sigma_{\text{QEC}} \frac{dN_\nu}{dE_\nu} dE_\nu \\ n_t &= \text{nucleons per area,} \end{aligned} \quad (5.1)$$

is relatively small, namely 8.6‰ for the model of Shrock and Lee [6, 7] and 2.9‰ for the model of Kovalenko [12] respectively. The predicted fractions of quasi-elastically produced Λ_c^+ (process (4.10)) are found to be:

$$\frac{N_{\Lambda_c^+}^{\text{shr}}}{N_{\text{cc}}^{\nu\mu}} = 0.0054 \quad (5.2)$$

and

$$\frac{N_{\Lambda_c^+}^{\text{kov}}}{N_{\text{cc}}^{\nu\mu}} = 0.0015. \quad (5.3)$$

Due to the steep Q^2 dependence of the differential QEC cross section, the charmed baryon is predominantly produced with low momentum. In the NOMAD experiment the decay vertices of the charmed baryons cannot be distinguished from the primary vertex because the Λ_c^+ has a mean life time of only $\tau = (200 \pm 6) \times 10^{-15}$ s and the Σ_c^+ and Σ_c^{++} , which decay (100%) via the strong interaction into a Λ_c^+ and a pion, have an even shorter mean life time. The resolution of the squared mass of the hadronic final state, W_{vis}^2 , calculated from the visible neutrino energy E_ν^{vis} and the muon momentum, is not sufficient to separate QEC from DIS events. Therefore, the search has to be performed in exclusive decay channels. For this analysis decays into a Λ have been investigated, namely the hadronic decay,

$$\Lambda_c^+ \rightarrow \Lambda \pi^+ \pi^+ \pi^- \quad (5.4)$$

with branching ratio:

$$\Gamma_i/\Gamma_{\text{tot}} = (3.3 \pm 1.0) \%, \quad (5.5)$$

the semi-leptonic decay into a positron,

$$\Lambda_c^+ \rightarrow \Lambda e^+ \nu_e \quad (5.6)$$

$$\Gamma_i/\Gamma_{\text{tot}} = (2.1 \pm 0.6) \%,$$

and the semi-inclusive decay,

$$B_c \rightarrow \Lambda + X \quad (5.7)$$

$$\Gamma_i/\Gamma_{\text{tot}} = (35 \pm 11) \%$$

where B_c stands for Λ_c^+ , Σ_c^+ or Σ_c^{++} and X denotes an arbitrary set of final state particles. Since the Σ_c always decay into a Λ_c^+ , the branching ratio corresponds to the one of the Λ_c^+ decay. The Λ itself can be identified from its most prominent decay:

$$\Lambda \rightarrow p + \pi^- \quad (5.8)$$

$$\Gamma_i/\Gamma_{\text{tot}} = (63.9 \pm 0.5) \%$$

which gives rise to an observable secondary vertex ($\tau = 2.632 \times 10^{-10}$ s).

5.2 Data Selection

In order to find the fraction of QEC events with respect to all charged current events, a proper data¹ sample has to be selected. This sample, referred to as the ν_μ cc sample, is specified via the selection cuts given in Section 4.1.4:

- **Detector:** Proper performance of detector and beam is demanded during the data taking period (*run*). Events from previously identified “bad” runs are rejected.
- **Trigger:** The events must fulfill the $\overline{V}T_1T_2$ trigger described in section 3.2.10.
- **Primary muon:** At least one identified muon with an energy $E_\mu > 5$ GeV has to be present at the primary vertex. A muon candidate is a drift chamber track that has been matched with a track reconstructed in the muon chambers. The primary muon, which is assumed to have the highest transversal momentum with respect to the neutrino beam direction, must be negatively charged.
- **Fiducial volume:** The primary vertex has to be in a confined region within the drift chambers. In the NOMAD co-ordinate system this region is given by:

$$\begin{aligned} -120 \text{ cm} &\leq x_{V^1} \leq 120 \text{ cm} \\ -120 \text{ cm} &\leq y_{V^1} \leq 120 \text{ cm} \\ 60 \text{ cm} &\leq z_{V^1} \leq 395 \text{ cm} \end{aligned} \quad (5.9)$$

¹In this thesis the expression “data” is only used in connection with real events.

- **Track multiplicity:** Including the μ^- , at least two reconstructed primary tracks must be found. Here, a track is assumed to originate from the primary vertex if its first hit has been found in a cylinder ($radius = 30$ cm, $length = 40$ cm) with axis along the neutrino beam direction and starting 10 cm in front of the primary vertex. The number of primary tracks is denoted² by $n_{trksV^1}^{box}$.
- **Charge:** The charge sum of the primary track candidates has to fulfill

$$-1 \leq \sum_{box} Q_{trks} \leq 2. \quad (5.10)$$

The $\nu_{\mu}cc$ Monte Carlo sample selected by these criteria has been normalized to the number of data events surviving these selection cuts, as it was done in Section 4.1.4. This normalization has to be justified by investigating the contamination from neutral current processes and the charged current interactions of other neutrinos (see next section).

5.2.1 Purity of the $\nu_{\mu}cc$ Sample

In order to determine the efficiency of the selection criteria in rejecting background from neutral current reactions as well as from interactions of $\bar{\nu}_{\mu}$, ν_e and $\bar{\nu}_e$, the corresponding Monte Carlo samples have been studied. In Table 5.1 the obtained *selection efficiencies* (or *reduction factors*) along with the expected number of events before and after the selection cuts are given.

	DCH events	Selection efficiency (%)	Events in the $\nu_{\mu}cc$ sample
$\nu_{\mu}cc$	1282000	48.5 ± 0.031	622500
nc	493000	0.168 ± 0.003	830
$\bar{\nu}_e cc$	20000	0.175 ± 0.004	35
$\nu_e cc$	3000	0.254 ± 0.008	8
$\bar{\nu}_{\mu}cc$	41000	0.077 ± 0.004	30

Table 5.1: Efficiencies of the $\nu_{\mu}cc$ sample selection for Monte Carlo events produced by $\nu_{\mu}cc$ scattering and other processes. The errors of the efficiencies are statistical only. The abbreviation *DCH* stands for *drift chambers*.

The Monte Carlo samples comprise the following numbers of events:

- $\nu_{\mu}cc$: 4.9 million events; ≈ 3.8 times the data sample,
- nc : 2.4 million events; ≈ 4.9 times the data sample,
- $\nu_e cc$: 940000 events; ≈ 47 times the data sample,

²A short description of the variables used in the analysis is given in appendix A

- $\bar{\nu}_e cc$: 380000 events; ≈ 128 times the data sample,
- $\bar{\nu}_\mu cc$: 400000 events; ≈ 9.7 times the data sample.

These numbers determine the stated statistical errors for the selection efficiencies. As mentioned before, the $\nu_\mu cc$ Monte Carlo sample has been normalized to the number of data events in the $\nu_\mu cc$ sample. The expected number of $\nu_\mu cc$ events in the drift chambers (DCH events) is obtained with the help of the Monte Carlo efficiency. The number of DCH events for the other processes is then given by the ratios $N_i/N_{\nu_\mu cc}$ which are determined by the known cross sections and the neutrino energy spectra. The selection criteria discard more than 99% of the events of the background processes. At the same time about 50% of the charged current ν_μ events are rejected which is, however, to a substantial fraction due to the restriction of the fiducial volume:

$$\begin{aligned}\epsilon_{\text{volume}} &\simeq 0.72 \\ \epsilon_{\text{other}} &\simeq 0.67.\end{aligned}\tag{5.11}$$

Considering the small contribution from other processes to the $\nu_\mu cc$ sample, the proposed normalization of the $\nu_\mu cc$ Monte Carlo sample to the data sample, seems to be reasonable.

5.3 Efficiencies and Normalization of the QEC Signal Monte Carlo Samples

The search for QEC events is being performed in three different decay channels of the Λ_c^+ . For the decays with a definite final state, (5.4) and (5.6) with $\Lambda \rightarrow p + \pi^-$, 12000 signal events have been generated. The semi-inclusive decay channel (5.7) is being investigated using a Monte Carlo sample which comprises 20000 QEC signal events, each with a Λ decaying into a proton and a π^- . The application of the selection cuts defining the $\nu_\mu cc$ sample reduces the QEC signal samples to the following fractions:

- $\Lambda_c^+ \rightarrow \Lambda \pi^+ \pi^+ \pi^-$:

$$\epsilon_{\nu_\mu cc}^{\text{shr}} = 0.588 \pm 0.007\tag{5.12}$$

$$\epsilon_{\nu_\mu cc}^{\text{kov}} = 0.599 \pm 0.007\tag{5.13}$$

- $\Lambda_c^+ \rightarrow \Lambda e^+ \nu_e$:

$$\epsilon_{\nu_\mu cc}^{\text{shr}} = 0.570 \pm 0.007\tag{5.14}$$

$$\epsilon_{\nu_\mu cc}^{\text{kov}} = 0.575 \pm 0.007\tag{5.15}$$

- $B_c \rightarrow \Lambda + X$:

$$\epsilon_{\nu_\mu cc}^{\text{shr}} = 0.580 \pm 0.005\tag{5.16}$$

$$\epsilon_{\nu_\mu cc}^{\text{kov}} = 0.571 \pm 0.005,\tag{5.17}$$

The selection efficiencies are substantially higher than the efficiencies of the $\nu_\mu cc$ background Monte Carlo events shown in Table 5.1. This is an effect of the relatively high mass of the charmed baryons which gives a lower bound to the momentum that has to be transferred from the neutrino.

The Monte Carlo signal samples have been normalized to the numbers of expected QEC signal events in the DCH which can be determined via the number of expected $\nu_\mu cc$ DCH events (see Table 5.1) and the production and branching ratios given in Section 5.1. The expected numbers of signal events in the $\nu_\mu cc$ sample for both QEC models are given in Table 5.2.

Search Channel	Events in the $\nu_\mu cc$ sample	
	Kovalenko	Shrock
$\Lambda_c^+ \rightarrow \Lambda \pi^+ \pi^+ \pi^-$	27.7	86.5
$\Lambda_c^+ \rightarrow \Lambda l^+ \nu_l$	15.1	53.4
$B_c \rightarrow \Lambda + X$	476.7	1443.6

Table 5.2: Expected numbers of signal events in the $\nu_\mu cc$ sample.

5.4 Selection and Identification of V^0 Vertices

The decay channels (5.4)-(5.7) of the Λ_c^+ all include a Λ in the final state. Being a neutral baryon, the Λ may decay weakly into a neutron and a π^0 ($\Gamma_i/\Gamma = 35.8\% \pm 0.5\%$), or into a proton and a π^- ($\Gamma_i/\Gamma = 63.9\% \pm 0.5\%$). Due to the mean life time of $(2.632 \pm 0.020) \times 10^{-10}$ s ($c\tau = 7.89$ cm), the latter decay may be observed in the drift chambers as two charged tracks which originate from a secondary vertex. These secondary vertices with two outgoing but no incoming tracks are called V^0 vertices. The identification of a Λ is thus accomplished by searching for a V^0 vertex and taking advantage of kinematic characteristics to separate the Λ from other particles, such as $\bar{\Lambda}$, K_S^0 and γ , whose decays or interactions might also lead to V^0 vertices.

The V^0 vertices in the drift chambers have been labeled by the NOMAD vertex fitting package [56], using the Kalman filter technique. In order to reject misidentified V^0 vertices the following constraints have been demanded:

- $\mathcal{P}(\chi_{V^0}^2) > 0.01$, where \mathcal{P} is the χ^2 probability of the vertex fit of the V^0 vertex.
- $p_T^{l.o.f} < 0.1$ GeV/c, where $p_T^{l.o.f}$ is the transverse momentum of the decaying particle with respect to the line of flight, as illustrated in Figure 5.1. This gives a measure on the probability of the neutral particle to have emanated from the primary vertex.
- The measured proper decay time of the V^0 vertex has to be consistent with the mean life time given in [25] for the tested hypothesis of either a decaying Λ , $\bar{\Lambda}$ or K_S^0 :

$$\tau < 6\tau_{V^0}. \quad (5.18)$$

The remaining photon candidates are removed by a kinematic cut which will be described later.

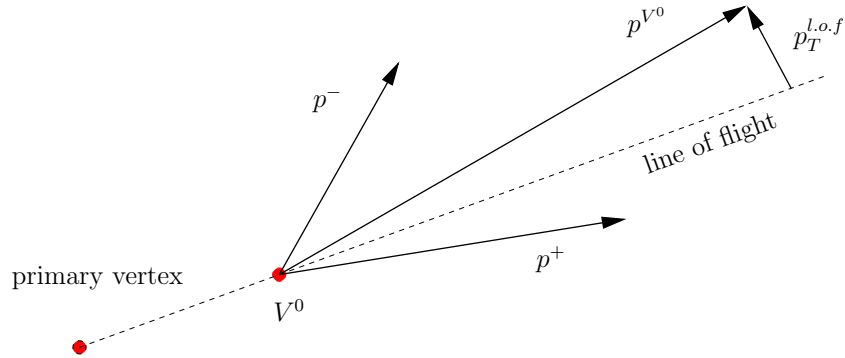


Figure 5.1: Definition of the transverse momentum of a particle with respect to the line of flight.

Figure 5.2 gives a schematic view of the momenta, p^+ and p^- , of the positively and negatively charged particles participating in a V^0 decay, split into transverse and longitudinal components with respect to the momentum of the parent particle, p^{V^0} . One possibility

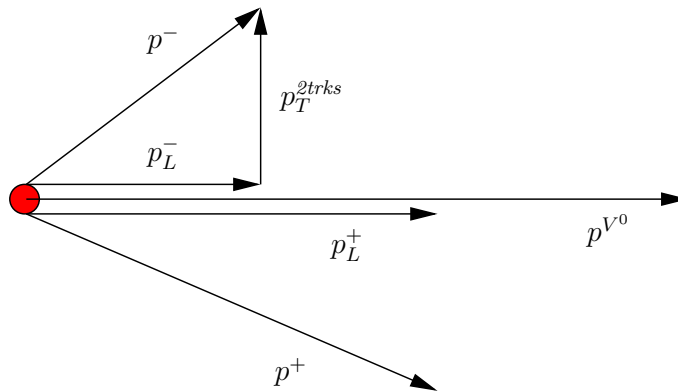


Figure 5.2: Schematic definition of the kinematic variables for a two-body decay of a neutral particle.

to recognize a Λ is by reconstructing the mass ($m_\Lambda = (1115.683 \pm 0.006) \text{ MeV}/c^2$) from the charged tracks of the decay particles, assuming them to be proton and pion. An alternative method arises from the mass difference between the proton and the pion. The Lorentz transformation, boosting the 4-momenta of the proton and the pion from the rest frame of the Λ to the laboratory system, results generally in a higher momentum for the proton compared to the pion. This can be seen from the transformation that boosts along

an arbitrary axis, e. g. the z-axis:

$$\begin{pmatrix} E \\ p_x \\ p_y \\ p_z \end{pmatrix} = \begin{pmatrix} \gamma & 0 & 0 & \beta\gamma \\ 0 & 1 & 0 & 0 \\ 0 & 0 & 1 & 0 \\ \beta\gamma & 0 & 0 & \gamma \end{pmatrix} \begin{pmatrix} E^0 \\ p_x^0 \\ p_y^0 \\ p_z^0 \end{pmatrix} = \begin{pmatrix} \gamma E^0 + \gamma\beta p_z^0 \\ p_x^0 \\ p_y^0 \\ \gamma p_z^0 + \gamma\beta E^0 \end{pmatrix} \quad (5.19)$$

with p^0 referring to the 4-momentum of a particle in the rest frame of the Λ where

$$\mathbf{p}^{+0} = -\mathbf{p}^{-0}.$$

If the velocity between the laboratory frame and the rest frame of the Λ is high enough (for Λ decays: $\beta > 0.26$), the particle with the higher mass receives more momentum because of its higher rest frame energy E^0 . From the longitudinal components of the proton and pion momenta, p_L^+ and p_L^- , an asymmetry parameter can be constructed:

$$\alpha^{2trks} = \frac{p_L^+ - p_L^-}{p_L^+ + p_L^-}. \quad (5.20)$$

The transverse momentum p_T^{2trks} is by definition the same for both decay particles. The 2-dimensional plot of α^{2trks} versus p_T^{2trks} is known as Podolanski-Armenteros plot. It can be shown that in this plot the values of Λ lie in a confined region. In Figure 5.3 the distribution of V^0 vertices is shown for data before and after the selection cuts described above. The Λ appear in region (II) with $\alpha^{2trks} > 0$. The $\bar{\Lambda}$, being the charge conjugates, populate region (I) with $\alpha^{2trks} < 0$. The distribution of K_S^0 is symmetric in α^{2trks} since the decay particles, π^+ and π^- , have the same mass. The photon conversions are found in the region with small p_T^{2trks} due to their vanishing mass. Hence, asking for $p_T^{2trks} > 0.06$ GeV/c rejects most of the V^0 vertices from $\gamma \rightarrow e^+e^-$. For the search for QEC events in the decay channels (5.4)-(5.7), the Λ candidates are required to lie in the region:

$$\begin{aligned} 0.4 &\leq \alpha^{2trks} \leq 0.93 \\ 0.06 \text{ GeV/c} &\leq p_T^{2trks} \leq 0.12 \text{ GeV/c}. \end{aligned} \quad (5.21)$$

5.5 Search in the Decay Channel: $\Lambda_c^+ \rightarrow \Lambda \pi^+ \pi^+ \pi^-$

A quasi elastically produced Λ_c^+ , which decays into a Λ and three pions, should lead ideally to an event with a primary muon, exactly four charged tracks from the primary vertex ($\mu^- \pi^+ \pi^+ \pi^-$), and, in case the Λ decays into proton and pion, to a secondary V^0 vertex. Figure 5.4 shows such an event, taken from the Monte Carlo simulation. The QEC signal³ events can thus be characterized by the following criteria:

³The search in the exclusive channels $\Lambda_c^+ \rightarrow \Lambda \pi^+ \pi^+ \pi^-$ and $\Lambda_c^+ \rightarrow \Lambda e^+ \nu_e$ has been optimized for quasi elastically produced Λ_c^+ (process (4.10)). The chosen selection criteria suppress events which include Σ_c^+ and Σ_c^{++} .

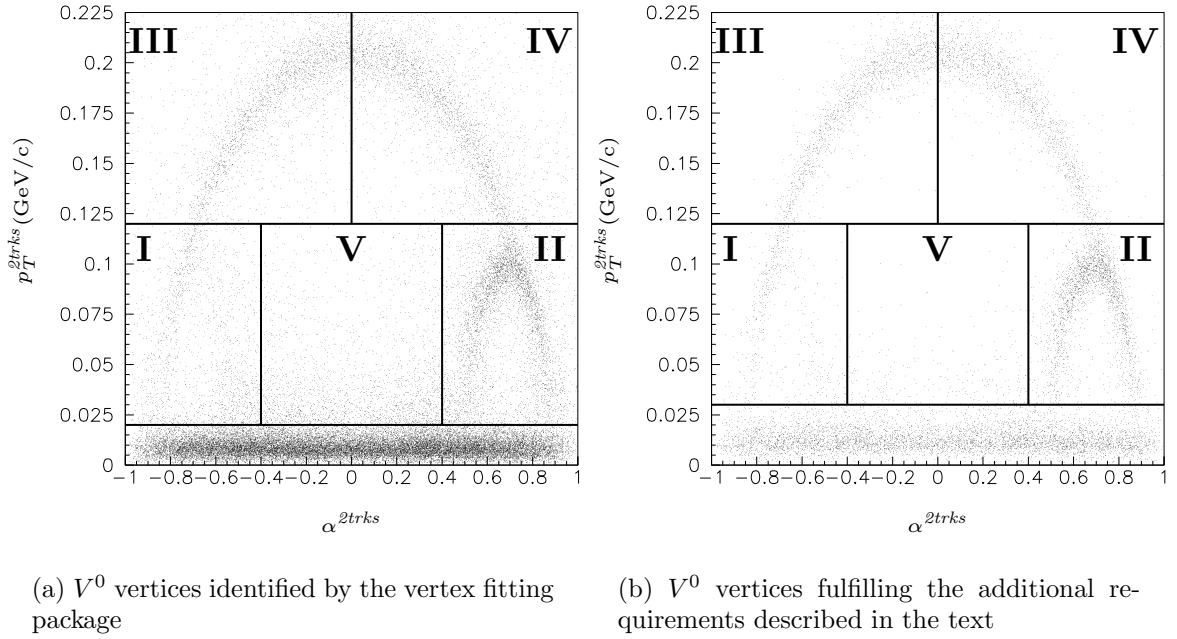


Figure 5.3: Podolanski-Armenteros plot: $\bar{\Lambda}$ and Λ populate the regions I and II respectively, while the K_s^0 are distributed symmetrically in all regions except V. Photon conversions populate the region with small p_T^{2trks} .

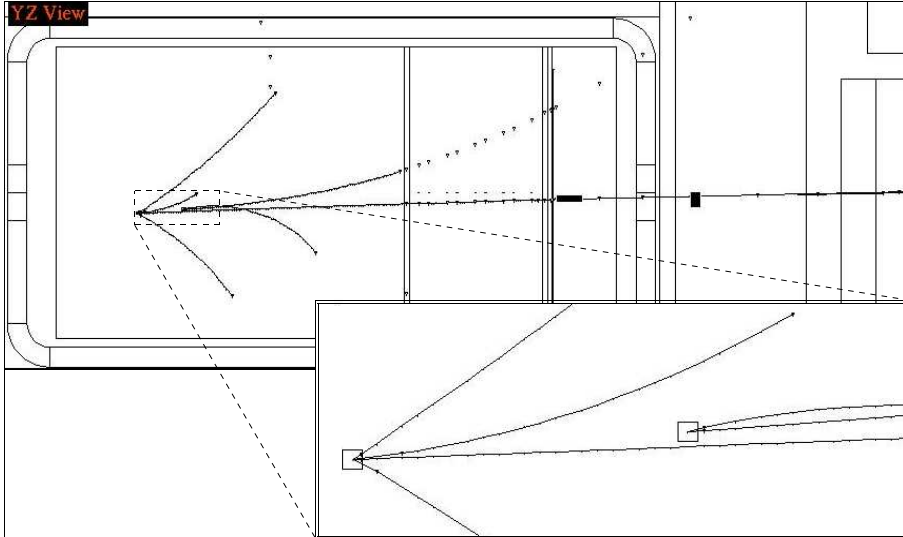


Figure 5.4: Display of a QEC event with $\Lambda_c^+ \rightarrow \Lambda \pi^+ \pi^+ \pi^-$, taken from the Monte Carlo simulation.

- $E_{cal}^{neutral} < 1.0 \text{ GeV}$: The reconstructed energy deposit of neutral particles in the ECAL should be small since there should be no neutral particles originating from the QEC process or the exclusive decays of the Λ_c^+ . Neutral particles arise mainly from low energy secondary interactions. As shown in Figure 5.5, the distribution of $E_{cal}^{neutral}$ for energies below 1 GeV is not well described in the Monte Carlo simulation. The distortion could be an indication of an inaccurate description of the photon propagation in the detector simulation or of an underestimation of noise effects. However, for the sum of events with $E_{cal}^{neutral} < 1.0 \text{ GeV}$ a good agreement between data and Monte Carlo is found.

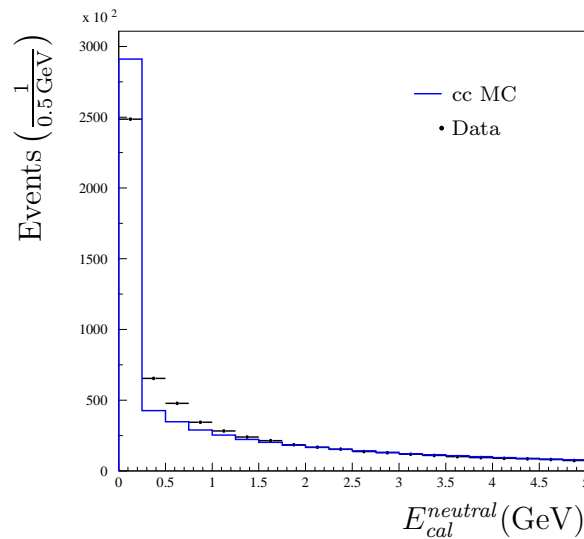


Figure 5.5: ECAL energy deposit by neutral particles.

- $2 \text{ GeV}^2/c^4 < W_{vis}^2 < 8 \text{ GeV}^2/c^4$: The square of the hadronic mass reconstructed from the visible neutrino energy and the muon energy, E_{ν}^{vis} and E_{μ} , should be in a range compatible with the Λ_c^+ mass, $m_{\Lambda_c^+}^2 = 5.22 \text{ GeV}^2/c^4$.
- $n_{V^0} = 1$: There has to be a reconstructed V^0 vertex fulfilling the selection requirements described in Section 5.4, namely:

$$\mathcal{P}(\chi_{V^0}^2) > 0.01 \quad (5.22)$$

$$p_T^{l.o.f} < 0.1 \text{ GeV}/c \quad (5.23)$$

$$\tau < 6\tau_{V^0} \quad (5.24)$$

$$p_T^{2trks} > 0.06 \text{ GeV}/c. \quad (5.25)$$

- **Λ identification**: The reconstructed α^{2trks} and p_T^{2trks} of the particles emerging from

the V^0 vertex are required to lie in a confined region:

$$\begin{aligned} 0.4 &\leq \alpha^{2trks} \leq 0.93 \\ 0.06 \text{ GeV}/c &\leq p_T^{2trks} \leq 0.12 \text{ GeV}/c. \end{aligned} \quad (5.26)$$

- $|M_{rec}^{A_c^+} - m_{A_c^+}| < 2\sigma_M$: Assuming pion masses for the charged primary tracks and proton and pion masses for the tracks from the V^0 vertex, a total mass may be calculated from the measured momenta. This reconstructed A_c^+ mass has to be consistent with the value from [25] within the experimental resolution. From the QEC Monte Carlo simulation the mass resolution is found to be $\sigma_M = 0.047 \text{ GeV}/c^2$.
- $n_{trksV^1}^{box} = 4$: The number of reconstructed primary tracks should correspond to the number of pions originating from the A_c^+ decay plus the muon track from the primary interaction.
- $\sum_{box} Q_{trks} = 0$: For a target being a neutron the total charge must vanish.

The efficiencies of these cuts in separating the QEC signal from the $\nu_\mu cc$ background have been determined with Monte Carlo samples consisting of about 12000 signal events for both QEC models (see Section 5.3) and the $\nu_\mu cc$ Monte Carlo sample mentioned in Section 5.2.1. In Table 5.3 the values are given after each cut along with the expected number of events. Due to the relatively small branching ratio for the decay $A_c^+ \rightarrow \Lambda \pi^+ \pi^+ \pi^-$ (see

	MCCC BACKGROUND		MC SIGNAL KOV.		MC SIGNAL SHR.	
	ϵ [%]	EVENTS	ϵ [%]	EVENTS	ϵ [%]	EVENTS
$\nu_\mu cc$ SAMPLE	100.0000	622519.0	100.0	24.7	100.0	86.5
$E_{cal}^{neutral} < 1.0 \text{ GeV}$	48.8003	303790.9	99.3	24.5	98.5	85.3
$2 \text{ GeV}^2/c^4 < W_{vis}^2 < 8 \text{ GeV}^2/c^4$	18.9667	118071.4	92.2	22.8	88.1	76.2
$n_{V^0} = 1$	0.2125	1322.6	20.4	5.0	21.8	18.9
Λ SELECTION	0.1180	734.9	20.1	5.0	21.5	18.6
$ M_{rec}^{A_c^+} - m_{A_c^+} < 2\sigma_M$	0.0148	91.8	10.2	2.5	12.7	11.0
$n_{trksV^1}^{box} = 4$	0.0045	28.0	10.1	2.5	12.6	10.9
$\sum_{box} Q_{trks} = 0$	0.0039	24.3	10.0	2.5	12.5	10.8

Table 5.3: $A_c^+ \rightarrow \Lambda \pi^+ \pi^+ \pi^-$: Expected numbers of surviving events and efficiencies of the signal and the background from the Monte Carlo simulations.

(5.1)), only few QEC signal events are expected in the $\nu_\mu cc$ sample. The requirement of a reconstructed V^0 vertex, which is crucial for the background rejection, also reduces the QEC signal significantly. The quasi elastic process produces A_c^+ which are almost at rest. The decay particles, one of them being the Λ , have little energy to share which makes their reconstruction less efficient and, thus, only about 20% of the V^0 vertices are found. The small difference between the efficiencies of the two QEC models is a result of the different Q^2 dependence of their differential cross sections. Figure 5.6(a) and 5.6(b) show

the W_{vis}^2 distribution for QEC signal events. Since the resolution of W_{vis}^2 is, obviously, not sufficient to identify the quasi elastically produced Λ_c^+ , only a loose cut is applied in order to reject events with high energy in the hadronic system. As mentioned in Section 4.1.4, the description of the hadronic mass distribution by the Monte Carlo simulation is not very good. In the region below $1.5 \text{ GeV}^2/c^4$ (see Figure 5.6(c)) there is an excess of Monte Carlo events which is probably due to an inadequate simulation of low energy events. The impact of the disagreement is alleviated by the rather large width of the region of allowed W_{vis}^2 values. The $M_{rec}^{A_c^+}$ distributions of the QEC signal events in Figure 5.7(a) and 5.7(b) show a narrow peak at the value of the Λ_c^+ mass. Events with missing pion tracks give rise to the bump just below the Λ_c^+ mass. Restricting the values of $M_{rec}^{A_c^+}$, thus, not only suppresses background events but also rejects badly reconstructed signal events. The number of primary tracks is shown in Figure 5.8. Considering the large statistical errors, the agreement between Monte Carlo and data is acceptable. The demand for vanishing total charge has only a small effect since the charge states ± 1 have already been ruled out by fixing the number of tracks.

The contribution of QEC events which do not belong to the signal sample⁴ has been estimated with the help of inclusive Monte Carlo samples which comprise 100000 events. The expected number of events for both QEC models and the efficiencies⁵ are given in Table 5.4. From the final numbers in Table 5.3 and Table 5.4 it is clear that for the two

	KOVALENKO		SHROCK	
	ϵ [%]	EVENTS	ϵ [%]	EVENTS
DCH Volume	100.0000	3694.5	100.0000	10986.1
Signal Sample	0.0545	2.0	0.0482	5.3

Table 5.4: Inclusive QEC: Contribution of Σ_c^+ , Σ_c^{++} and Λ_c^+ events not fulfilling the classifications of the signal sample.

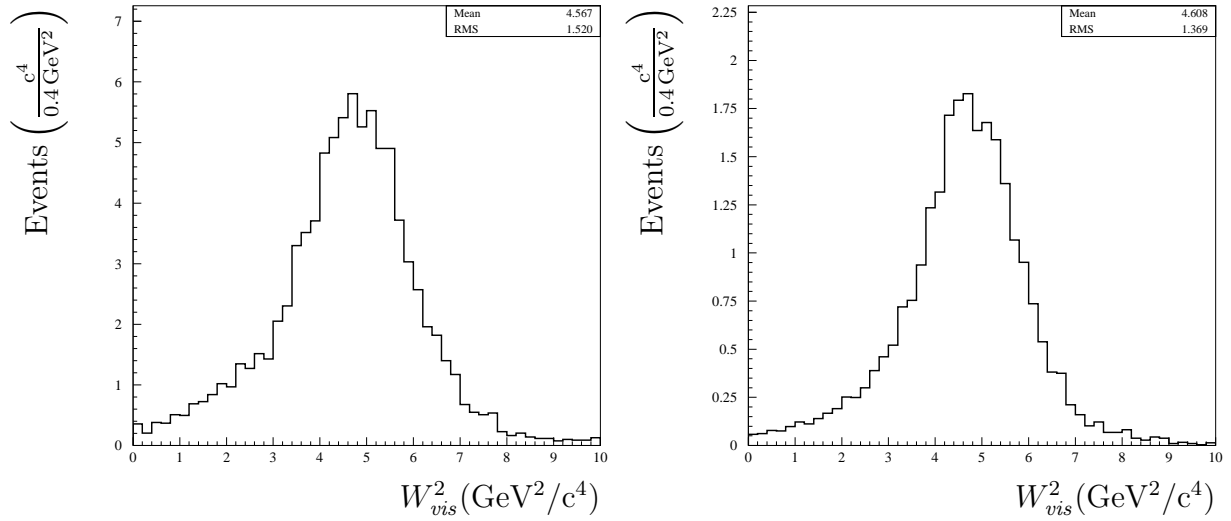
investigated models at most a small excess of data events is expected. A strong suppression of background events is achieved by the selection criteria, however, due to reconstruction inefficiencies for low energy events only about 10% of the signal events survive. In Table 5.5 the expected numbers of $\nu_\mu cc$ Monte Carlo events are compared with the numbers of surviving events in the data. No significant deviations are found.

5.6 Search in the Decay Channel: $\Lambda_c^+ \rightarrow \Lambda e^+ \nu_e$

A quasi elastic event which includes a semi-leptonic decay of a Λ_c^+ into a Λ , a positron and a neutrino should feature one positively charged primary track additional to the track of

⁴Quasi elastically produced Σ_c^+ and Σ_c^{++} as well as Λ_c^+ which decay into different channels do not belong to the defined signal.

⁵Here, the total reduction is given, including the $\nu_\mu cc$ sample selection.



(a) Signal Monte Carlo sample: Shrock and Lee

(b) Signal Monte Carlo sample: Kovalenko

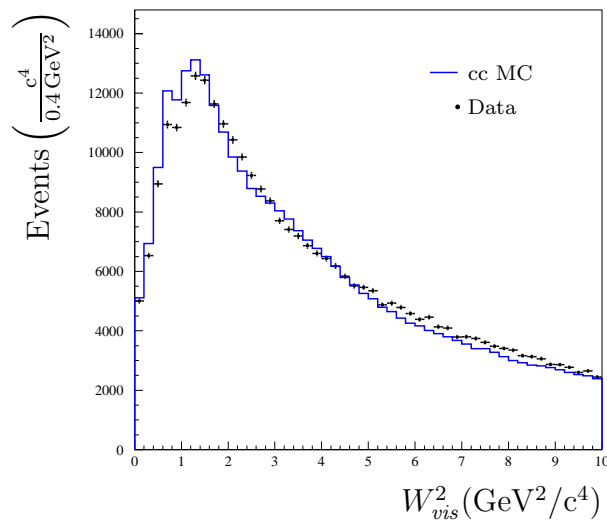
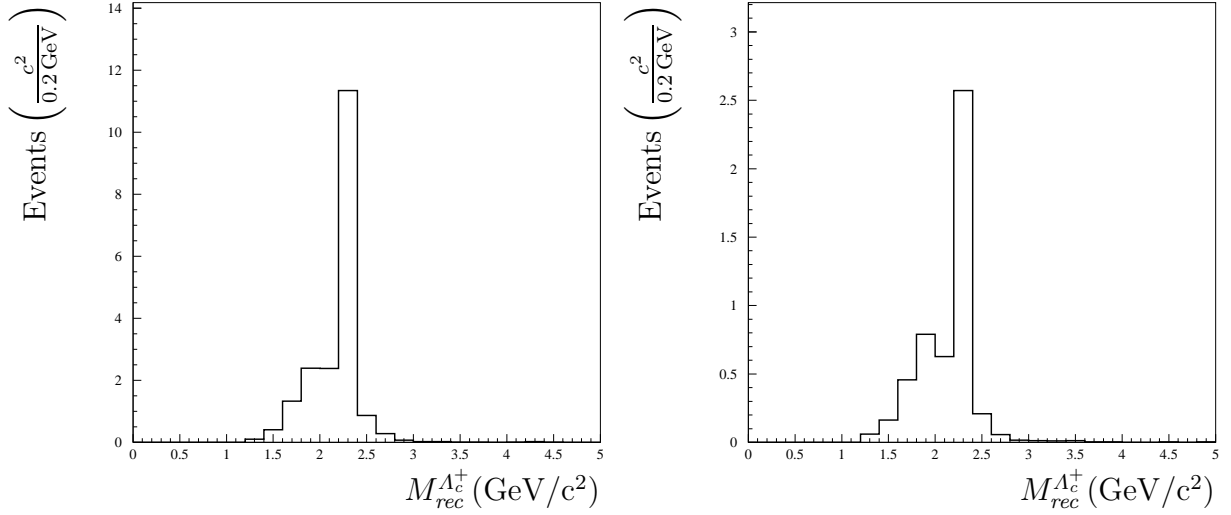
(c) Data and $\nu_\mu cc$ Monte Carlo sample

Figure 5.6: Invariant mass of the hadronic system for events with limited energy deposit by neutral particles in the ECAL (searched decay channel: $\Lambda_c^+ \rightarrow \Lambda \pi^+ \pi^+ \pi^-$).



(a) Signal Monte Carlo sample: Shrock and Lee

(b) Signal Monte Carlo sample: Kovalenko

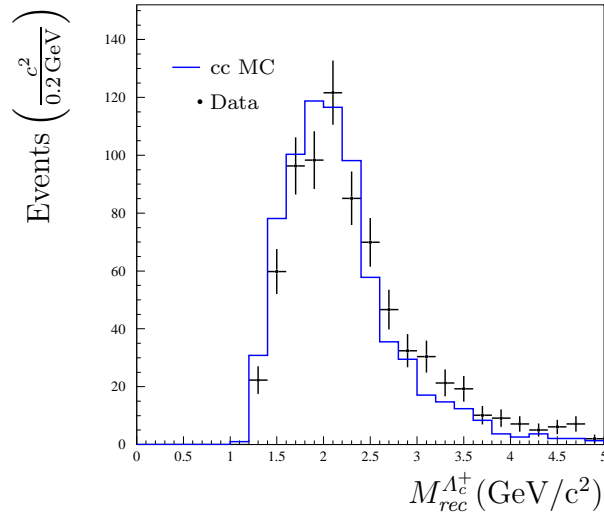
(c) Data and ν_μ cc Monte Carlo sample

Figure 5.7: Reconstructed invariant mass of the Λ_c^+ assuming the primary tracks to be pions and the V^0 to origin from a Λ decay (searched decay channel: $\Lambda_c^+ \rightarrow \Lambda \pi^+ \pi^+ \pi^-$).

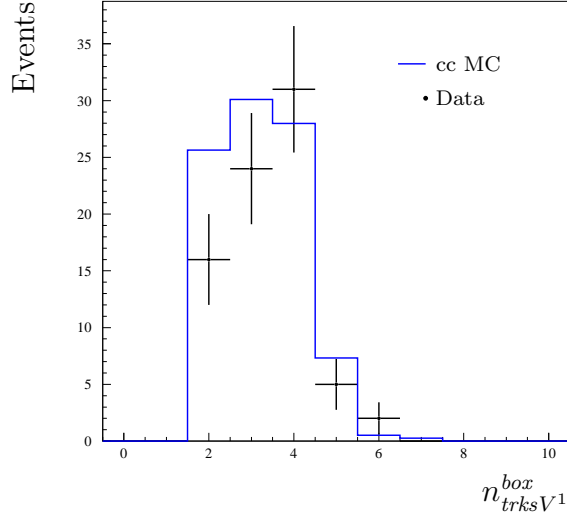


Figure 5.8: Number of charged primary tracks.

	MCCC BACKGROUND		DATA	
	ϵ [%]	EVENTS	ϵ [%]	EVENTS
$\nu_{\mu}cc$ SAMPLE	100.0000	622519.0	100.0000	622519
$E_{cal}^{neutral} < 1.0 \text{ GeV}$	48.8003	303790.9	49.1121	305732
$2 \text{ GeV}^2/c^4 < W_{vis}^2 < 8 \text{ GeV}^2/c^4$	18.9667	118071.4	19.0238	118427
$n_{V^0} = 1$	0.2125	1322.6	0.2199	1369
Λ SELECTION	0.1180	734.9	0.1205	750
$ M_{rec}^{\Lambda_c^+} - m^{\Lambda_c^+} < 2\sigma_M$	0.0148	91.8	0.0125	78
$n_{trksV1}^{box} = 4$	0.0045	28.0	0.0050	31
$\sum_{box} Q_{trks} = 0$	0.0039	24.3	0.0042	26

Table 5.5: $\Lambda_c^+ \rightarrow \Lambda \pi^+ \pi^+ \pi^-$: Numbers of surviving events and efficiencies for the data and the background Monte Carlo simulation.

the primary muon and possibly a secondary V^0 vertex from the decaying Λ . Figure 5.9 shows a Monte Carlo event which comprehends these properties.

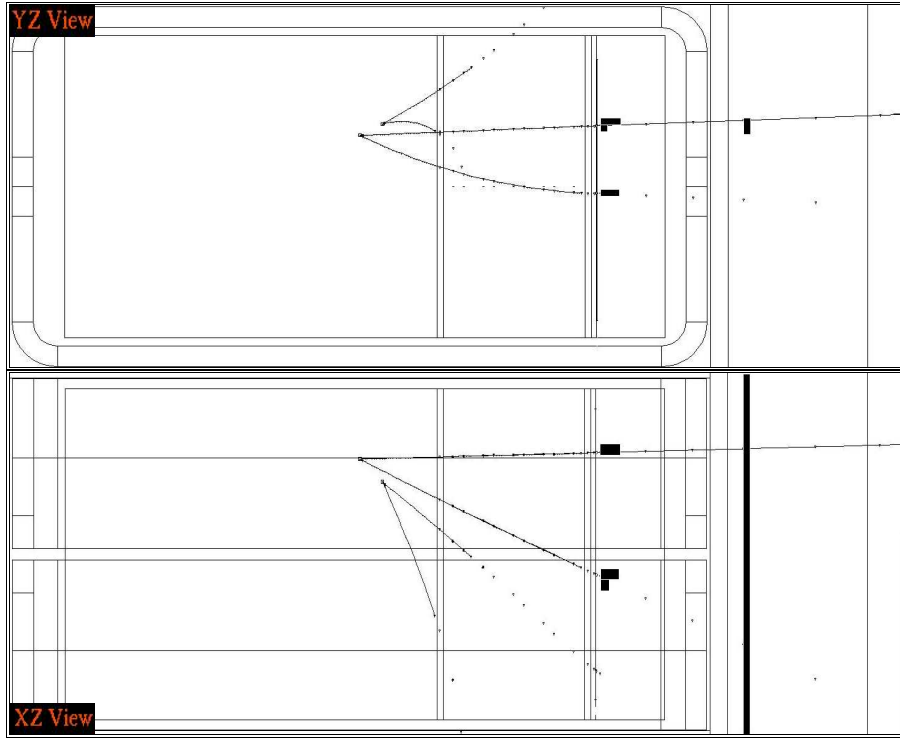


Figure 5.9: Display of a QEC event with $\Lambda_c^+ \rightarrow \Lambda e^+ \nu_e$, taken from the Monte Carlo simulation. Top view (yz) and side view (xz) of the event are presented.

The momentum carried away by the ν_e results in an unbalance of the total transverse momentum of the event with respect to the neutrino beam direction.

The positron may be identified via its energy deposition in the PRS and the ECAL. The normalized difference between the momentum measured in the DCH and the energy determined from the ECAL⁶, $(E_{clu}^{cal} - p_{\pi}^{dch}) / (E_{clu}^{cal} + p_{\pi}^{dch})$, is used to discriminate electrons and positrons from pions. Figure 5.10(a) shows the distribution of $(E_{clu}^{cal} - p_{\pi}^{dch}) / (E_{clu}^{cal} + p_{\pi}^{dch})$ for tracks taken from the Monte Carlo simulation. In Figure 5.10(b) the PRS energy deposit of simulated electrons and pions is shown. The electrons lose on average more energy due to shower formation.

A QEC signal event in this decay channel can be characterized as follows:

- $E_{cal}^{neutral} < 1.0 \text{ GeV}$: As described in Section 5.5, only little energy should be deposited in the ECAL by neutral particles.

⁶The energy corresponds to the cluster energy found in the ECAL. The momentum is determined by a fit of the drift chamber track assuming the particle to be a pion.

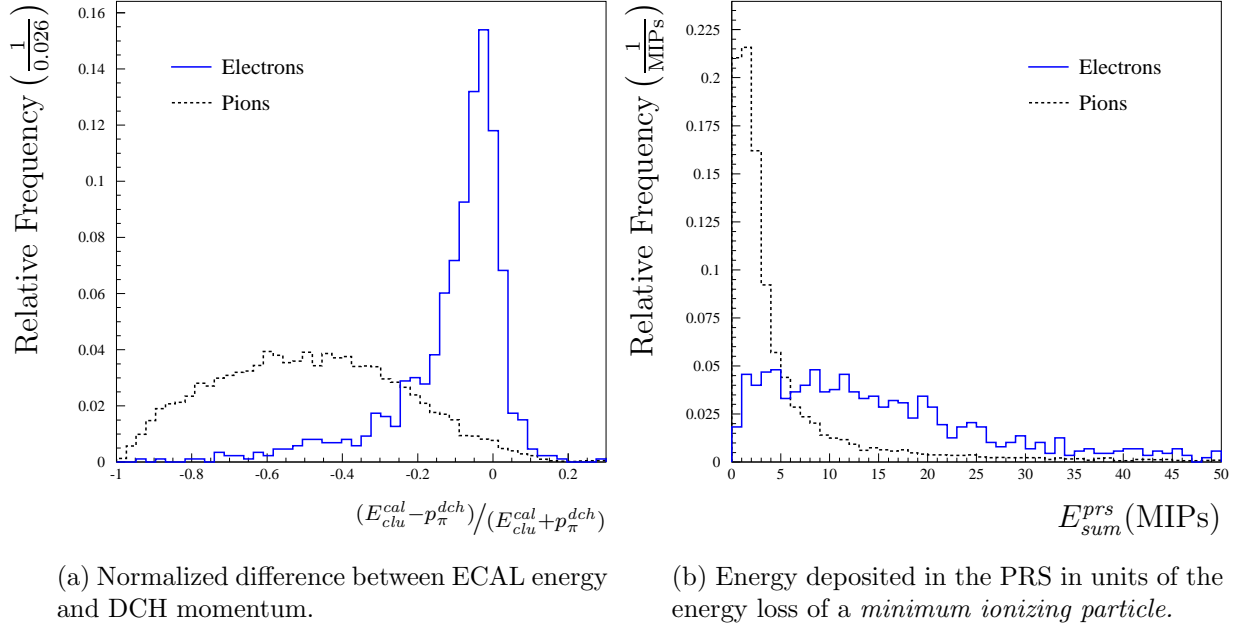


Figure 5.10: Distribution of the discrimination variables used for the electron identification. The pion sample is taken from the $\nu_{\mu}cc$ Monte Carlo. The electron distributions stem from the e^{+} taken from the QEC Monte Carlo with $\Lambda_c^{+} \rightarrow \Lambda e^{+} \nu_e$. The momentum p_{π}^{dch} is determined by a fit of the DCH track, assuming the particle to be a pion.

- $\text{GeV}^2/c^4 < W_{vis}^2 < 8 \text{ GeV}^2/c^4$: The square of the hadronic mass reconstructed from the visible neutrino and the muon energy, E_{ν}^{vis} and E_{μ} , should be in a range compatible with the Λ_c^{+} mass, $m_{\Lambda_c^{+}}^2 = 5.22 \text{ GeV}^2/c^4$.
- $n_{V^0} = 1$: There has to be a reconstructed V^0 vertex fulfilling the selection requirements described in Section 5.4, namely:

$$\mathcal{P}(\chi_{V^0}^2) > 0.01 \quad (5.27)$$

$$p_T^{l.o.f} < 0.1 \text{ GeV}/c \quad (5.28)$$

$$\tau < 6\tau_{V^0} \quad (5.29)$$

$$p_T^{2trks} > 0.06 \text{ GeV}/c. \quad (5.30)$$

- **Λ identification:** The reconstructed α^{2trks} and p_T^{2trks} of the particles emerging from the V^0 vertex are required to lie in a confined region:

$$\begin{aligned} 0.4 &\leq \alpha^{2trks} \leq 0.93 \\ 0.06 \text{ GeV}/c &\leq p_T^{2trks} \leq 0.12 \text{ GeV}/c. \end{aligned} \quad (5.31)$$

- $n_{V^1 cal}^{box} = 1$: There has to be exactly one track from the primary vertex additional to the one of the muon. For the purpose of identification that track is required to reach the PRS and the ECAL.
- $(E_{clu}^{cal} - p_{\pi}^{dch}) / (E_{clu}^{cal} + p_{\pi}^{dch}) > -0.125$: The energy deposit of a positron candidate in the ECAL should be of the same order as its momentum measured in the drift chambers.
- $E_{sum}^{prs} > 5 \text{ MIPs}$: The energy deposit of the positron candidate in the PRS must exceed 5 times the energy deposit of a *minimum ionizing particle*.

The signal selection efficiencies and the background reduction factors have been determined by means of the Monte Carlo samples mentioned in Section 5.3 and 5.2.1. In Table 5.6 the impact of the selection cuts on the efficiencies is given sequentially. The number of charged

	MCCC BACKGROUND		MC SIGNAL KOV.		MC SIGNAL SHR.	
	ϵ [%]	EVENTS	ϵ [%]	EVENTS	ϵ [%]	EVENTS
$\nu_{\mu}cc$ SAMPLE	100.0000	622542.0	100.0	15.1	100.0	53.4
$E_{cal}^{neutral} < 1.0 \text{ GeV}$	48.7988	303793.2	97.8	14.8	97.1	51.8
$2 \text{ GeV}^2/c^4 < W_{vis}^2 < 8 \text{ GeV}^2/c^4$	18.9661	118071.7	80.1	12.1	74.2	39.6
$n_{V^0} = 1$	0.2124	1322.5	17.0	2.6	16.9	9.0
Λ SELECTION	0.1180	734.9	16.8	2.5	16.7	8.9
$n_{V^1 cal}^{box} = 1$	0.0134	83.2	2.3	0.3	3.1	1.7
$(E_{clu}^{cal} - p_{\pi}^{dch}) / (E_{clu}^{cal} + p_{\pi}^{dch}) > -0.125$	0.0004	2.4	1.7	0.3	2.3	1.2
$E_{sum}^{prs} > 5.0 \text{ MIPs}$	0.0000	0.3	1.4	0.2	2.0	1.1

Table 5.6: $\Lambda_c^+ \rightarrow \Lambda e^+ \nu_e$: Expected numbers of surviving events and efficiencies for the signal and the background Monte Carlo simulations.

current background events in the $\nu_{\mu}cc$ sample is not exactly equal to the numbers stated for the other two decay channels (see Table 5.3 and Table 5.9), due to a slightly different counting of the primary tracks.

Figure 5.11 shows the distributions of the reconstructed hadronic mass for the samples of both signal and the background Monte Carlo events. The W_{vis}^2 distribution of the QEC events is shifted towards lower values, because of the momentum carried away by the ν_e . Hence, about 20 % of the signal events have an W_{vis}^2 below $2 \text{ GeV}^2/c^4$ and are discarded by the restriction of the W_{vis}^2 range. Since not all of the final state particles can be observed, it is not possible to reconstruct the mass of the Λ_c^+ directly from the measured momenta of the primary tracks. As already seen in Section 5.5 the reconstruction of the V^0 vertices is rather inefficient and reduces the signal sample to about 20 %. An even more substantial deflation of the signal sample is introduced by demanding the e^+ track to reach the PRS and the ECAL, again an effect of the lack of energy in the hadronic system. This inefficiency is, however, justified by the vast background reduction of more than two orders of magnitude which results from the electron identification. The distributions of $(E_{clu}^{cal} - p_{\pi}^{dch}) / (E_{clu}^{cal} + p_{\pi}^{dch})$ and E_{sum}^{prs} for both signal and the $\nu_{\mu}cc$ background Monte Carlo events are shown in Figures 5.12 and 5.13. The total charge is fixed since events with a negatively charged track

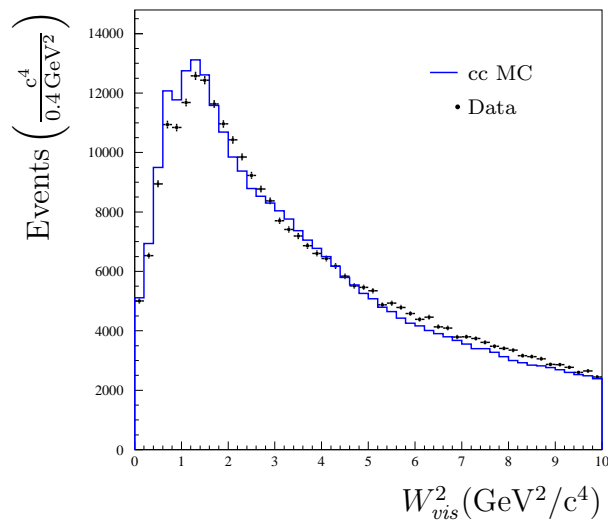
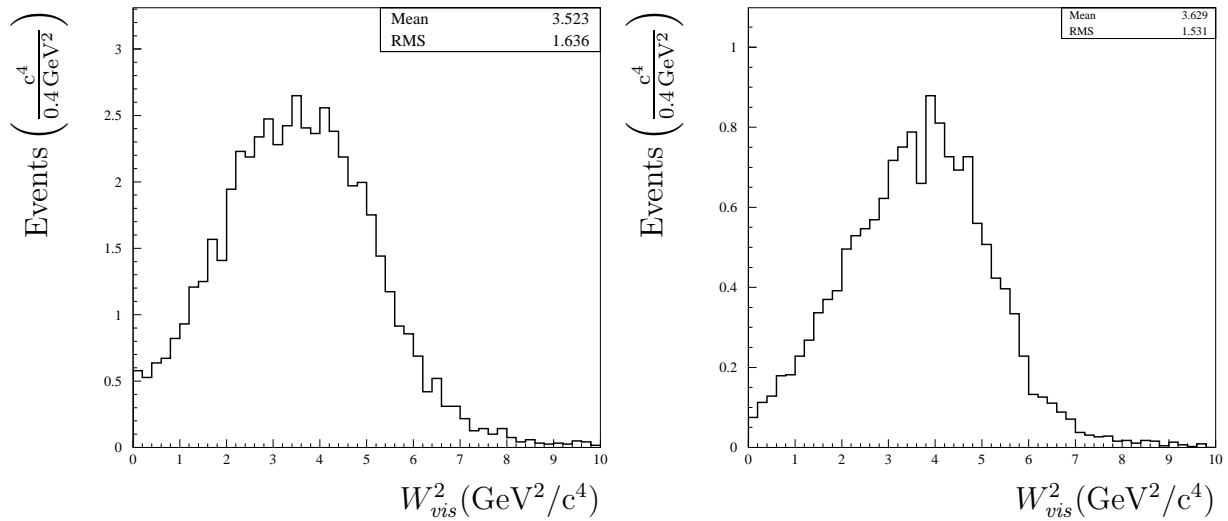
(c) Data and $\nu_\mu cc$ Monte Carlo sample

Figure 5.11: Invariant mass of the hadronic system for events with limited energy deposit by neutral particles in the ECAL (searched decay channel: $\Lambda_c^+ \rightarrow \Lambda e^+ \nu_e$).

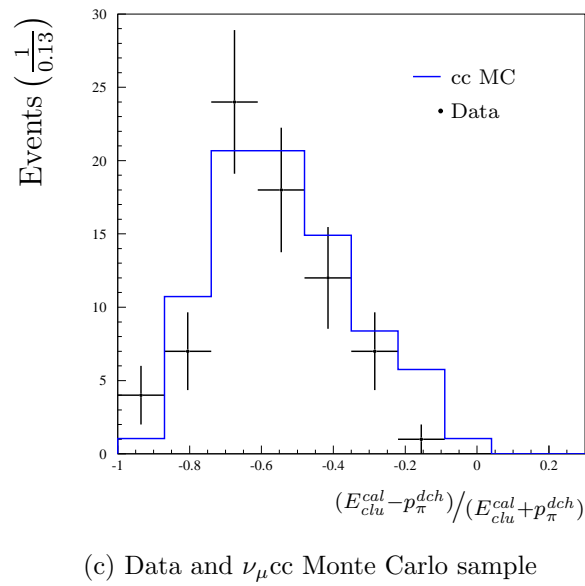
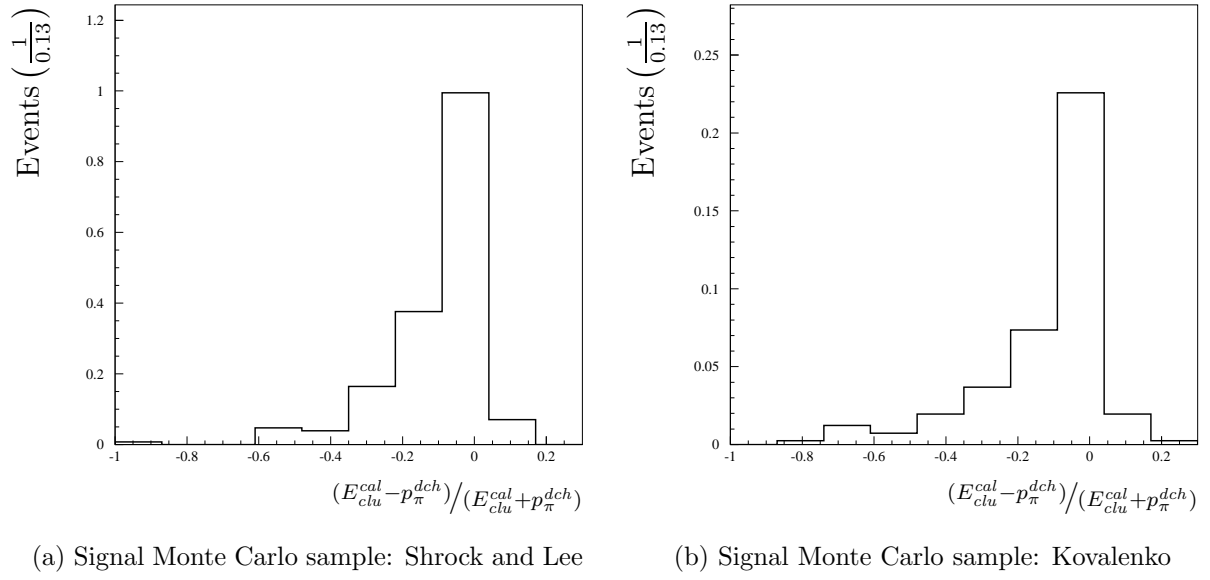


Figure 5.12: Normalized difference between ECAL energy and DCH momentum (searched decay channel: $\Lambda_c^+ \rightarrow \Lambda e^+ \nu_e$).

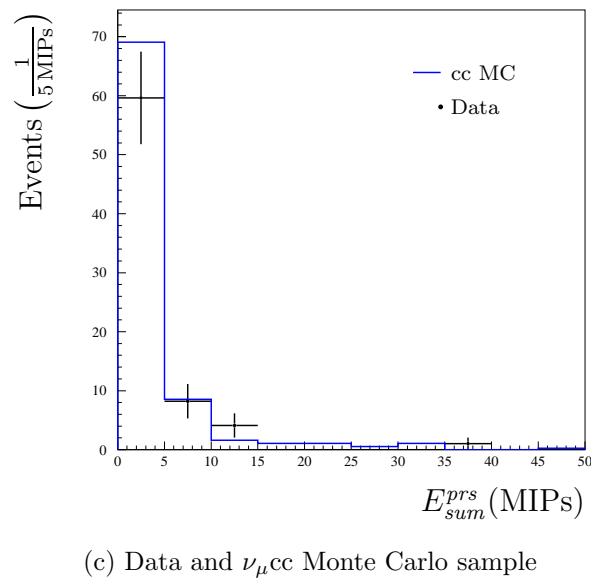
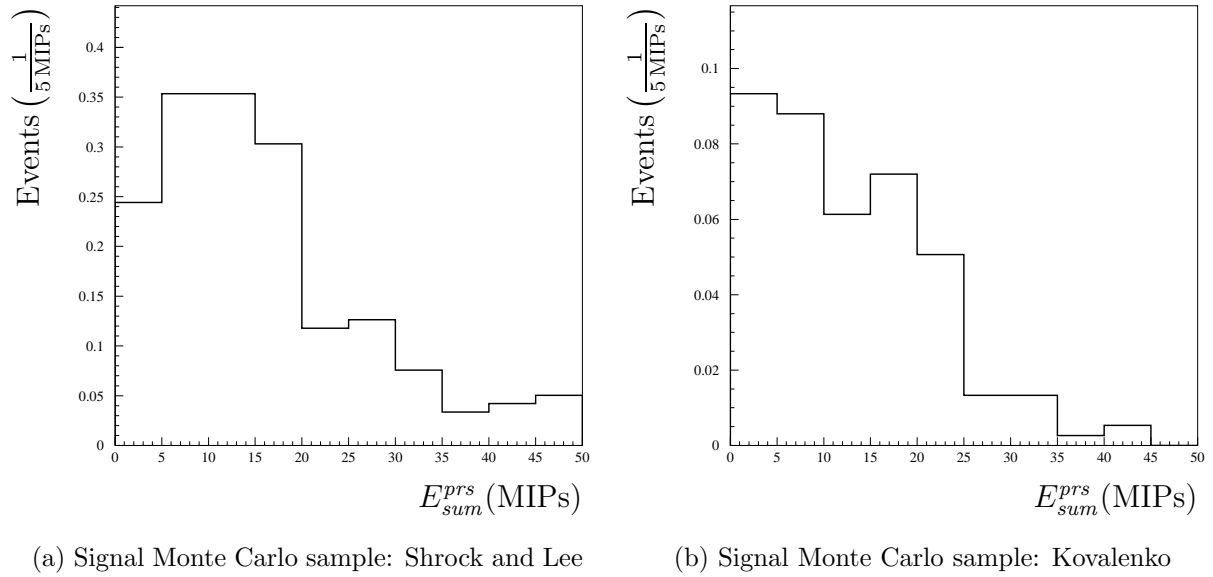


Figure 5.13: Energy deposited in the PRS in units of the energy loss of a *minimum ionizing particle* (searched decay channel: $\Lambda_c^+ \rightarrow \Lambda e^+ \nu_e$).

additional to the primary muon have been ruled out by the selection cuts defining the $\nu_\mu cc$ sample.

The expected number of events originating from QEC processes other than the one defined as signal have been estimated with the inclusive QEC Monte Carlo samples mentioned in Section 5.5. The expected numbers of events for both models and the corresponding efficiencies are given in Table 5.7. The signal selection in the semi-leptonic decay channel

	KOVALENKO		SHROCK	
	ϵ [%]	EVENTS	ϵ [%]	EVENTS
DCH Volume	100.0000	3709.5	100.0000	11039.6
Signal Sample	0.0101	0.4	0.0051	0.6

Table 5.7: Inclusive QEC: Contribution of Σ_c^+ , Σ_c^{++} and Λ_c^+ events not fulfilling the classifications of the signal sample.

of the Λ_c^+ yields a very clean sample with a background reduction of more than 6 orders of magnitude. However, only 1 – 2% of the signal events survive due to reconstruction inefficiencies and the small acceptance for low energy electrons. Together with the inherently small cross section and the branching ratio, less than two events are predicted by the model of Shrock and Lee. If the cross section is assumed to follow the model of Kovalenko less than one event is expected from QEC.

In Table 5.8 a comparison of the expected numbers of $\nu_\mu cc$ Monte Carlo events with the numbers of surviving data events is given. There are no data events left after the identification of the e^+ .

	MCCC BACKGROUND		DATA	
	ϵ [%]	EVENTS	ϵ [%]	EVENTS
$\nu_\mu cc$ SAMPLE	100.0000	622542.0	100.0000	622542
$E_{cal}^{neutral} < 1.0 \text{ GeV}$	48.7988	303793.2	49.1107	305735
$2 \text{ GeV}^2/c^4 < W_{vis}^2 < 8 \text{ GeV}^2/c^4$	18.9661	118071.7	19.0231	118427
$n_{V^0} = 1$	0.2124	1322.5	0.2199	1369
Λ SELECTION	0.1180	734.9	0.1205	750
$n_{V^1 cal}^{box} = 1$	0.0134	83.2	0.0117	73
$(E_{clu}^{cal} - p_\pi^{dch}) / (E_{clu}^{cal} + p_\pi^{dch}) > -0.125$	0.0004	2.4	0.0000	0
$E_{sum}^{prs} > 5.0 \text{ MIPs}$	0.0000	0.3	0.0000	0

Table 5.8: $\Lambda_c^+ \rightarrow \Lambda e^+ \nu_e$: Numbers of surviving events and efficiencies for the data and the background Monte Carlo simulation.

5.7 Semi-Inclusive Search: $B_c \rightarrow \Lambda + X$

One of the limiting factors for the search for QEC events in exclusive decays is the small size of the branching ratios. An inclusive search, on the other hand, does not allow an adequate background suppression since the only criterion to mark out the QEC events is given by $W^2 = m_{B_c}^2$ which, however, cannot be measured with sufficient accuracy. The semi-inclusive decay of a quasi elastically produced B_c into a Λ^7 ,

$$\begin{aligned} B_c &\rightarrow \Lambda + X \\ \Gamma_i/\Gamma_{\text{tot}} &= (35 \pm 11) \%, \end{aligned} \quad (5.32)$$

promises a higher number of expected signal events while still giving a means of background suppression by identifying the decaying Λ . The following characteristics are demanded in order to receive a sample enriched with QEC events:

- $2 \text{ GeV}^2/c^4 < W_{vis}^2 < 6 \text{ GeV}^2/c^4$: The square of the hadronic mass reconstructed from the visible neutrino and the muon energy, E_ν^{vis} and E_μ , should be in a range compatible with the B_c mass ($m_{\Lambda_c^+}^2 = 5.22 \text{ GeV}^2/c^4$, $m_{\Sigma_c}^2 = 6.01 \text{ GeV}^2/c^4$). For this decay channel, however, it has to be kept in mind that some of the energy may be carried away by undetected neutral particles.
- $n_{V^0} = 1$: There has to be a reconstructed V^0 vertex fulfilling the selection requirements described in Section 5.4, namely:

$$\mathcal{P}(\chi_{V^0}^2) > 0.01 \quad (5.33)$$

$$p_T^{l.o.f} < 0.1 \text{ GeV}/c \quad (5.34)$$

$$\tau < 6\tau_{V^0} \quad (5.35)$$

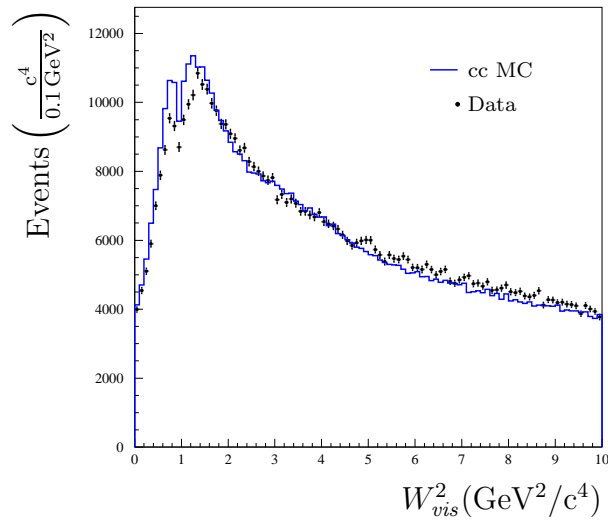
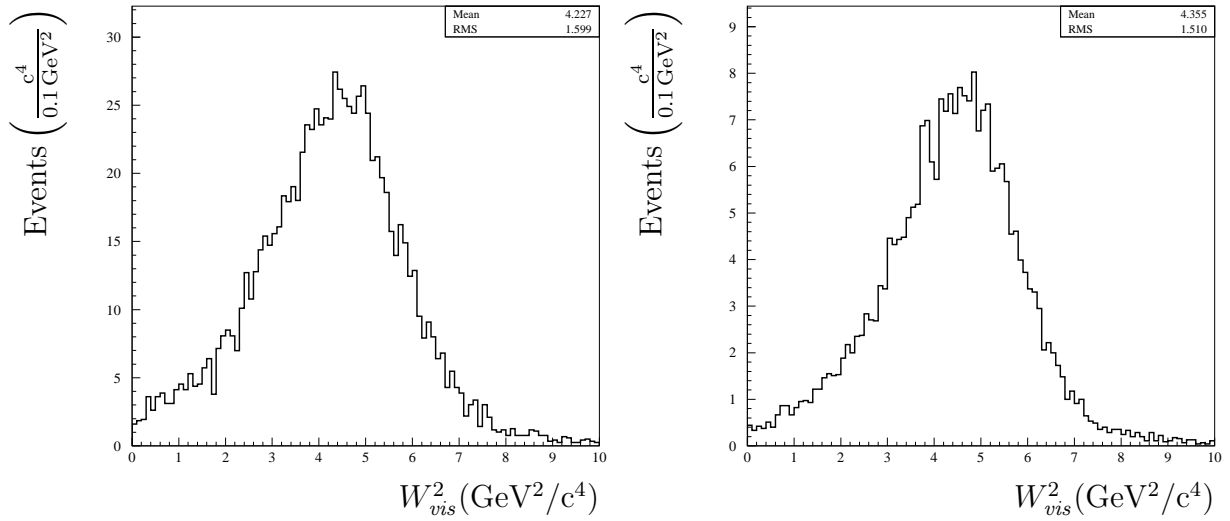
$$p_T^{2trks} > 0.06 \text{ GeV}/c. \quad (5.36)$$

- **Λ identification:** The reconstructed α^{2trks} and p_T^{2trks} of the particles emerging from the V^0 vertex are required to lie in a confined region:

$$\begin{aligned} 0.4 &\leq \alpha^{2trks} \leq 0.93 \\ 0.06 \text{ GeV}/c &\leq p_T^{2trks} \leq 0.12 \text{ GeV}/c. \end{aligned} \quad (5.37)$$

The expected numbers of signal and background events after each cut together with the corresponding efficiencies are given in Table 5.9. Since some of the momentum may be carried away by neutral particles, the mean of the reconstructed hadronic mass distribution of the QEC events is not at the value of the squared mass of one of the B_c , but shifted towards zero. In Figure 5.14 the distribution of the hadronic mass is plotted for both signal and the background Monte Carlo events. Bearing the displacement in mind, the

⁷Since the Σ_c^+ and the Σ_c^{++} always decay into a Λ_c^+ and a pion, all quasi elastically produced charmed baryons have essentially the same branching ratio for the decay into a Λ .

Figure 5.14: Invariant mass of the hadronic system (searched decay channel: $B_c \rightarrow \Lambda + X$).

	MCCC BACKGROUND		MC SIGNAL KOV.		MC SIGNAL SHR.	
	ϵ [%]	EVENTS	ϵ [%]	EVENTS	ϵ [%]	EVENTS
$\nu_{\mu\text{cc}}$ SAMPLE	100.0000	622519.0	100.0	476.7	100.0	1443.6
$2 \text{ GeV}^2/c^4 < W_{vis}^2 < 6 \text{ GeV}^2/c^4$	17.9056	111465.9	79.6	379.7	76.3	1101.9
$n_{V^0} = 1$	0.1533	954.1	15.8	75.3	16.5	237.8
Λ SELECTION	0.0863	537.3	15.3	72.9	16.1	231.8

Table 5.9: $B_c \rightarrow \Lambda + X$: Expected numbers of surviving events and efficiencies for the signal and the background Monte Carlo simulations.

upper boundary, that restricts the band of allowed W_{vis}^2 , has been put to a lower value than for the searches in the exclusive decay channels.

Also here, the Λ selection criterion rejects about 80% of the signal events because of reconstruction inefficiencies. The expected contribution due to quasi elastically produced B_c which do not decay into a Λ is given in Table 5.10. Efficiencies and numbers of events

	KOVALENKO		SHROCK	
	ϵ [%]	EVENTS	ϵ [%]	EVENTS
DCH Volume	100.0000	2900.3	100.0000	8643.3
Signal Sample	0.1747	5.1	0.1324	11.4

Table 5.10: Inclusive QEC: Contribution of Σ_c^+ , Σ_c^{++} and Λ_c^+ events not fulfilling the classifications of the signal sample.

have been estimated with the help of the inclusive Monte Carlo samples mentioned in Section 5.5.

In the final sample, a statistical significance of $S^{\text{shr}} = 8.7$ for the model of Shrock and Lee is achieved with S defined by

$$S = \frac{N_{\text{QEC}}}{\sqrt{N_{\text{QEC}} + N_{\text{background}}}}. \quad (5.38)$$

Here, the total QEC contribution is taken into consideration, i. e., N_{QEC} is equal to the sum of the numbers given in Table 5.9 and 5.10. The expected excess predicted by the model of Kovalenko would lead to an effect with a significance of $S^{\text{kov}} = 3.1$. Hence, if present, the contribution of a QEC process, having either cross section, should be observed. The investigation of the data sample, summarized in Table 5.11, shows no significant deviation from the predictions of the $\nu_{\mu\text{cc}}$ Monte Carlo simulation.

5.8 Calculation of Cross Section Limits

The small numbers of expected events in the exclusive decay channels (5.4) and (5.6) require Poisson statistics. For the treatment of a Poisson process with background and small sig-

	MCCC BACKGROUND		DATA	
	ϵ [%]	EVENTS	ϵ [%]	EVENTS
ν_μ CC SAMPLE	100.0000	622519.0	100.0000	622519
$2 \text{ GeV}^2/c^4 < W_{vis}^2 < 6 \text{ GeV}^2/c^4$	17.9056	111465.9	18.2616	113682
$n_{V^0} = 1$	0.1533	954.1	0.1594	992
Λ SELECTION	0.0863	537.3	0.0863	537

Table 5.11: $B_c \rightarrow \Lambda + X$: Numbers of surviving events and efficiencies for the data and the background Monte Carlo simulation.

nal, there are two methods accepted by the Particle Data Group [25], the Bayesian Method and the Unified Approach, a frequentist method proposed by Feldman and Cousins [57]. Systematic uncertainties can be incorporated into the latter, following a semi-Bayesian approach which has been suggested by Cousins and Highland [58]. In this work a program called POLE [59] is used for confidence interval calculations. Following the Unified Approach for the confidence interval construction, it allows for systematic uncertainties of both, signal and background processes, a feature which is inevitable, considering the large systematic errors introduced by the ignorance of the charmed baryon branching ratios. In principle, the significant number of observed data events for the semi-inclusive decay channel (5.7) would allow a Gaussian approximation, according to the well known central limit theorem. Independent systematic uncertainties could be included by using the common propagation of errors. However, since neither signal nor background are exactly known, the situation gets complicated and for the sake of consistency the upper confidence level is being calculated with the help of POLE as well.

As seen in sections 5.5, 5.6 and 5.7, it has been differentiated between two possible sources giving rise to the QEC events present in the final data sample in each searched channel. There is a contribution of $N_{\text{QEC}}^{\text{ex}}$ events originating from the exclusive decay of the according charmed baryon B_c as well as an inclusive contribution of $N_{\text{QEC}}^{\text{incl}}$ events from quasi elastically produced B_c which decay into different channels⁸. Hence, the number of selected QEC events in each searched channel is given by

$$N_{\text{QEC}}^{\text{sel}} = N_{\text{QEC}}^{\text{ex}} + N_{\text{QEC}}^{\text{incl}}. \quad (5.39)$$

The exclusive fraction is related to the total number of QEC reactions in the drift chambers, N_{QEC}^0 , by

$$N_{\text{QEC}}^{\text{ex}} = N_{\text{QEC}}^0 \cdot R \cdot \epsilon_{\text{ex}} \quad (5.40)$$

$$R = R_{\text{QEC}}^{B_c} \cdot R_{A_c^+}^i \quad (5.41)$$

where $R_{\text{QEC}}^{B_c}$ denotes the fraction of QEC reactions producing a B_c at the interaction vertex:

$$R_{\text{QEC}}^{B_c} = \frac{N_{B_c}}{N_{\text{QEC}}^0}, \quad (5.42)$$

⁸The definition of the samples $N_{\text{QEC}}^{\text{ex}}$ and $N_{\text{QEC}}^{\text{incl}}$ is such that they have no overlap.

and $R_{A_c^+}^i = \Gamma_i/\Gamma_{\text{tot}}$ refers to the branching ratio of the corresponding decay channel. Since only the production of the ground state baryons is implemented in the Monte Carlo generators, only QEC events including Λ_c^+ , Σ_c^+ or Σ_c^{++} are counted by N_{QEC}^0 .

The efficiency ϵ_{ex} results from the sequential application of the cuts defining the $\nu_{\mu}cc$ sample and the signal selection cuts:

$$\epsilon_{ex} = \epsilon_{\nu_{\mu}cc} \cdot \epsilon_{sel}. \quad (5.43)$$

A similar relation holds for the inclusive contribution:

$$N_{\text{QEC}}^{\text{incl}} = N_{\text{QEC}}^0(1 - R)\epsilon_{\text{incl}}. \quad (5.44)$$

Given an upper limit for the number of surviving QEC events in the final sample, the upper limit for the total number of QEC events, which may have occurred in the drift chambers, becomes:

$$\hat{N}_{\text{QEC}}^0 = \frac{\hat{N}_{\text{QEC}}^{\text{sel}}}{\epsilon_{\text{tot}}} \quad (5.45)$$

with the total efficiency given by:

$$\epsilon_{\text{tot}} = R(\epsilon_{ex} - \epsilon_{\text{incl}}) + \epsilon_{\text{incl}} \quad (5.46)$$

Finally, the upper limit for the QEC cross section relative to the known total charged current cross section can be obtained by a comparison with the predicted total number of charged current events.

5.9 Error Estimation

In order to determine confidence intervals of counting measurements the number of expected background events has to be known. The background must be established either by a different measurement or by a Monte Carlo simulation. In general, only an estimation with some uncertainty can be given. In this work the background has been estimated with the help of the Monte Carlo samples mentioned in Section 5.2.1. The uncertainties of the signal efficiencies include a statistical contribution as well as the Gaussian errors of the branching ratios given in [25]. To some degree, also the difference between the QEC models may be accounted for. The ignorance of the exact signal efficiencies is incorporated when calculating the confidence intervals of the signal fractions in the surviving data samples. The confidence levels for the QEC cross sections may then be determined with the mean values of the efficiencies.

This approach may not be intuitive since for the calculation of cross sections, Gaussian uncertainties of signal efficiencies are usually included with the help of the common error propagation when dividing by the signal efficiencies. However, there is no obvious way to combine a Poisson confidence interval for the number of signal events in the final sample with the Gaussian uncertainty of the signal efficiency. Therefore all the uncertainties have to be included already when calculating the confidence interval (see [58, 60]).

5.9.1 Background Uncertainties

For the background error different sources have been investigated:

- The background contributions from neutral current reactions and interactions of $\bar{\nu}_\mu$, ν_e and $\bar{\nu}_e$ have been estimated with the help of the corresponding Monte Carlo samples mentioned in Section 5.2.1.

After the application of the signal selection cuts for the search channels (5.4)-(5.7) no events have survived for any of these processes. With the help of Poisson statistics the following upper limits for the signal selection efficiencies have been determined at a 90 % confidence level:

	DCH events	Suppression factor	Events in the signal sample
nc	493000	$< 1.0 \times 10^{-6}$	< 0.5
$\bar{\nu}_e$ cc	20000	$< 2.6 \times 10^{-6}$	< 0.05
ν_e cc	3000	$< 6.5 \times 10^{-6}$	< 0.02
$\bar{\nu}_\mu$ cc	41000	$< 6.1 \times 10^{-6}$	< 0.25

In total, less than one event is expected and, thus, this contribution is neglected.

- The statistical errors are assumed to be Gaussian and can be determined from the number of surviving Monte Carlo background events:

$$\begin{aligned}
 - \Lambda_c^+ \rightarrow \Lambda \pi^+ \pi^+ \pi^-: \\
 \sigma_b = 2.5 \\
 \frac{\sigma_b}{b} = 10 \% \qquad (5.47)
 \end{aligned}$$

$$\begin{aligned}
 - \Lambda_c^+ \rightarrow \Lambda e^+ \nu_e: \\
 \sigma_b = 0.3 \\
 \frac{\sigma_b}{b} = 100 \% \qquad (5.48)
 \end{aligned}$$

$$\begin{aligned}
 - B_c \rightarrow \Lambda + X: \\
 \sigma_b = 11.9 \\
 \frac{\sigma_b}{b} = 2.2 \% \qquad (5.49)
 \end{aligned}$$

Obviously, the statistical error for the search in the semi-leptonic decay channel would have to be treated with Poisson statistics. However, since no data events are observed this approximation shall suffice.

- The systematic error introduced by the imperfections of the Monte Carlo simulation is difficult to quantify. The efficiency of the Λ selection may be slightly different for simulated events. Also the restriction of the W^2 range may not have exactly the same effect on data and on Monte Carlo events. For the two search channels where only few events have been observed in the final sample, this contribution is unimportant.

However, for the semi-inclusive channel this uncertainty may have quite an impact. Due to the lack of knowledge, all results will be given disregarding this systematic error. Nevertheless, a limit which includes a 5 % systematic background error will be presented to give an idea of the effect.

5.9.2 Uncertainties of the Signal Efficiency

The different sources contributing to the uncertainty of the total signal efficiencies can be identified from equation (5.46). Most prominent is the error of the measurement of the Λ_c^+ branching ratios. The uncertainties of the exclusive and inclusive efficiencies, ϵ_{ex} and ϵ_{incl} , are given statistically only. The fractions of the different QEC processes are determined for both models directly from the Monte Carlo simulation. This last contribution does not apply for the semi-inclusive search since Σ_c^+ and Σ_c^{++} decay into a Λ_c^+ and cannot be distinguished.

A summary of the values is given in tables 5.12, 5.13 and 5.14.

(%)	Kovalenko	Shrock	model ind.
ϵ_{ex}	6.005 ± 0.219	7.358 ± 0.244	6.682 ± 1.336
ϵ_{incl}	0.055 ± 0.007	0.048 ± 0.007	0.051 ± 0.008
$R_{\Lambda_c^+}^i$	2.110 ± 0.640	2.110 ± 0.640	2.110 ± 0.640
$R_{\text{QEC}}^{B_c}$	52.356 ± 0.424	62.621 ± 0.268	57.489 ± 11.498
ϵ_{tot}	0.120 ± 0.021	0.145 ± 0.030	0.132 ± 0.034
$\sigma_{\epsilon_{\text{tot}}}/\epsilon_{\text{tot}}$	17.787	20.917	26.007

Table 5.12: All the factors used to calculate the total signal efficiency in the decay channel $\Lambda_c^+ \rightarrow \Lambda \pi^+ \pi^+ \pi^-$. The errors are statistical only except for the last column where the difference between the models has been incorporated.

(%)	Kovalenko	Shrock	model ind.
ϵ_{ex}	0.799 ± 0.080	1.124 ± 0.096	0.962 ± 0.337
ϵ_{incl}	0.010 ± 0.003	0.005 ± 0.002	0.008 ± 0.005
$R_{\Lambda_c^+}^i$	1.342 ± 0.384	1.342 ± 0.384	1.342 ± 0.384
$R_{\text{QEC}}^{B_c}$	52.356 ± 0.424	62.621 ± 0.268	57.489 ± 11.498
ϵ_{tot}	0.016 ± 0.004	0.015 ± 0.004	0.015 ± 0.006
$\sigma_{\epsilon_{\text{tot}}}/\epsilon_{\text{tot}}$	22.875	24.885	40.866

Table 5.13: All the factors used to calculate the total signal efficiency in the decay channel $\Lambda_c^+ \rightarrow \Lambda e^+ \nu_e$. The errors are statistical only except for the last column where the difference between the models has been incorporated.

(%)	Kovalenko	Shrock	model ind.
ϵ_{ex}	8.733 ± 0.207	9.320 ± 0.216	9.026 ± 0.632
ϵ_{incl}	0.175 ± 0.015	0.132 ± 0.013	0.154 ± 0.046
$R_{\Lambda_c^+}^i$	22.370 ± 7.030	22.370 ± 7.030	22.370 ± 7.030
$R_{\text{QEC}}^{B_c}$	100.000 ± 0.000	100.000 ± 0.000	100.000 ± 0.000
ϵ_{tot}	2.089 ± 0.604	2.188 ± 0.648	2.138 ± 0.641
$\sigma_{\epsilon_{\text{tot}}}/\epsilon_{\text{tot}}$	28.888	29.610	29.956

Table 5.14: All the factors used to calculate the total signal efficiency in the decay channel $B_c \rightarrow \Lambda + X$. All errors are statistical only except for the last column where the difference between the models has been incorporated.

For the last columns the mean values are used and the difference between the models is assumed to correspond to the σ of a Gaussian distribution. This means for a parameter p :

$$p^{\text{ind}} = \frac{1}{2}(p^{\text{kov}} + p^{\text{shr}}) \quad (5.50)$$

$$\sigma_{p^{\text{ind}}} = |p^{\text{kov}} - p^{\text{shr}}|. \quad (5.51)$$

At least for the semi-inclusive search channel this crude approximation seems to be reasonable since the biggest difference between the models is given by the fraction of the production cross sections of the charmed baryons, $R_{\text{QEC}}^{B_c}$, which in this case drops out. The discrepancies between the efficiencies, on the other hand, is small enough to be treated as a Gaussian fluctuation.

The common error propagation is used to determine the uncertainty of the total efficiency ϵ_{tot} .

5.10 Results

The agreement between the measured numbers of events and the background predictions in tables 5.5, 5.8 and 5.11 allows the calculation of upper limits for the expected numbers of QEC events surviving the signal selections in each search channel. These upper limits, which incorporate the errors discussed in Section 5.9, are given in Table 5.15 at a 95% confidence level. The different Q^2 behavior of the differential cross sections demands a discrimination of the QEC models. However, following the approach described in Section 5.9, also a limit which is to some degree model independent can be given. Dividing by the signal efficiencies ϵ_{tot} defined in Section 5.8 and summarized in Table 5.16, upper limits for the number of expected QEC events which may have occurred in the drift chambers can be determined. The number of scattering events is proportional to the cross section

Search channel	95 % upper limit for signal sample events		
	Kovalenko	Shrock, Lee	model ind.
$\Lambda_c^+ \rightarrow \Lambda \pi^+ \pi^+ \pi^-$	< 15.00	< 15.30	< 16.35
$\Lambda_c^+ \rightarrow \Lambda e^+ \nu_e$	< 2.97	< 3.06	< 3.75
$B_c \rightarrow \Lambda + X$	< 58.50	< 58.80	< 59.15

Table 5.15: Upper limits (95 % C. L.) for the expected numbers of QEC events surviving the signal selection cuts. The limits are given for the specific QEC models as well as for a model independent average.

Search channel	Signal Efficiencies ϵ_{tot} (%)		
	Kovalenko	Shrock, Lee	model ind.
$\Lambda_c^+ \rightarrow \Lambda \pi^+ \pi^+ \pi^-$	0.120	0.145	0.132
$\Lambda_c^+ \rightarrow \Lambda e^+ \nu_e$	0.016	0.015	0.015
$B_c \rightarrow \Lambda + X$	2.089	2.188	2.138

Table 5.16: Total signal efficiencies for each search channel. The definition of ϵ_{tot} may be found in Section 5.8.

averaged over the neutrino energy spectrum:

$$\langle \sigma \rangle = \frac{\int \sigma(E_\nu) \phi_\nu(E_\nu) dE_\nu}{\int \phi_\nu(E_\nu) dE_\nu} \quad (5.52)$$

with the neutrino flux

$$\phi_\nu = \frac{dN_\nu}{dE_\nu}. \quad (5.53)$$

Since the absolute flux of the muon neutrinos is not very well known, cross sections are generally given relative to the total charged current cross section. The upper limits for the relative average cross section are presented in Table 5.17. In principle, a combined limit

Search channel	95 % upper limit for $\langle \sigma_{\text{QEC}} \rangle / \langle \sigma_{cc} \rangle$ (%)		
	Kovalenko	Shrock, Lee	model ind.
$\Lambda_c^+ \rightarrow \Lambda \pi^+ \pi^+ \pi^-$	< 0.97	< 0.82	< 0.97
$\Lambda_c^+ \rightarrow \Lambda e^+ \nu_e$	< 1.48	< 1.64	< 1.95
$B_c \rightarrow \Lambda + X$	< 0.22	< 0.21	< 0.22

Table 5.17: Upper limits (95 % C. L.) for QEC cross sections relative to the total charged current cross section. The cross sections are averaged over the ν_μ energy spectrum of the CERN SPS neutrino beam which has a mean energy of $\langle E_\nu \rangle = 24.3$ GeV.

could be computed including the results of all search channels. However, since the limit

would not improve much because of the dominating influence of the semi-inclusive decay channel $B_c \rightarrow \Lambda + X$, this has been abandoned.

As described in Section 4.2, the implemented QEC Monte Carlo generator does not include the processes

$$\nu_\mu + n \rightarrow \mu^- + \Sigma_c^{*+} \quad (2520) \quad (5.54)$$

$$\nu_\mu + p \rightarrow \mu^- + \Sigma_c^{*++} \quad (2530). \quad (5.55)$$

The inclusion of the additional processes would lead to a different $R_{\text{QEC}}^{B_c}$ and hence to a different total efficiency ϵ_{tot} (see (5.46)) for the search channels $\Lambda_c^+ \rightarrow \Lambda e^+ \nu_e$ and $\Lambda_c^+ \rightarrow \Lambda \pi^+ \pi^+ \pi^-$. This means that the upper limits determined from these two channels only hold for the sum of the quasi elastic Λ_c^+ , Σ_c^+ and Σ_c^{*+} production. The results of the semi-inclusive search in the channel $B_c \rightarrow \Lambda + X$, on the other hand, should be valid for the sum of all QEC processes, since the Σ_c^* cannot be distinguished from Λ_c^+ and Σ_c (i. e., $R_{\text{QEC}}^{B_c} \equiv 1$), and the efficiencies ϵ_{ex} and ϵ_{incl} should be roughly the same for Λ_c^+ , Σ_c and Σ_c^* . Hence, the same total efficiency ϵ_{tot} should be obtained.

If the total charged current cross section is assumed to grow linearly with the neutrino energy (see Figure 2.6), the cross section average becomes:

$$\langle \sigma_{\text{cc}} \rangle = \sigma_0 \cdot \frac{\int E_\nu \phi_\nu(E_\nu)}{\int \phi_\nu(E_\nu) dE} = \sigma_0 \cdot \langle E_\nu \rangle = \sigma_{\text{cc}}(\langle E_\nu \rangle). \quad (5.56)$$

Hence, a limit (95 % C. L.) on the cross section averaged over the neutrino energy spectrum can be quoted:

$$\langle \sigma_{\text{QEC}} \rangle < 3.58 \times 10^{-40} \text{ cm}^2. \quad (5.57)$$

Several measurements of quasi elastic charm production processes have been performed in the last 25 years, most of them in bubble chamber experiments [14, 15, 16, 17]. Also, two emulsion experiments have searched for QEC events: E531 [18] at Fermilab and CHORUS [19] at CERN. For a comparison all the cross section measurements are listed below:⁹

- Gargamelle [14]:

$$\langle \sigma_{\Lambda_c^+}^n \rangle + \langle \sigma_{\Sigma_c^+}^n \rangle + \langle \sigma_{\Sigma_c^{*+}}^n \rangle = (31.8 \pm 19.2) \times 10^{-40} \text{ cm}^2 \quad (5.58)$$

- Son et al. [15]:

$$\langle \sigma_{\Lambda_c^+}^n \rangle = (80_{-65}^{+84}) \times 10^{-40} \text{ cm}^2 \quad (5.59)$$

- BEBC [16]:

$$\langle \sigma_{\Sigma_c^{*++}}^p \rangle = (2.3_{-1.6}^{+2.7}) \times 10^{-40} \text{ cm}^2 \quad (5.60)$$

⁹The cross sections are given for neutron, proton or isoscalar targets depending on the measured process. It is crucial to normalize properly if cross sections for different targets are compared: $\sigma^N = \frac{1}{2}(\sigma^n + \sigma^p)$. Thus, if a process only occurs for either a proton or a neutron, e. g. $\nu n \rightarrow \mu \Lambda_c^+$, a factor two must be incorporated: $\sigma(\nu n \rightarrow \mu \Lambda_c^+) = 2\sigma(\nu N \rightarrow \mu \Lambda_c^+)$.

- E531 [18]:

$$\langle \sigma_{\Lambda_c^+}^n \rangle = (3.7_{-2.3}^{+3.7}) \times 10^{-40} \text{ cm}^2 \quad (5.61)$$

- SKAT [17]:

$$\langle \sigma_{\Sigma_c^{++}}^p \rangle = (2.3 \pm 2.0) \times 10^{-40} \text{ cm}^2 \quad (5.62)$$

$$\langle \sigma_{\Sigma_c^{*++}}^p \rangle = (4.5 \pm 4.0) \times 10^{-40} \text{ cm}^2 \quad (5.63)$$

- CHORUS [19]:

$$\langle \sigma_{\Lambda_c^+}^n \rangle + \langle \sigma_{\Sigma_c^+}^n \rangle + \langle \sigma_{\Sigma_c^{*+}}^n \rangle = (5.5_{-2.3}^{+3.9}) \times 10^{-40} \text{ cm}^2 \quad (5.64)$$

$$\langle \sigma_{\Sigma_c^{++}}^p \rangle + \langle \sigma_{\Sigma_c^{*++}}^p \rangle = (2.3_{-1.6}^{+2.6}) \times 10^{-40} \text{ cm}^2 \quad (5.65)$$

$$\langle \sigma_{\text{QEC}}^N \rangle = (3.8_{-1.5}^{+2.3}) \times 10^{-40} \text{ cm}^2. \quad (5.66)$$

The comparison of the different measurements can only be approximate as long as the energy dependence of the QEC cross section is not known. However, considering the flatness of the QEC cross section which is observed for all suggested models, the introduced uncertainty is rather small compared to the statistical uncertainties of the measurements. An estimation of the model dependence will be given at the end of the section. The CERN experiments CHORUS and NOMAD were both situated in the same neutrino beam. Hence, for these two the ambiguity of the energy spectra may be neglected completely. Figure 5.15 shows the results of all stated measurements normalized to an isoscalar nucleon target. The different contributions measured by an experiment have been summed up in order to compare them with the upper limit measured by NOMAD. Due to the large uncertainties, all measurements are compatible within 1.5σ .

As mentioned in Section 5.9.1, the systematic uncertainties of the background have been omitted due to the lack of knowledge. For the semi-inclusive search channel, the background uncertainty has quite an impact. If an additional systematic error of 5% is assumed, the 95% upper limit for the cross section average rises up to:

$$\langle \sigma_{\text{QEC}} \rangle < 5.0 \times 10^{-40} \text{ cm}^2. \quad (5.67)$$

Normalizing the predictions of the theoretical models to the determined upper limits, allows to constrain the cross sections of quasi elastic Λ_c^+ , Σ_c^+ and Σ_c^{++} production separately. For an isoscalar target this yields the following model dependent numbers, again at a 95% confidence level:

$\langle \sigma \rangle / \langle \sigma_{cc} \rangle$	Kovalenko	Shrock, Lee
$\nu_\mu N \rightarrow \mu^- \Lambda_c^+$	$< 0.114\%$	$< 0.131\%$
$\nu_\mu N \rightarrow \mu^- \Sigma_c^+$	$< 0.034\%$	$< 0.026\%$
$\nu_\mu N \rightarrow \mu^- \Sigma_c^{++}$	$< 0.070\%$	$< 0.052\%$

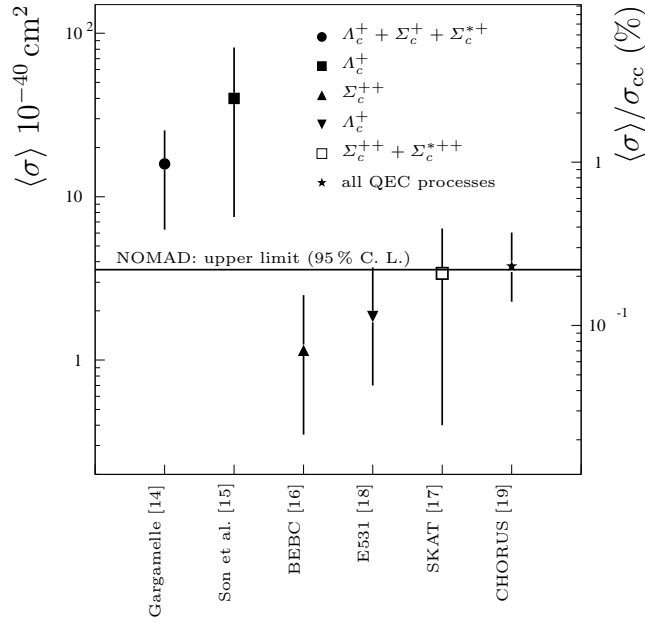


Figure 5.15: Compilation of QEC measurements. All cross sections are given for isoscalar targets.

Also, limits for the absolute QEC cross section on an isoscalar target, $\sigma_{\text{QEC}} = \frac{1}{2}(\sigma_{\Lambda_c^+} + \sigma_{\Sigma_c^+} + \sigma_{\Sigma_c^{++}})$, can be given. For a comparison with the values compiled in Table 2.3 of Section 2.3.3, a neutrino energy of 10 GeV has been chosen:

$$\sigma_{\text{QEC}}^{\text{kov}} < 3.75 \times 10^{-40} \text{ cm}^2 \quad (5.68)$$

$$\sigma_{\text{QEC}}^{\text{shr}} < 3.34 \times 10^{-40} \text{ cm}^2. \quad (5.69)$$

The difference is a result of the different energy dependence of the cross section predictions which are shown in Figure 5.16. The plot also allows to estimate the discrepancy introduced by averaging the cross section over the neutrino energy spectrum. The upper limit for the cross section becomes $4 \times 10^{-40} \text{ cm}^2$ rather than the $3.6 \times 10^{-40} \text{ cm}^2$ estimated by assuming an energy independent cross section.

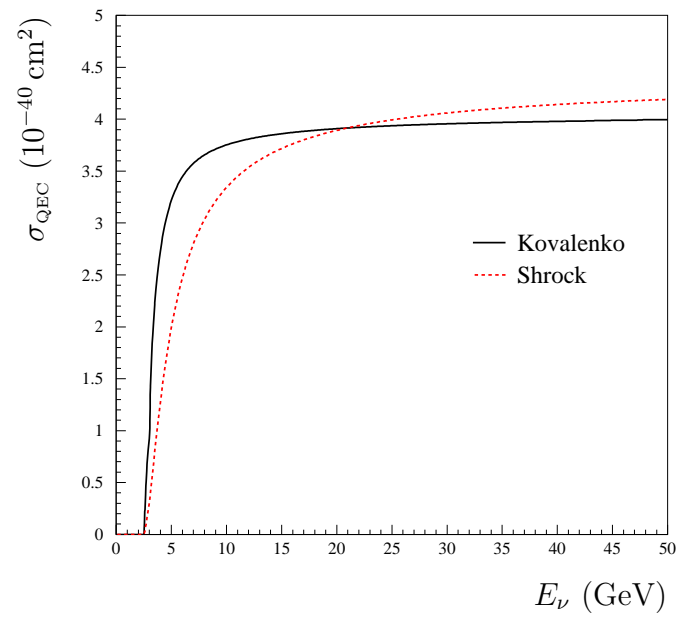


Figure 5.16: Energy dependence of the upper limits for the two investigated QEC models.

Chapter 6

Conclusion

A search for the quasi elastic charm production processes

$$\nu_\mu + n \rightarrow \mu^- + \Lambda_c^+(2285) \quad (6.1)$$

$$\nu_\mu + n \rightarrow \mu^- + \Sigma_c^+(2455) \quad (6.2)$$

$$\nu_\mu + n \rightarrow \mu^- + \Sigma_c^{*+}(2520) \quad (6.3)$$

and

$$\nu_\mu + p \rightarrow \mu^- + \Sigma_c^{++}(2455) \quad (6.4)$$

$$\nu_\mu + p \rightarrow \mu^- + \Sigma_c^{*++}(2530). \quad (6.5)$$

has been performed for three different decays of charmed baryons, namely

$$\Lambda_c^+ \rightarrow \Lambda \pi^+ \pi^+ \pi^- \quad (6.6)$$

$$\Lambda_c^+ \rightarrow \Lambda e^+ \nu_e \quad (6.7)$$

$$\Lambda_c^+, \Sigma_c, \Sigma_c^* \rightarrow \Lambda \text{ anything}. \quad (6.8)$$

Exploiting the good momentum measurement and tracking capabilities of NOMAD, the Λ were found by searching for their decay vertices and distinguished from $\bar{\Lambda}$, K_S^0 and γ by using their specific decay asymmetry which can be manifested in an Podolanski-Armenteros plot. Kinematic cuts have been applied, taking into account the characteristics of quasi elastic charm events, such as a fixed W^2 . In the decay channel (6.6) a cut on the reconstructed invariant mass of the Λ_c^+ has been applied. The electron in the semi-leptonic decay channel (6.7) was identified with the help of its energy deposit in the preshower detector and the electromagnetic calorimeter. Good sensitivity was found for the semi-inclusive decay channel (6.8), due to the relatively high branching ratio.

For all search channels, the data has been found to be in agreement with the background predicted from charged and neutral current Monte Carlo simulations.

An upper limit for the cross section averaged over the neutrino energy spectrum of the CERN SPS neutrino beam ($\langle E_\nu \rangle = 24.3 \text{ GeV}$) has been derived. At 95 % confidence level

this limit has been found to be

$$\langle \sigma_{\text{QEC}} \rangle < 3.58 \times 10^{-40} \text{ cm}^2 \quad (6.9)$$

$$\frac{\langle \sigma_{\text{QEC}} \rangle}{\langle \sigma_{\text{cc}} \rangle} < 0.22 \% \quad (6.10)$$

The limit calculation includes the systematic errors of the signal efficiencies, however, systematic uncertainties of the background estimation have been neglected due to the lack of knowledge.

Given the almost energy independent behavior of the quasi elastic charm production cross section for energies above 15 GeV, the absolute limit for the cross section has been derived to be

$$\sigma_{\text{QEC}} < 4.0 \times 10^{-40} \text{ cm}^2 \quad (6.11)$$

at a 95 % confidence level.

Appendix A

Variables for Event Classification

$n_{trksV^1}^{box}$ The number of tracks having their first hit sufficiently close to the primary vertex and which are not identified as coming from a decay, scattering or V^0 vertex. This means the first hit must be in a cylinder ($radius = 30$ cm, $length = 40$ cm) with axis along the neutrino beam direction and starting 10 cm in front of the primary vertex.

$n_{trksV^1}^{box+}$ The same as $n_{trksV^1}^{box}$ but positively charged.

$n_{trksV^1}^{box-}$ The same as $n_{trksV^1}^{box}$ but negatively charged.

$n_{V^1 cal}^{box}$ The number of primary tracks, defined like $n_{trksV^1}^{box}$, which reach the PRS and the ECAL.

$\sum_{box} Q_{trks}$ The charge sum of the tracks which have their first hit sufficiently close to the primary vertex (see also $n_{trksV^1}^{box}$).

V^0 A vertex with two outgoing tracks of opposite charge but no incoming track.

n_{V^0} The number of V^0 vertices.

E_ν^{vis} The visible neutrino energy is equal to the length of the total momentum measured in an event.

E_μ The reconstructed energy of the primary muon.

Q_{vis}^2 The reconstructed Q^2 .

W_{vis}^2 The reconstructed W^2 .

x_{vis} The reconstructed Bjorken scaling variable x_{Bj} .

y_{vis} The reconstructed inelasticity $y = \frac{E_\nu - E_\mu}{E_\nu}$.

$M_{rec}^{A_c^+}$ The reconstructed mass of the A_c^+ .

$\mathcal{P}(\chi_{V^0}^2)$ χ^2 probability of the V^0 vertex fit during reconstruction.

$p_T^{l.o.f}$ Transverse component of the total momentum of the two outgoing charged tracks of a V^0 vertex with respect to the line connecting the primary and the V^0 vertex (see figure 5.1).

p_T^{2trks} The transverse momentum of the particle coming from a V^0 decay with respect to the momentum of the mother particle.

p_L^+ The longitudinal momentum of the positively charged particle coming from a V^0 decay with respect to the momentum of the mother particle.

p_L^- The longitudinal momentum of the negatively charged particle coming from a V^0 decay with respect to the momentum of the mother particle.

α^{2trks} The decay asymmetry $\alpha^{2trks} = \frac{p_L^+ - p_L^-}{p_L^+ + p_L^-}$.

M_{rec}^Λ The reconstructed mass of the Λ .

E_{clu}^{cal} The energy of a cluster in the calorimeter (CAL).

E_{sum}^{prs} Sum of the energy of the horizontal and vertical preshower tubes.

p_π^{dch} The momentum of a track determined from a fit with a pion hypotheses in the drift chambers.

$E_{cal}^{neutral}$ The energy of all neutral “tracks”, i. e. calorimeter objects which have been associated to a reconstructed vertex.

Bibliography

- [1] Y. Fukuda et al., Evidence for oscillation of atmospheric neutrinos, *Phys. Rev. Lett.* **81**, 1562–1567 (1998).
- [2] Q. R. Ahmad et al., Direct evidence for neutrino flavor transformation from neutral-current interactions in the Sudbury Neutrino Observatory, *Phys. Rev. Lett.* **89**, 011301 (2002).
- [3] K. Eguchi et al., First results from KamLAND: Evidence for reactor anti- neutrino disappearance, *Phys. Rev. Lett.* **90**, 021802 (2003).
- [4] N. Armenise et al., Study of Neutrino induced Dimuon Events in GARGAMELLE at CERN SPS, *Phys. Lett.* **B86**, 115 (1979).
- [5] J. Finjord and F. Ravndal, Neutrino - Production of Charmed Baryons, *Phys. Lett.* **B58**, 61 (1975).
- [6] R. E. Shrock and B. W. Lee, Estimates of Charm Production in Exclusive Neutrino Reactions, *Phys. Rev.* **D13**, 2539 (1976).
- [7] R. E. Shrock and B. W. Lee, Errata, *Phys. Rev.* **D14**, 313 (1976).
- [8] C. Avilez, T. Kobayashi, and J. G. Korner, Weak Production of Charmed Baryon Resonances, *Phys. Lett.* **B66**, 149 (1977).
- [9] C. Avilez, T. Kobayashi, and J. G. Korner, Quark Model Calculation of Charmed Baryon Production by Neutrinos, *Phys. Rev.* **D17**, 709 (1978).
- [10] C. Avilez and T. Kobayashi, Comment on the Neutrino Production of the Ground State Charmed Baryons, *Phys. Rev.* **D19**, 3448 (1979).
- [11] A. Amer, M. B. Gavela, A. Le Yaouanc, and L. Oliver, Problem of Charmed Baryons Production Rate by Neutrino, *Phys. Lett.* **B81**, 48 (1979).
- [12] S. G. Kovalenko, Quasielastic neutrino production of charmed baryons from the point of view of local duality, *Sov. J. Nucl. Phys.* **52**, 934–936 (1990).

- [13] P. Migliozi, G. D'Ambrosio, G. Miele, and P. Santorelli, A direct evaluation of the $\Lambda/c+$ absolute branching ratios: A new approach, *Phys. Lett.* **B462**, 217–224 (1999).
- [14] N. Armenise et al., Evidence for charmed baryon 'elastic' production in neutrino reactions at CERN SPS, *Phys. Lett.* **B104**, 409 (1981).
- [15] D. Son et al., Quasielastic charmed baryon production and exclusive strange particle production by high-energy neutrinos, *Phys. Rev.* **D28**, 2129 (1983).
- [16] G. T. Jones et al., Production of charmed hadrons in neutrino proton and anti-neutrino proton charged current interactions, *Z. Phys.* **C36**, 593 (1987).
- [17] V. V. Ammosov et al., Observation of the production of charmed $\Sigma(c)^{*++}$ baryons in neutrino interactions at the SKAT bubble chamber, *JETP Lett.* **58**, 247–251 (1993).
- [18] N. Ushida et al., Cross-sections for neutrino production of charmed particles, *Phys. Lett.* **B206**, 375 (1988).
- [19] A. Kayis-Topaksu et al., Cross-section measurement for quasi-elastic production of charmed baryons in νN interactions, *Phys. Lett.* **B575**, 198–207 (2003).
- [20] F. Halzen and A. D. Martin, *Quarks and Leptons: An Introductory Course in Modern Particle Physics*, John Wiley and sons, 1984.
- [21] M. E. Peskin and D. V. Schroeder, *An Introduction to Quantum Field Theory*, Advanced-Wesley Publishing Company, 1995.
- [22] F. Mandl and G. Shaw, *Quantum Field Theory*, John Wiley and sons, 1993.
- [23] N. Schmitz, *Neutrinophysik*, Teubner, 1997.
- [24] V. M. Abazov et al., A precision measurement of the mass of the top quark, *Nature* **429**, 638–642 (2004).
- [25] S. Eidelman et al., Review of Particle Physics, *Physics Letters B* **592**, 1+ (2004).
- [26] D. H. Perkins, *Introduction to High Energy Physics*, Cambridge University Press, 4th edition, 1999.
- [27] P. Langacker, editor, *Precision Tests of the Standard Electroweak Model*, volume 14 of *Advanced Series on Directions in High Energy Physics*, World Scientific, 1995.
- [28] L.-L. Chau and W.-Y. Keung, Comments on the Parametrization of the Kobayashi-Maskawa Matrix, *Phys. Rev. Lett.* **53**, 1802 (1984).

- [29] K. Hagiwara et al., Review of Particle Physics, *Physical Review D* **66**, 010001+ (2002).
- [30] C. H. Llewellyn Smith, Neutrino Reactions at Accelerator Energies, *Phys. Rep.* **3**, 261 (1972).
- [31] A. Pais, Weak Interactions at High Energies, *Annals of Physics* **63**, 361 (1971).
- [32] R. E. Marshak, Riazuddin, and C. P. Ryan, *Theory of Weak Interactions in Particle Physics*, Wiley-Interscience, 1969.
- [33] E. D. Bloom and F. J. Gilman, Scaling and the behavior of Nucleon Resonances in Inelastic Electron - Nucleon Scattering, *Phys. Rev.* **D4**, 2901 (1971).
- [34] P. Astier et al., Search for the oscillation muon-neutrino \rightarrow tau- neutrino, CERN Geneva - CERN-SPSLC-91-21 (91/03,rec.Apr.) 24 p. CERN Geneva - CERN-SPSLC-P-261 (91/03,rec.Apr.) 24 p.
- [35] P. Astier et al., Final NOMAD results on $\nu/\mu \rightarrow \nu/\tau$ and $\nu/e \rightarrow \nu/\tau$ oscillations including a new search for ν/τ appearance using hadronic tau decays, *Nucl. Phys.* **B611**, 3–39 (2001).
- [36] P. Astier et al., Search for $\nu/\mu \rightarrow \nu/e$ oscillations in the NOMAD experiment, *Phys. Lett.* **B570**, 19–31 (2003).
- [37] P. Astier et al., Prediction of neutrino fluxes in the NOMAD experiment, *Nucl. Instrum. Meth.* **A515**, 800–828 (2003).
- [38] L. Casagrande et al., The alignment of the CERN West Area neutrino facility, CERN-96-06.
- [39] J. Altegoer et al., The NOMAD experiment at the CERN SPS, *Nucl. Instrum. Meth.* **A404**, 96–128 (1998).
- [40] M. Barranco-Luque et al., The Construction of the Central Detector for an Experiment at the CERN anti-p p Collider, *Nucl. Instr. Meth.* **176**, 175 (1980).
- [41] J. Altegoer et al., The trigger system of the NOMAD experiment, *Nucl. Instrum. Meth.* **A428**, 299–316 (1999).
- [42] L. J. Winton, *Coherent Diffractive Pion Production in Charged Current Neutrino Interactions*, PhD thesis, University of Melbourne, 1999.
- [43] M. Anfreville et al., The drift chambers of the Nomad experiment, *Nucl. Instrum. Meth.* **A481**, 339–364 (2002).
- [44] W. W. M. Allison and J. H. Cobb, Relativistic Charged Particle Identification by Energy Loss, *Ann. Rev. Nucl. Part. Sci.* **30**, 253 (1980).

- [45] M. L. Cherry et al., Transition radiation from relativistic electrons in periodic radiators, *Phys. Rev.* **D10**, 3594–3607 (1974).
- [46] G. Bassompierre et al., A large area transition radiation detector for the NOMAD experiment, *Nucl. Instrum. Meth.* **A403**, 363–382 (1998).
- [47] A. Fasso, A. Ferrari, P. R. Sala, and J. Ranft, FLUKA: Status and prospects for hadronic applications, Prepared for International Conference on Advanced Monte Carlo for Radiation Physics, Particle Transport Simulation and Applications (MC 2000), Lisbon, Portugal, 23-26 Oct 2000.
- [48] R. Brun and F. Carminati, GEANT detector description and simulation Tool, (1993), CERN program library long writeup W5013.
- [49] G. Ingelman, A. Edin, and J. Rathsman, LEPTO 6.5 - A Monte Carlo Generator for Deep Inelastic Lepton-Nucleon Scattering, *Comput. Phys. Commun.* **101**, 108–134 (1997).
- [50] D. Rein and L. M. Sehgal, Neutrino Excitation of Baryon Resonances and Single Pion Production, *Ann. Phys.* **133**, 79 (1981).
- [51] M. Gluck, E. Reya, and A. Vogt, Parton distributions for high-energy collisions, *Z. Phys.* **C53**, 127–134 (1992).
- [52] A. Bodek and J. L. Ritchie, Fermi Motion Effects in Deep Inelastic Lepton Scattering from Nuclear Targets, *Phys. Rev.* **D23**, 1070 (1981).
- [53] T. Sjostrand, High-energy physics event generation with PYTHIA 5.7 and JETSET 7.4, *Comput. Phys. Commun.* **82**, 74–90 (1994).
- [54] L. M. Chounet, J. M. Gaillard, and M. K. Gillard, Leptonic decays of hadrons, *Phys. Rept.* **4**, 199–324 (1972).
- [55] V. D. Barger and R. J. N. Phillips, *Collider Physics*, Addison-Wesley Publishing Company, Inc., 1996.
- [56] I. G. Bird, Vertex Finding and Fitting Package, NOMAD Memo 96-019, August 1996.
- [57] G. J. Feldman and R. D. Cousins, A Unified approach to the classical statistical analysis of small signals, *Phys. Rev.* **D57**, 3873–3889 (1998).
- [58] R. D. Cousins and V. L. Highland, Incorporating systematic uncertainties into an upper limit, *Nucl. Instrum. Meth.* **A320**, 331–335 (1992).
- [59] J. Conrad, O. Botner, A. Hallgren, and C. Perez de los Heros, Including systematic uncertainties in confidence interval construction for Poisson statistics, *Phys. Rev.* **D67**, 012002 (2003).

- [60] C. Giunti, Treatment of the background error in the statistical analysis of Poisson processes, Phys. Rev. **D59**, 113009 (1999).

Curriculum Vitae

Personal Data

Full Name Markus Bischofberger
Date of Birth June 23, 1975
Place of Birth Zurich (Switzerland)
Nationality Swiss, citizen of Teufen (AR), Niederweningen (ZH)

Education

1982 – 1988 Primary School Niederweningen (ZH)
1988 – 1994 Gymnasium Bülach (ZH), Maturitätstypus C
1995 – 2000 Studies in physics at the Swiss Federal Institute of Technology (ETH)
 in Zurich
2000 Diploma thesis (4 months) at the ETH Zurich. Title of the thesis:
 “Calculation of cosmic ray induced nucleon and neutrino fluxes
 on the surface of the earth”
2001 – 2005 Graduate education in experimental particle physics at the ETH Zurich